A detailed study of the unidentified TeV source HESS J1826-130 in the search for Galactic PeVatrons with H.E.S.S.

Eine detaillierte Analyse der unidentifizierten
TeV-Quelle HESS J1826-130
auf der Suche nach Galaktischen PeVatrons
mit dem H.E.S.S. Instrument

Der Naturwissenschaftlichen Fakultät
der Friedrich-Alexander-Universität Erlangen-Nürnberg
zur Erlangung des Doktorgrades Dr. rer. nat.

vorgelegt von
Alexander Elmar Ziegler
aus Bamberg

Als Dissertation genehmigt von der Naturwissenschaftlichen Fakultät
der Friedrich-Alexander-Universität Erlangen-Nürnberg

Tag der mündlichen Prüfung:	10.07.2018
Vorsitzender des Promotionsorgans:	Prof. Dr. Georg Kreimer
Gutachter:	Prof. Dr. Christopher van Eldik Dr. Johannes Knapp

Abstract

This thesis presents a detailed study of the unidentified TeV γ-ray source HESS J1826-130. The source was detected within the H.E.S.S. Galactic plane survey, in which it was reconstructed with a very hard energy spectrum without clear indication for a spectral cutoff in the considered energy range. Assuming a hadronic scenario in which the observable γ-ray emission would be produced by interactions of highly energetic hadronic particles with ambient molecular matter, these source characteristics point to the presence of a highly energetic particle accelerator, potentially accelerating cosmic-ray particles up to PeV (10^{15} eV) energies. The search for such Galactic PeVatrons currently constitutes one of the major questions in the research field of high-energy astrophysics. A dedicated re-observation campaign of HESS J1826-130 with the H.E.S.S. instrument during summer 2015 has yielded an extended data set, which was used in this work for a detailed spectral and morphological analysis of the emission region to allow for further evaluation of the potential PeVatron character of the source.

The emission region of HESS J1826-130 is located close to the strongly extended and bright pulsar wind nebula HESS J1825-137. This constitutes, especially for the standard On-Off region analysis approach of ground-based γ-ray astronomy, a problematic analysis situation, as a potential contamination of the analysis On-region due to emission from nearby sources can hardly be taken into account in an appropriate way. Therefore, the analysis presented in this work is based on an alternative likelihood template-fit analysis approach. The applied analysis procedure has the strong advantage of simultaneously taking into account the contributions of all sources which are located in the field of view. Thus, a morphological and spectral characterization of the individual components free of any contamination effects is reached, as the influence from neighboring emission regions is intrinsically taken care of. For this purpose, the GammaLib/ctools software framework, one of the high-level analysis software candidates for the future Cherenkov Telescope Array (CTA), was used and contributions to its further development have been achieved.

The spectral analysis presented in this work yields a significant detection of a high-energy cutoff in the energy spectrum of HESS J1826-130 with a best-fit cutoff energy of $18.0 \pm 4.6\,\mathrm{TeV}$. The reconstructed spectral index of 1.80 ± 0.13 illustrates the exceptional hardness of the emission. Assuming a hadronic emission scenario, a modeling of the measured TeV energy spectrum results in a cutoff energy estimate of $200\,(^{+217}_{-86})_{\mathrm{stat}} \pm 42_{\mathrm{sys}}\,\mathrm{TeV}$ for the parent proton spectrum. A 95% confidence level upper limit on the cutoff energy can be set at $\mathrm{UL}_{95} = 863 \pm 19_{\mathrm{stat,MC}} \pm 249_{\mathrm{sys}}\,\mathrm{TeV}$. These results show that the PeVatron hypothesis can most likely be ruled out. A view on the region in the multi-wavelength regime reveals HESS J1826-130 as a plausible pulsar wind nebula candidate, if associated with the energetic pulsar PSR J1826-1256, which is located in the immediate vicinity of the TeV source. However, the presence of dense molecular matter in combination with the knowledge of a previous supernova explosion in the near surrounding, which left behind HESS J1825-137, is to be seen as support for a hadronic emission scenario. Also the two nearby supernova remnants G018.6-00.2 and G018.1-00.1 might be connected to the TeV excess via a runaway cosmic ray scenario. Presumably, a reliable identification of the origin of the TeV emission of HESS J1826-130 will only become possible by future observations of the complex region with the CTA observatory, combined with an extended analysis in the multi-wavelength regime.

Kurzfassung

In der vorliegenden Dissertation wird eine detaillierte Analyse der unidentifizierten TeV-Gammastrahlungsquelle HESS J1826-130 präsentiert. Diese Strahlungsquelle wurde im Zuge des H.E.S.S. Galactic Plane Surveys detektiert und zeichnete sich dabei durch ein außergewöhnlich hartes Energiespektrum, ohne offensichtliche Anzeichen für einen Abbruch im erfassten Energiebereich, aus. Dieses Merkmal lässt, unter der Annahme eines hadronischen Emissionsszenarios, den Rückschluss auf einen hochenergetischen hadronischen Teilchenbeschleuniger, der Teilchen potentiell bis in den PeV-Energiebereich (10^{15} eV) beschleunigt, zu. Die Suche nach solch galaktischen PeVatron-Teilchenbeschleunigern stellt im Forschungsbereich der Hochenergie-Astrophysik eine der derzeitig zentralen Forschungsfragen dar. Nach einer intensiven Nachbeobachtung von HESS J1826-130 mit dem H.E.S.S. Instrument im Sommer 2015 steht ein erweiterter Datensatz zur Verfügung, der in dieser Arbeit verwendet wurde, um die Strahlungsregion morphologisch und spektral detailliert zu analysieren und den möglichen PeVatron-Charakter der Quelle weiter zu testen.

Die Emissionsregion HESS J1826-130 befindet sich räumlich in der unmittelbaren Nachbarschaft des im TeV-Energiebereich stark ausgedehnten und sehr hellen Pulsarwindnebels HESS J1825-137. Dies stellt insbesondere für den klassischen Analyseansatz der bodengebundenen Gammastrahlungsastronomie, der mit On-Off Regionen arbeitet, ein Hindernis dar, da eine potentielle Kontamination der Analyseregion durch weitere, räumlich nahe gelegene TeV Quellen hierbei nur schwer korrekt berücksichtigt werden kann. Aus diesem Grund wurde für die vorliegende Analyse mit einem Likelihood Modell-Fit ein alternativer Analyseansatz gewählt, der den Vorteil bietet, alle im Gesichtsfeld vorhandenen Quellen und deren Einfluss aufeinander simultan zu berücksichtigen. Damit wird eine morphologische und spektrale Charakterisierung der individuellen Komponenten frei von möglichen Kontaminationseffekten erzielt. Hierfür wurde die Software GammaLib/ctools, die einen der Kandidaten für die Analysesoftware des CTA Observatoriums darstellt, verwendet sowie Beiträge zu deren Weiterentwicklung geleistet.

Die in dieser Arbeit vorgenommene spektrale Analyse der Emissionsregion ergibt die signifikante Detektion eines Abbruchs des Energiespektrums von HESS J1826-130 bei einer Energie von 18.0 ± 4.6 TeV („best-fit cutoff energy“). Die außergewöhnliche Härte der Emission resultiert in einem rekonstruierten spektralen Index von 1.80 ± 0.13. Eine Modellierung des gemessenen TeV Spektrums basierend auf der Annahme eines hadronischen Emissionsszenarios lässt den Rückschluss auf einen Abbruch des zugrunde liegenden Protonenspektrums bei einer Energie von $200\,({}^{+217}_{-86})_{\mathrm{stat}} \pm 42_{\mathrm{sys}}$ TeV zu. Die obere 95 % Konfidenzgrenze beträgt $\mathrm{UL}_{95} = 863 \pm 19_{\mathrm{stat,MC}} \pm 249_{\mathrm{sys}}$ TeV. Die genannten Ergebnisse zeigen, dass die PeVatron-Hypothese mit hoher Wahrscheinlichkeit ausgeschlossen werden kann. Aus einer Betrachtung der Emissionsregion im Multiwellenlängenbereich ergibt sich, dass HESS J1826-130 in Verbindung mit dem räumlich nahe gelegenen und energetisch geeigneten Pulsar PSR J1826-1256 einen plausiblen Pulsarwindnebel-Kandidaten darstellt. Ein hadronisches Entstehungsszenario ist jedoch, insbesondere im Hinblick auf das Vorhandensein von dichtem molekularem Material in der Emissionsregion, nicht ausschließbar. In diesem Zusammenhang könnte HESS J1826-130 mit derselben Supernova-Explosion in Verbindung stehen, aus der auch HESS J1825-137 entstand. Alternativ kommen die beiden nahe gelegenen Supernovaüberreste G018.6-00.2 und G018.1-00.1 als lokale Teilchenbeschleuniger in Frage. Eine eindeutige Identifizierung des Ursprungs der TeV-Emission von HESS J1826-130 wird vermutlich erst mit Hilfe weiterer detaillierter Beobachtungen der komplexen Region durch das sich im Aufbau befindliche CTA Gammastrahlungs-Observatorium, in Kombination mit erweiterten Studien im Multiwellenlängenbereich, möglich sein.

Contents

1 Introduction

The research field of observational γ-ray astronomy has undergone an impressive development within the last 20 years and a variety of important new results has helped to establish it as one of today's major research subfields in high-energy astrophysics and astroparticle physics. Probing the highest energy range of the electromagnetic spectrum, the study of cosmic γ rays relates to the study of the most energetic, non-thermal processes taking place in the universe. The key science questions addressed by current modern γ-ray astronomy can, following Funk (2015), broadly be divided into four main areas: (a) Cosmic ray (CR) astrophysics, with a focus on the questions of acceleration mechanisms, particle spectra of accelerated CRs, which sources provide the bulk of Galactic CRs and which of them are able to accelerate up to PeV energies. (b) The search for dark matter (DM) via a detection of potential annihilation signals in γ rays, probing the nature of DM and its distribution throughout the Galaxy. (c) The study of relativistic outflows such as winds or jets in systems like active galactic nuclei (AGNs), γ-ray bursts (GRBs) and binary systems, trying to improve our understanding of the extreme environments of black holes and other massive compact objects. (d) The probing of fundamental cosmological questions like a violation of Lorentz invariance through a search for energy-dependent variations of the speed of light. The research presented in this thesis relates to topic (a), and a detailed introduction to it will be given in chapter 2. A more comprehensive overview of the other topics can be found in current review papers, e.g. Funk (2015); Degrange & Fontaine (2015) and references therein.

The energy range covered by current satellite-based instruments, such as the Fermi Large Area Telescope (LAT, Atwood et al. 2009), is commonly referred to as the high-energy domain, corresponding to photon energies up to about 100 GeV. Due to the rapid decline in the fluxes of the observed γ-ray sources with increasing photon energy, the collection area of these instruments, naturally limited to the size of a satellite, becomes simply too small to allow for an efficient operation at higher energies. The very-high-energy (VHE) range, referring to photon energies above this threshold, is studied by ground-based γ-ray observatories using indirect detection methods. When a VHE photon hits the Earth's atmosphere, a cascade of secondary particles forming an electromagnetic air shower is initiated. Imaging Atmospheric Cherenkov Telescopes (IACTs) such as Veritas (Holder et al. 2008), Magic (Aleksić et al. 2012) or H.E.S.S. (Hinton et al. 2004) detect this signal by sampling the Cherenkov light emitted by the secondary particles of these showers and have proven to be very successful. Since the detection of the first VHE γ-ray source in 1989, the Crab Nebula (Weekes et al. 1989), the number of TeV sources has grown to more than 200 today listed in the TeVCat online catalog of TeV astronomy (see Fig. 1.1, Wakely & Horan 2017). The VHE source population is naturally divided into two sub-populations, with the first one consisting of strong extragalactic TeV emitters such as AGNs or starburst galaxies. However, due to their large spatial distance, these sources appear as point-like sources to current IACT instruments. The second sub-population are the Galactic TeV emitters, encompassing source categories like pulsar wind nebula (PWNs), supernova remnants (SNRs) and the Galactic Center region. Being located much closer to the solar

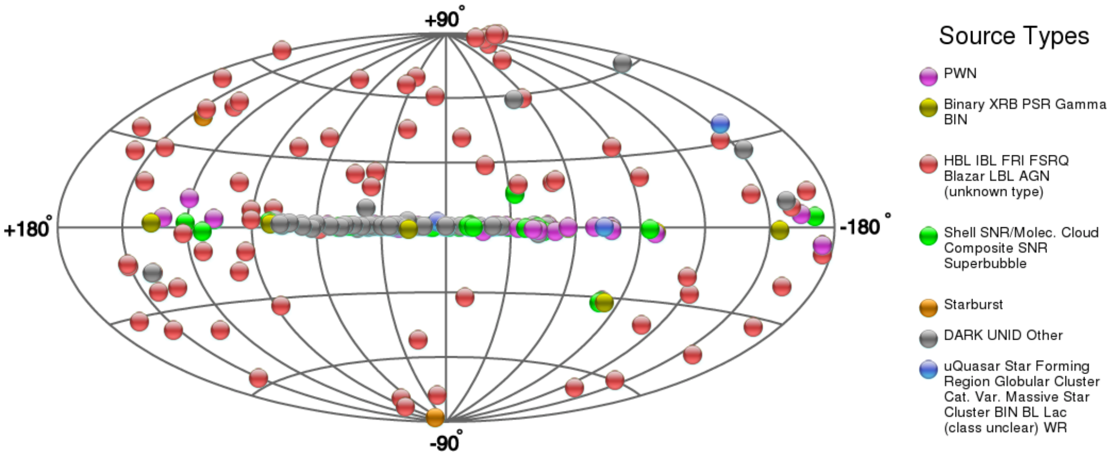

Figure 1.1: Distribution of known TeV γ-ray sources shown in Galactic coordinates (established and newly announced TeVCat catalog, status October 2017). Different source classes are indicated by different colors. The extragalactic source population is dominated by AGNs (red). The Galactic source population, clustered centrally along the Galactic plane, is clearly identifiable. A significant fraction of sources consists of not firmly identified (UNID) and dark sources, which means these sources could not yet be associated with any objects at a different wavelength. Image credit: TeVCat (Wakely & Horan 2017).

system, morphological and spectral analyses of these objects allow for detailed studies of the underlying astroparticle physical processes, causing the observable TeV emission. A non-negligible fraction of TeV sources also consists of not yet firmly identified and so-called dark sources, lacking an association with any other objects at a different wavelength. PWN are the most common class of identified Galactic VHE sources, the observable γ rays being produced via Inverse Compton (IC) scattering of highly energetic leptons, originating from the pulsar and scattering off ambient interstellar radiation fields. Hadronic CR particles can, besides leptonic ones, efficiently be accelerated in the expanding shock waves of SNRs, where γ rays might be produced in the interactions of these accelerated particles with ambient matter causing a bright TeV glowing. Also dense molecular clouds located in the near vicinity of SN explosions might get enlightened by highly energetic runaway CR particles producing a distinct γ-ray signal related to the physical properties of their parent particle population.

It is generally assumed that Galactic cosmic rays (CRs) are responsible for the flux of CRs measured on Earth up to about 3×10^{15} eV (3 PeV), the position of the knee in the CR energy spectrum (see chapter 2). This assumption requires the existence of Galactic particle accelerators that are able to accelerate hadronic particles up to the PeV energy range. The search for these so-called Galactic PeVatrons is one of the central questions of cosmic ray astrophysics, targeted by modern VHE γ-ray astronomy. Promising targets are TeV emitters showing a very hard energy spectrum up to ~ 100 TeV without incidence for a strong attenuation. This finding would, if the observed emission is of hadronic origin, point to a parent particle distribution of energies up to the PeV range.

This dissertation presents a detailed study of the PeVatron candidate source HESS J1826-130. The aim is to derive a precise characterization of the emission region in the VHE domain to allow, based on this characterization, for a further evaluation of the potential PeVatron character. This work is organized as follows: In chapter 2, an introduction to cosmic ray astrophysics and its close connection to γ-ray astronomy is given. Our current understanding of the CR energy spectrum is reviewed, pointing to the addressed topic of PeV particle acceleration. Chapter 3 summarizes the basic concepts of IACT ground-based γ-ray astronomy focusing on the H.E.S.S. instrument, which was used to take the data analyzed in this work. The likelihood-based analysis approach used in this thesis deviates from the classical region-based analysis approach of VHE γ-ray astronomy and is introduced with a short discussion of its status within the H.E.S.S. experiment. This thesis presents the first H.E.S.S. data analysis applying this new analysis technique to a complicated multi-source region, encompassing spatially extended, neighboring TeV sources. Chapter 4 begins with a detailed introduction to the analyzed field of view (FoV), including a discussion of the multi-wavelength (MWL) surrounding. The results of the data analysis from the VHE range are presented and discussed. A comprehensive verification of these results and checks on the new analysis procedure are given. In chapter 5, a modeling of the emission of HESS J1826-130 using the measured TeV energy spectrum is presented. Based on these results and a consideration of the surrounding MWL sources, different possible origins of the emission are identified and discussed. The last chapter summarizes the contents of this work and gives a concluding outlook.

2 Gamma-ray astronomy in the context of cosmic ray astrophysics

This chapter summarizes the current status of our basic understanding of CR astrophysics and outlines its close connection to γ-ray astronomy. A basic introduction and overview to the field of research is followed by a detailed discussion of the CR energy spectrum measured locally on Earth (section 2.1). This topic is naturally connected to the question of the origin of CRs and potential acceleration mechanisms. Alongside, the question of PeV particle acceleration taking place in our Galaxy is raised. A discussion of the experimental detection of such Galactic PeVatron accelerators using VHE γ-ray astronomy forms the second part of this chapter (section 2.2). Briefly, the basic nature of cosmic γ-ray photons is highlighted, followed by a description of their production in the interaction processes of CR particles, putting γ rays in the context of secondary messenger particles for CR astrophysics. Finally, the search strategy for Galactic PeVatrons in VHE γ rays is discussed.

2.1 Cosmic rays

In 1911 and 1912, Victor Hess made several balloon flights in which he studied the ionizing radiation of the atmosphere. At that time, the prevailing theory was that all the ionizing radiation is connected to natural radioactivity originating from the rocks of the Earth, hence being of terrestrial origin. However, in his experiments, which reached total heights of about 5 km, Hess discovered that after the expected initial decrease in the ionization rate with increasing altitude, it rises again significantly in heights above ~ 1 km. This finding led him to the conclusion that in addition to the terrestrial radiation coming from the ground, there must be some new kind of ionizing radiation originating from outside the Earth's atmosphere. For this discovery of cosmic radiation, or cosmic rays, Hess was awarded the nobel prize in 1936 (cf. Grupen 2000). Ever since, a huge scientific effort, including the operation of various different experiments, was driven by the questions raised by this discovery. A study of CRs as observed here on Earth, like the locally measured energy spectrum or composition, provides a direct insight into the related astrophysical processes, such as acceleration mechanisms or transport phenomena. The overall measured flux level allows an estimation of the total energy amount needed to sustain the locally measured, constant flux of CRs, which can be set in relation to the energy content of potential source candidates. These aspects will be discussed in more detail in the following sections.

2.1.1 Basic introduction

CRs can be subdivided into *primary* CRs, particles accelerated in astrophysical sources, and *secondary* CRs, which are created in interactions of primary CRs with their surrounding. Primaries are electrons, protons and helium, as well as heavier nuclei synthesized in stars (e.g. carbon, oxygen, iron). Nuclei which are not abundant end-products of stellar nucleosynthesis are secondaries. Positrons and anti-protons, so far the only detected antimatter particles of CRs, are typically thought to be of secondary origin. However, the question whether a tiny fraction of them might be primaries or not is an active topic of current research (cf. Patrignani & Particle Data Group 2016). Cosmic neutrinos and γ rays are also secondary particles in the sense that they are produced in the interactions of (predominantly) primary CRs with ambient matter or stellar radiation fields. However, the term cosmic rays is usually used to refer to the extraterrestrial flux of massive, charged particles. This is the convention which is followed throughout this thesis.

CRs are either measured by satellites and balloon based experiments ($E \lesssim 1\,\mathrm{TeV}$) or by ground-based air-shower experiments. About 98% of the incident particles are protons and heavier nuclei, about 2% are electrons. The positron flux is at a level of ~ 10% of the electrons, the anti-proton to proton fraction is about 10^{-4}. Within the group of protons and heavier nuclei, protons are the most abundant species (~ 87%), followed by helium nuclei (~ 12%), whereas heavier nuclei make up the remaining ~ 1% (Longair 2011).

The composition and energy spectrum of CRs can be interpreted in terms of propagation, given the assumption that the sources of Galactic CRs are located within our Galaxy. Being charged, CR particles are deflected by irregular interstellar magnetic fields during propagation, making high isotropy a distinct feature of CRs measured on Earth. Yet, with rising energy, anisotropies are to be expected, and current experiments detect CR anisotropy at a level of 10^{-3} at energies around a few TeV (Patrignani & Particle Data Group 2016). Generally, the basic propagation of CR particles can be described by a diffusion model with possible inclusion of convection. Additionally, energy and particle loss mechanisms (e.g. spallation of heavy nuclei) have to be taken into account. The basic transport equation of CRs can be written as (Longair 2011):

$$\frac{\partial n_i(E,\vec{r},t)}{\partial t} = D\nabla^2 n_i + \frac{\partial}{\partial E}\left(b(E)n_i\right) + Q_i - \frac{n_i}{\tau_i} + \sum_{j>i}\frac{P_{ij}}{\tau_j}n_j \tag{2.1}$$

where n_i is the number density of CR nuclei of species i with energy E at position $\vec{r}$. The first term on the right hand side of Eq. 2.1 is the diffusion term, the second one takes into account energy gains or losses, $b(E) = -\mathrm{d}E/\mathrm{d}t$. Q_i is the source term (injection rate), while the last two terms describe gains and losses through spallation processes. $\tau_{i,j}$ are the spallation lifetimes of species i and j, while the spallation of all species with $j > i$ contributes to n_i. P_{ij} denotes the probability for species i being created in an inelastic collision of nucleus j. For a more detailed and general discussion of CR transport see e.g. Strong et al. (2007) and references therein. Often, simplifying assumptions and basic considerations provide valuable insight to the understanding of experimentally observed CR data, like the slab and the leaky box models allow for a basic explanation of the chemical CR nuclei abundances, the observed energy dependent primary to secondary ratio, or an estimate of the characteristic age of Galactic CRs ("radioactive cosmic ray clocks"). The basic results of these considerations are outlined in the following:

- CR element abundances compared to the solar system:
  The element abundances of CR nuclei compared to the corresponding abundances in the solar system differ considerably in three points:
  - The light elements lithium, berillium, boron are overabundant in CRs.
  - There is an excess abundance in CR elements just lighter than iron.

  - The ratio of ^{3}He to ^{4}He.

  All observed differences can be explained by the production of the secondary particles in spallation processes of primary CRs, while typical traversed path lengths are about $\xi = 4.8\,\mathrm{g/cm^2}$ (cf. Longair 2011). Assuming a particle velocity equal to the speed of light c and a matter density of the interstellar medium $\rho_{\mathrm{ISM}} = 1\,\mathrm{proton/cm^3}$, this allows an estimate of the Galactic CR escape time τ_{escape}:

$$\tau_{escape} = \frac{\xi}{c\,\rho_{\mathrm{ISM}}} = \frac{4.8\,\mathrm{g/cm^2}}{3\times10^{10}\,\mathrm{cm/s}\times1.7\times10^{-24}\,\mathrm{g/cm^3}} = 3\times10^{6}\,\mathrm{years}. \tag{2.2}$$

- Unstable secondary particles:
  The ratio of radioactive secondary isotopes like ^{10}Be relative to the isotopes in which they decay to allow also for a derivation of the mean characteristic escape time of Galactic CRs: $\tau_{escape} \sim 10^7$ years (Longair 2011), which is in rough agreement with the one calculated before.
- Energy dependence of secondary to primary ratios:
  The energy dependence of the abundance ratio of primary to secondary nuclei such as the B/C ratio can be explained by an energy-dependent escape time (diffusion coefficient), meaning that higher energetic particles diffuse faster. This also implies that transport effects will alter the spectral slope of the initial particle spectra.
- CR Source energy rate:
  From the mean CR energy density $\omega_{\mathrm{CR}} = 1\,\mathrm{eV/cm^3} = 1.6\times10^{-12}\,\mathrm{erg/cm^3}$, one can calculate the mean energy injection rate required to sustain the flux of Galactic CRs using the mean characteristic escape time:

$$\dot{E}_{CR} = \omega_{\mathrm{CR}}\,V_{\mathrm{Gal}}/\tau_{escape} \sim 3\times10^{48}\,\mathrm{erg/yr}, \tag{2.3}$$

  assuming a galactic radius of 10 kpc. This energy injection rate must be provided by the sources of CRs.
- Diffusive CR propagation:
  The calculated characteristic escape times for CRs leaving the volume of our Galaxy can be seen as strong experimental proof of a non-ballistic, diffusive propagation of CRs, as it exceeds the ballistic propagation time scales by orders of magnitude.

In the picture of diffusing CRs originating from sources located in our Galaxy, it is reasonable to assume that at a certain energy, particles will not anymore be efficiently confined to the volume of the Galaxy and start to escape rather quickly. This aspect is mirrored in the energy dependence of the B/C ratio and will become more evident in a detailed discussion of the CR energy spectrum in the following section.

2.1.2 The energy spectrum of cosmic rays

The central discussion of this section is focused on the energy spectrum of hadronic CRs (protons and heavier nuclei), usually just referred to as the CR energy spectrum. Electrons, positrons and anti-protons require a separate treatment and are discussed afterwards.

Energy spectrum of cosmic ray protons and nuclei

The differential energy spectrum of CRs as a function of energy per nucleus is shown in Fig. 2.1. It extends from about 10^9 eV up to 10^{20} eV, spanning a remarkable range of 11 orders of magnitude in energy. For energies E $\lesssim 10^{10}$ eV, the spectrum is affected by the Earth's magnetic field and solar winds. This leads to a cutoff at the lowest energies and a periodical modulation following the solar cycle. Above this energy range, the overall spectral shape is well described by a power law, $\mathrm{d}N/\mathrm{d}E = C \cdot E^{-\alpha}$, while a representation scaled by $E^{2.6}$ (see Fig. 2.2) clearly reveals the positions of spectral breaks. At an energy of about $10^{15.5}$ eV, the spectrum steepens considerably with a change in the spectral index from about 2.7 to 3.1, which marks the position of the so-called *knee*. At around $10^{18.5}$ eV, the so-called *ankle*, the spectrum hardens again, while a cutoff can be observed at the highest energies. The common interpretation of these spectral features is given under the assumption of a Galactic CR population, originating from sources located within our Galaxy, which merges into an extragalactic component at the highest energies around the ankle. The observed changes in the spectral shape are attributed to intrinsic source properties as well as propagation effects.

One of the most popular explanations of the spectral steepening around the knee correlates the feature to the maximum attainable acceleration energy of the Galactic CR sources. A change observed in the chemical composition around the knee stimulates the interpretation of it representing preceding cutoffs in the spectra of different nuclei, as the typical acceleration mechanisms are rigidity dependent: if the maximum proton energy is $E_{p,\max} = 3 \times 10^{15}$ eV, then iron nuclei are accelerated up to $E_{Fe,\max} = 26 E_{p,\max} \sim 10^{17}$ eV (e.g. Hörandel 2004; Blasi & Amato 2012; Gaisser et al. 2013). However, Hillas (2005) pointed out that a single Galactic population seems to cutoff too sharply to explain the spectrum from the knee up to the ankle, which requires another, higher energetic Galactic CR component. This second Galactic component might also explain the recent observation of the so-called *second knee*, a slight steepening of the energy spectrum between the knee and the ankle, located at around 10^{17} eV (see also Gaisser et al. 2013; Thoudam et al. 2016). The diffusive propagation typically affects the overall shape of the particle spectrum: as more energetic particles diffuse faster, a steeper spectrum is observed on Earth compared to initial source injection spectra. However, it has also been shown that the knee might be explained exclusively by propagation effects (e.g. Ptuskin et al. 1993; Roulet 2004).

The ankle is usually taken to indicate the contribution of an extragalactic component, merging into the steeply falling Galactic one. In this context, it is illustrative to calculate the gyroradius r_G of a highly energetic proton of charge e in a magnetic field of strength B, using a typical Galactic magnetic field strength of about $3\,\mu$G:

$$r_G = \frac{E}{c\,e\,B} = \frac{10^{18.5}\,\mathrm{eV}}{c\,e\,(3\,\mu\mathrm{G})} \approx 1000\,\mathrm{pc}\ , \tag{2.4}$$

which exceeds the vertical height of around 300 pc of our Galaxy. This result shows that ultra-high-energy (UHE, $E \gtrsim 10^{18}$ EeV) CRs are not confined to the volume of our Galaxy anymore and hence the influence of a potential extragalactic component is expected to be observed. The energy range from the knee up to the ankle is classically thought to be connected to the transition between the vanishing Galactic population and the clear domination of an extragalactic component. Currently, three different kinds of models which explain the transition from Galactic to extragalactic CRs are discussed: ankle, dip, and mixed composition models (Aloisio et al. 2012 and references therein).

The ankle model follows the traditional interpretation, in which the transition occurs

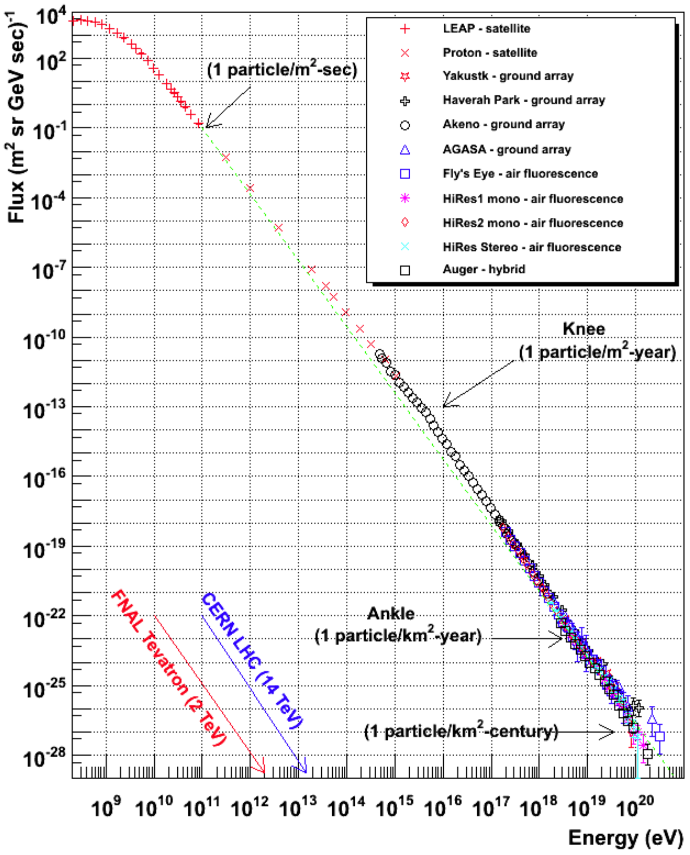

Figure 2.1: Differential all-particle energy spectrum of cosmic rays (protons and heavier nuclei) as measured by various experiments. The prominent features, the *knee* and the *ankle*, are marked, and corresponding particle arriving frequencies are indicated. The energy scales, reached by current accelerator experiments are also referenced. Image credit: W. Hanlon, `http://www.physics.utah.edu/~whanlon/spectrum.html`.

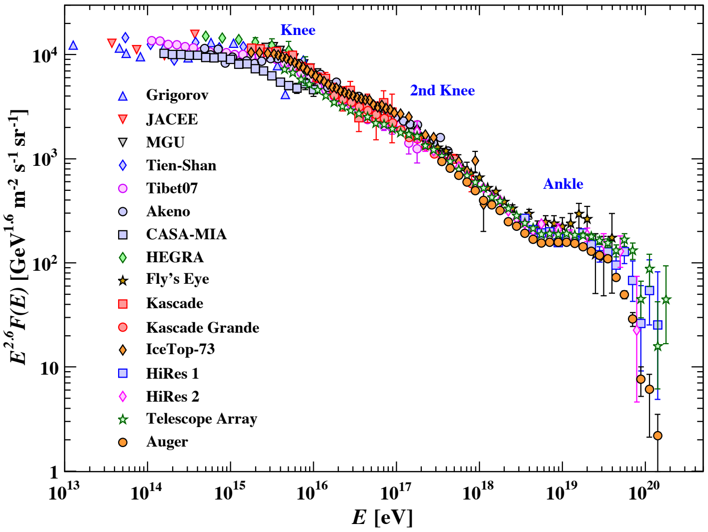

Figure 2.2: All-particle cosmic-ray energy spectrum above 10^{13} eV, scaled by $E^{2.6}$. Image taken from Patrignani & Particle Data Group (2016).

where the ankle is observed. It needs a second Galactic component to describe the high energy part of the spectrum between the knee and the ankle and is dominated by a heavy iron component at energies just before the transition regime (~ 1 EeV, Fig. 2.3). This is however in tension with composition measurements of the Pierre Auger Observatory (Abraham et al. 2009, 2010) and the HiRes detector (cf. Sokolsky & HiRes Collaboration 2011), see Fig. 2.4. Both experiments measure a proton (or light nuclei) dominated composition in an energy range of $(1-5)$ EeV.
In the dip model (Berezinskii & Grigor'eva 1988), the transition from Galactic to extragalactic CRs occurs much earlier in energy, at about the position of the second knee. It is characterized by a sharp composition change from a heavy Galactic iron component to extragalactic protons.

The early onset of the extragalactic component is attenuated by pair-production processes in which the protons interact with cosmic microwave background (CMB) photons:

$$p + \gamma_{\mathrm{CMB}} \rightarrow p + e^- + e^+ \ . \tag{2.5}$$

The ankle appears as an intrinsic part of the dip. The following sharp cutting off of the spectrum at around 10^{20} eV is also explained by interactions of the extragalactic protons with the CMB, by the famous GZK (Greisen 1966; Zatsepin & Kuz'min 1966) reaction:

$$p + \gamma_{\mathrm{CMB}} \rightarrow \pi + X. \tag{2.6}$$

The threshold energy is around 60 EeV, well in agreement with the observation. The pair production process and the GZK cutoff are signatures of protons, and recent measurements of HiRes (Fig. 2.4) and the Telescope Array (Tinyakov 2014) seem to confirm a proton dominated ultra-high-energy composition, which can be considered as experimental evidence supporting the dip model. However, this is in disagreement with measurements by the Pierre Auger Observatory (Fig. 2.4 and more recently Aab et al. 2017), which tend to an iron dominated ultra-high-energy composition.
Mixed composition models allow for a mixed composition in the extragalactic component similar to the abundances of Galactic CRs (proton and helium being the dominant components). Transition can occur at the ankle or below it down to the second knee, with the exact position being parameter-dependent. Because of photo-disintegration of heavy nuclei on the extragalactic background light, the extragalactic composition becomes generally lower at $E > 10$ EeV, making the GZK feature also present in most of the mixed composition models (Aloisio et al. 2012). It is however important to notice that if the UHE extragalactic component would be iron dominated, the high energy cutoff could be explained solely by photo-disintegration processes, without the need for the GZK effect (Stecker & Salamon 1999).

To shortly summarize, the current status is as follows: There is the general consensus that CRs up to the second knee are of Galactic origin. This requires the existence of Galactic particle accelerators which reach at least energies up to where the knee is observed at around $10^{15.5}$ eV – that is *particle acceleration up to PeV energies.* There is common agreement that the observed UHE CRs are of extragalactic origin. The transition from the Galactic to the extragalactic component is in all discussed models located at the energy range of the second knee up to the ankle. Up to the present, the situation concerning the mass composition in the UHE range, which is the main property used to discriminate between the different discussed transition scenarios, remains unclear due to disagreeing measurements of different experiments.

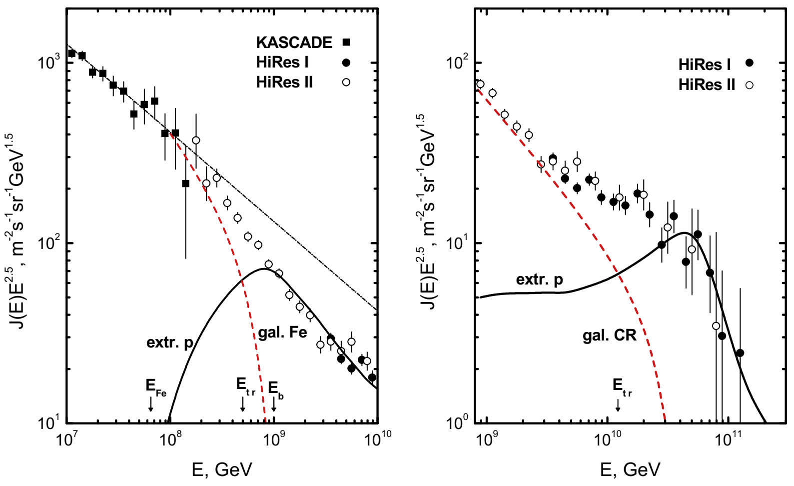

Figure 2.3: Transition in the dip (left) and the ankle (right) models. In both models, the red dashed line depicts the Galactic iron component, the black solid line the extragalactic proton component. E_{tr} marks the transition energy (intersection point), which is considerably smaller in the dip model than in the ankle model. E_{Fe} depicts the position of the iron knee, E_{b} the position at which the transition is completed (left panel). Image taken from Aloisio et al. (2012).

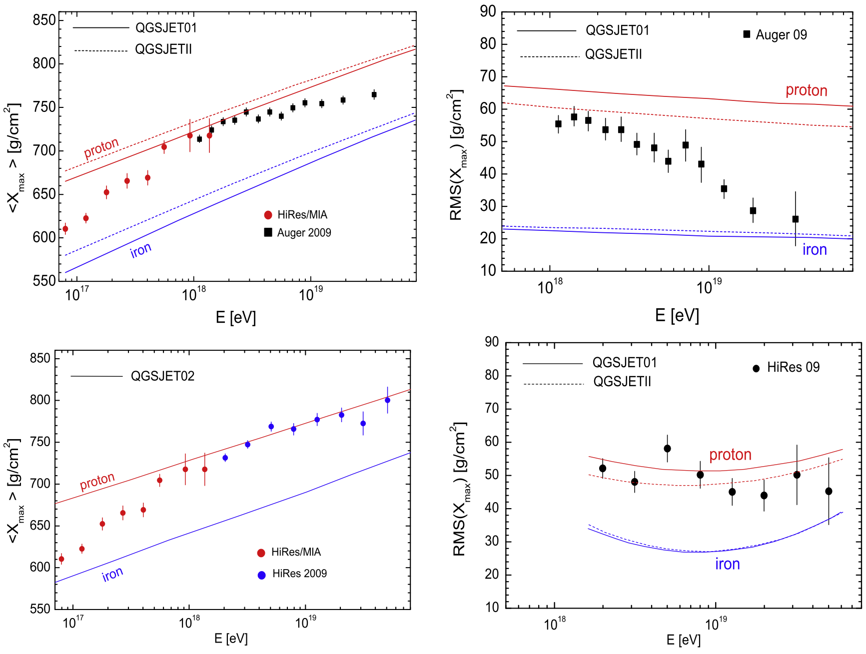

Figure 2.4: Pierre Auger Observatory (top) and HiRes (bottom) measurements of the mass-composition dependent quantity atmospheric depth X_{max} (left) and its root mean square (RMS) as a function of energy. The calculated values for protons and iron for different interaction models are shown as well. At energies $E \gtrsim 10\,\mathrm{EeV}$, the measurements differ significantly, with the Auger data pointing to an iron dominated population at the highest energies. The HiRes data suggest a proton dominated composition. Images taken from Aloisio et al. (2012).

Energy spectrum of cosmic ray electrons/positrons

The leptonic component of CRs is, due to the small electron mass, subject to strong radiative (synchrotron and Inverse Compton) energy losses during propagation. This is reflected in a much steeper spectrum with a spectral index of about 3.1 compared to about 2.7 for the hadronic component, see Fig. 2.5. The radiative cooling time of TeV electrons in the interstellar medium is about 10^5 years (cf. section 2.2.1), which limits the distances of potential sources to a few hundreds of parsecs, e.g. Atoyan et al. (1995). The aforementioned authors conclude that the measured TeV electrons indicate the existence of at least one nearby ($r \leq 100\,\mathrm{pc}$), young source of accelerated electrons. The entire spectrum is explained by assuming that this component dominates at high energies ($E \gtrsim 1\,\mathrm{TeV}$) over the bulk population of electrons which is produced at distant ($\geq 1\,\mathrm{kpc}$), in time and space uniformly distributed Galactic sources.
The positron fraction $C_+ = F(e^+)/(F(e^+)+F(e^-))$, which is the ratio of the positron flux relative to the total flux of positrons plus electrons, is shown in Fig. 2.6. The rise of C_+ above 10 GeV cannot be explained by models assuming the production of e^+ exclusively as secondary particles. However, if a potential nearby e^- source was a source of (e^+, e^-) pairs (like a nearby pulsar), this rise would naturally be explained. Alternative discussed models propose propagation effects (e.g. Gaggero et al. 2013) as well as dark matter annihilation processes (e.g Ibarra et al. 2013; Di Mauro et al. 2016).
Hence, the leptonic component gives, in comparison to the hadronic one, a supplementary probe of CRs, which can be seen to pose its own, to some extend separate, questions within CR astrophysics.

Anti-protons are, apart from positrons, so far the only detected antimatter particles in CRs. The overall proton to anti-proton ratio is about 10^{-4}, and shows a strong dependence on the solar cycle (e.g Asaoka et al. 2002). There is an overall agreement that most of the measured anti-protons are of secondary origin. However, uncertainties surrounding the knowledge about cross sections of relevant production processes as well as of models for propagation make correct interpretations still a challenging task. CR anti-protons will not be further discussed in this work, for details see Strong et al. (2007); Winkler (2017), and references therein.

2.1.3 The origin of cosmic rays: A key science question

The preceding section presented a discussion of CRs from an experimental point of view, which is preliminarily based on measurements of the differential energy spectrum. The basic conclusions resulting from these measurements have been outlined and require a discussion in an astrophysical context. The main question, which has been omnipresent in CR physics since their very first discovery, is usually put this way:

What is the origin of CRs?

This question implicitly entails a complex subset of questions: Where do the particles originate from? Which are the astrophysical objects in which acceleration occurs? What are the related acceleration mechanisms? This section presents a basic introduction to this topic, focused on the hadronic component of Galactic CRs, as it refers to the research subject addressed in this work.

From an experimental point of view, the following basic requirements for the sources of Galactic CRs can be drawn (cf. preceding discussion):

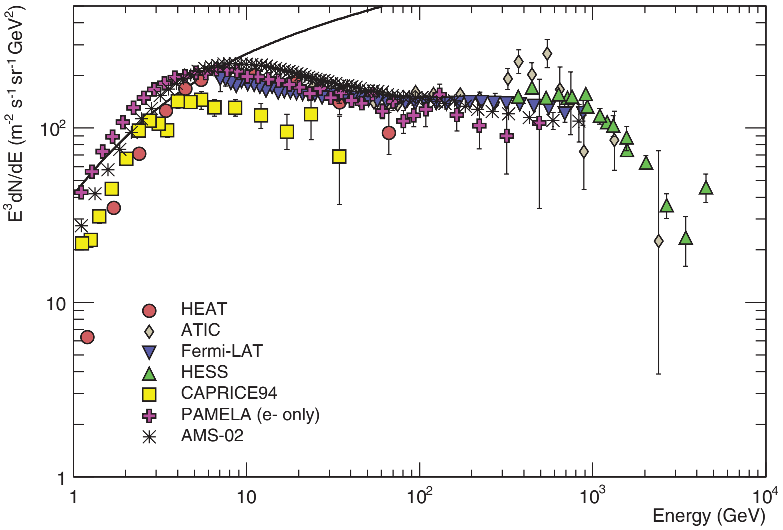

Figure 2.5: Energy spectrum of CR electrons plus positrons (except PAMELA data which show the electron-only spectrum). Note the applied scaling factor of E^3. The black solid line shows the proton spectrum, multiplied by 0.01. Image taken from Patrignani & Particle Data Group (2016).

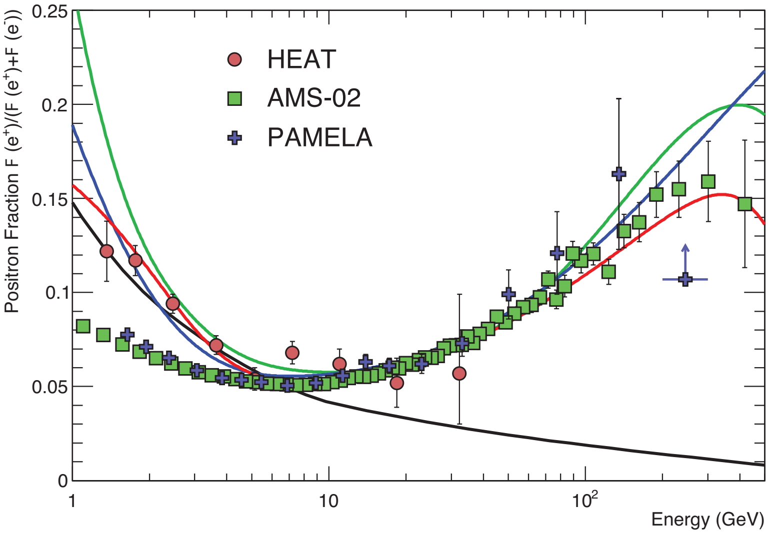

Figure 2.6: Measured positron fraction, i.e. the ratio of the e^+ flux relative to the total flux of e^+ and e^-. The black line represents a model of pure secondary e^+ production. The three colored lines correspond to models invoking dark matter decay (green), propagation physics (blue) and primary production in a pulsar (red). Image taken from Patrignani & Particle Data Group (2016).

- Provide a mean energy injection rate of $\sim 3 \times 10^{48}$ erg/yr.
- Power law energy spectrum with spectral index around 2.2.
- Particle acceleration at least up to the *knee*, i.e. up to PeV (10^{15} eV) energies.

Supernova remnants as sources of cosmic rays

Supernovae (SN) have been proposed to relate to the origin of CRs for the first time by Baade & Zwicky (1934), followed by Ginzburg & Syrovatskiy (1961). Today, there are strong theoretical and observational arguments which make young supernova remnants (SNRs) good candidates for acceleration up to the knee within the Galaxy, which will be discussed in more detail in the following.

The first key aspect is that SNRs are able to provide the experimentally derived energy rate. The amount of kinetic energy released in a typical SN explosion is about 10^{51} erg. The mean rate of SNRs in the Galaxy is assumed to be about $2-3$ per century. Hence, the required energy injection rate is well covered, assuming about 10% of the kinetic energy release can effectively be converted into particle acceleration.

The second key aspect is the fact that SNRs provide an appropriate mechanism for particle acceleration. The basic idea of this mechanism goes back to Fermi (1949), who proposed that charged particles can gain energy by scattering off magnetized interstellar clouds acting as randomly moving magnetic mirrors. This scattering leads to an average energy gain per collision of $\Delta E/E \sim (v/c)^2$, assuming that these mirrors move randomly with velocity v and the particles move with velocity c. The Fermi acceleration mechanism is in its original version, due to the second order in the velocity ratio, rather inefficient. The basic problem are tail-on collisions, in which particles might also lose energy. However, the mechanism can get quite efficient if only head-on collisions would apply, in a restricted area, granting for an efficiently large number of scatterings per time interval. It was in the late 1970s that a number of researchers independently realized that such conditions apply at strong shock fronts like those of expanding SNRs (Krymskii 1977; Axford et al. 1977; Bell 1978; Blandford & Ostriker 1978). In the so-called *diffusive shock acceleration* (DSA) mechanism, highly energetic charged particles are trapped between magnetic irregularities present on both sides of an astrophysical shock, which leads to numerous (head-on) scatterings. The average energy gain per crossing is shown to be $\Delta E/E \sim (v/c)$, i.e. in first order of v/c, which allows for a much more rapid acceleration. The second key feature of the DSA mechanism is that it automatically results in a number spectrum of the accelerated particles, which follows a *power law*: $\mathrm{d}N/\mathrm{d}E \sim E^{-\gamma}$ with γ depending on the shock compression ratio r: $\gamma = (r+2)/(r-1)$. For strong, highly supersonic moving shocks, $r = 4$, which yields a spectral index of $\gamma = 2$, very close to the required value.
The maximum energy which can be reached in DSA is related to the strength of the magnetic field which confines the particles to the shock area. Recent results of nonlinear DSA, taking into account the interaction between the accelerating particles and the shock, propose magnetic field amplifications up to a factor of 10^3 due to CR driven instabilities (e.g. Bell & Lucek 2001), allowing for magnetic field strengths of $100-1000\,\mu$G. Such magnetic field amplifications could in turn allow for particle acceleration up to PeV energies and possibly well beyond. In SNRs, these highest energies are supposed to be reached in the first few hundred years, early in the free expansion phase. In this phase, the shock speed is appropriately high to stimulate strong magnetic field amplifications and to allow for a sufficiently high acceleration rate (e.g. Hillas 2006; Schure & Bell 2013; Gabici & Aharonian 2007). In conclusion, young SNRs with ages < 1000 years are prime candidates for

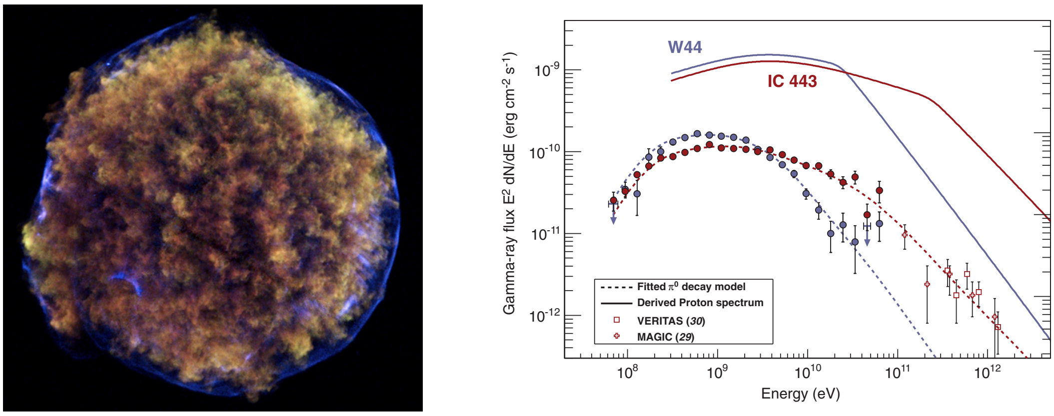

Figure 2.7: *Left:* Composite Chandra X-ray image of Tycho's SNR (SNR 1572). Energy-color coding: Red 1.6-2.0 keV, Green 2.2-2.6 keV, Blue 4-6 keV. The sharp blue rim filaments are produced by highly energetic electrons which have been accelerated in the expanding shock wave of the SNR by the DSA mechanism. The low energy X-rays in red and green trace the expanding debris of the SNR. Image credit: NASA/CXC, Lu et al. (2011).
Right: Secondary γ-ray spectra of the SNRs W44 and IC443 measured with the Fermi satellite. The characteristic pion bump (low-energy) cutoff at around $200 - 300\,\mathrm{MeV}$, yielding experimental proof for the acceleration of hadronic CRs in the shock waves of SNRs, is clearly detected. Inferred primary proton spectra as well as fitted π^0 models are also shown. Image credit: Ackermann et al. (2013).

acceleration up to PeV energies and beyond.

From an experimental point of view, magnetic field amplification in the shocks of young SNRs is verified by observations of narrow shells of non-thermal X-ray emission (Fig. 2.7). These thin rims are interpreted as the shock waves of the SNRs, in which electrons are accelerated to very high energies. Due to the strong magnetic fields, the particles suffer strong synchrotron losses, so that they lose all their energy in the immediate vicinity of the shock. Field strengths with typical values of several hundreds of μG, up to a few mG have been inferred from such observations (e.g. Vink & Laming 2003; Völk et al. 2005).

The detection of the *pion bump* for the SNRs W44, IC443 (Giuliani et al. 2011; Ackermann et al. 2013) and W51C (Jogler & Funk 2016) very recently provided the unambiguous experimental proof that besides electrons, also hadronic CRs are accelerated in the shock waves of SNRs. The characteristic low-energy cutoff found at around $200 - 300\,\mathrm{MeV}$ in the energy spectrum of secondary γ rays is an unmistakable signature for the decay of neutral π^0 mesons which are produced by highly energetic hadronic CRs interacting with ambient matter (see section 2.2.1).

In summary, there is strong experimental and theoretical evidence for the acceleration of CRs in SNRs. However, non-linear DSA is an active field of research and a detailed understanding is still under development, whilst from an experimental point of view, a crucial problem remains open: none of the so far observed SNRs show clear observational evidence for acceleration up to PeV energies and beyond (for an extended overview, see Aharonian 2013; Funk 2015). Moreover, the problem of an unambiguous identification of the origin of secondary γ rays, used to trace the accelerated CRs (cf. section 2.2.1) poses an additional challenging experimental task, especially at the highest energies. In consequence, the question if SNRs are really the sources that provide the bulk of Galactic CRs up to the knee is still not resolved.

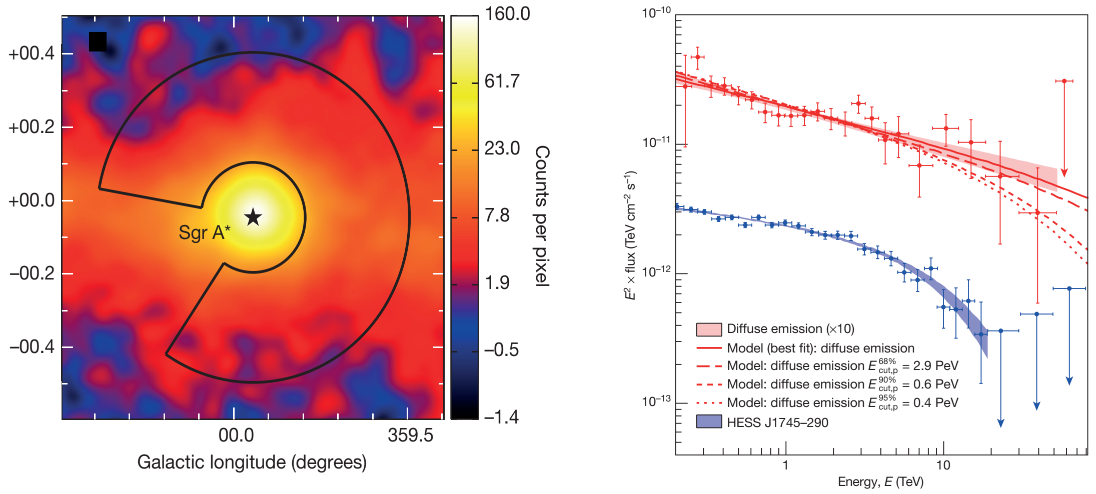

Figure 2.8: *Left:* VHE γ-ray emission at the Galactic Center measured by H.E.S.S. The analyzed diffuse emission region around the central source HESS J1745-290 is depicted by the black contour line. The position of Sgr A* is marked by a black star.
Right: Reconstructed spectrum of the diffuse emission, together with best-fit models for a hadronic emission scenario. The spectrum of the central source is shown for comparison. The hard diffuse γ-ray excess, extending up to several tens of TeV without clear indication for a cutoff, is seen as evidence for particle acceleration up to PeV energies. Image credit: H.E.S.S. Collaboration et al. (2016).

General discussion

The first experimental detection of PeVatron particle acceleration in our Galaxy was claimed very recently by the H.E.S.S. Collaboration (H.E.S.S. Collaboration et al. 2016), presenting a detailed analysis of diffuse γ-ray emission in the direct vicinity of the supermassive black hole Sgr A* in the Galactic Center (Fig. 2.8). The authors suggest the central black hole itself as the most plausible supplier of ultra relativistic protons and nuclei, which are thought to cause the diffuse γ-ray excess. The evidence for acceleration up to PeV energies is inferred from the measured γ-ray spectrum, which is best characterized by a power law with a photon index of ~2.3 extending up to tens of TeV, without a cutoff or a break. Particle acceleration could have taken place in strong shocks formed in the accretion flow (Aharonian & Neronov 2005; Istomin 2014) or further away from the very central region of Sgr A*, at termination shocks (Atoyan & Dermer 2004). An important conclusion made in the publication is the following: If Sgr A* is the responsible particle accelerator, it should have been more active in the past to be able account for the measured γ-ray flux. If Sgr A* was indeed more active for the last $10^6 - 10^7$ years, providing an average acceleration rate of about 10^{39} erg/s, the entire flux of Galactic CRs around the knee at about 1 PeV could be attributed solely to Sgr A*. This explanation "could be a solution to one of the most controversial and actively debated problems of the paradigm of the SNR origin of Galactic cosmic rays", to quote H.E.S.S. Collaboration et al. (2016).

Besides providing a competitive scenario for the SNR origin of Galactic CRs, such observations of the Galactic Center fill the gap to particle acceleration in extreme environments such as black holes, where acceleration is typically thought to be connected to relativistic outflows like strong winds or jets. Objects like binary systems, AGNs, and γ-ray bursts (GRBs) are related to these phenomena and constitute prominent sources of non-thermal emission at different wavelengths. AGNs and GRBs are among the generic prime candidates discussed as the sources of extragalactic CRs. For an extended review on particle acceleration in relativistic outflows, see e.g. Bykov et al. (2012).

In this section, it was outlined that SNRs are good candidates to be the sources which provide the bulk of Galactic CRs up to the knee and beyond, however clear experimental proof of this hypothesis, referred to as supernova paradigm, is still lacking. From very recent observations of the Galactic Center region, one might deduce a competitive scenario with only one single powerful Galactic particle accelerator, Sgr A*, which, if so, must have been much more active in the past. However, also this scenario might be questionable.

Our understanding concerning the origin of Galactic CRs improved a lot in the very recent years, but a definitive answer remains an open question - meaning *the hunt for the origin of Galactic CRs, i.e. the hunt for Galactic Pevatrons, is still ongoing.* The close connection between the search for these sources and γ-ray astronomy has already been signified: the presented, important experimental findings are driven by γ-ray observations which allow for conclusions about the underlying particle astrophysics. This connection will be discussed in detail in the following chapter.

2.2 Search for Galactic PeVatrons in very-high-energy gamma rays

The close connection between cosmic ray astrophysics and γ-ray astronomy has already been implied by the fact that the presented experimental results concerning the question about the origin of Galactic CRs are derived from observations in high and very-high-energy γ rays.

This close connection relates to the fact that cosmic γ rays are produced only in the interactions of highly energetic charged CR particles with ambient matter or interstellar radiation fields. Once produced, the neutral γ-ray photons travel on straight lines through the ISM, pointing directly back to their point of origin. This property provides the opportunity to reveal and study the sites of production, acceleration and interaction of CRs indirectly: γ rays serve as secondary messenger particles, used to study the physical properties of the underlying parent particle population and related astrophysical processes. The information provided by the study of secondary cosmic γ rays cannot be gained from direct observations of CRs on Earth, as the charged CR particles get deflected by irregular interstellar magnetic fields, which leads to a strongly isotropized CR flux.

Depending on the nature of the underlying parent particles, one distinguishes between hadronic or leptonic (electronic) origin of γ rays. The relevant production processes will be discussed in the following section. Based on this overview, a discussion about the search for Galactic PeVatrons in VHE γ rays, which relates to the research focus of this work, will be given.

2.2.1 Origin of cosmic gamma rays

Leptonic origin of γ rays

Electrons or positrons produce γ rays preliminary via Inverse Compton (IC) up-scattering of ambient photon fields. Among the target photon fields are the cosmic microwave background (CMB) as well as infrared or optical ISM radiation fields.

Two different domains are distinguished for IC scattering: the Thomson regime, in which the energy of the photon in the electron rest frame is much smaller than the electron rest mass ($\hbar\omega' \ll mc^2$). The electron is given only a small recoil in the scattering and loses its energy continuously. The opposite extreme is referred to as deep Klein-Nishina (KN) regime ($\hbar\omega' \gg mc^2$), in which the electron loses a large fraction of its energy in a single scattering process. The differential number density of up-scattered photons, resulting from the interaction of mono-energetic electrons of energy γmc^2 with a segment of an isotropic photon gas $\mathrm{d}n(\epsilon) = n(\epsilon)\,\mathrm{d}\epsilon$, expressed as a function of the up-scattered photon energy ϵ_1 in units of the initial electron energy, $E_1 = \epsilon_1/(\gamma mc^2)$, is given by (Blumenthal & Gould 1970):

$$\frac{\mathrm{d}N_{\gamma,\epsilon}}{\mathrm{d}t\,\mathrm{d}E_1} = \frac{2\pi r_0 mc^3}{\gamma}\frac{n(\epsilon)\,\mathrm{d}\epsilon}{\epsilon}\left[2q\ln(q) + (1+2q)(1-q) + 0.5\,\frac{(\Gamma_e q)^2}{1+\Gamma_e q}\,(1-q)\right] . \tag{2.7}$$

r_0 denotes the classical electron radius, $q = E_1/\Gamma_\epsilon(1-E_1)$. The dimensionless parameter $\Gamma_\epsilon = 4\epsilon\gamma/mc^2$ determines the domain of the scattering: The Thomson limit corresponds to $\Gamma_\epsilon \ll 1$, the extreme Klein-Nishina limit to $\Gamma_\epsilon \gg 1$. The transition is also mirrored in a change of the energy loss rate from $\mathrm{d}E/\mathrm{d}t \propto \gamma^2$ for the Thomson regime to $\mathrm{d}E/\mathrm{d}t \propto \ln\gamma$ in the KN regime. Scattering off a black body distribution of photons will result in a broad spectral energy distribution (SED) which peaks in the Thomson regime at

$$E_{\gamma,\mathrm{TeV}} \approx 33 E_{e,\mathrm{TeV}}^2 k_B T_{\mathrm{eV}} , \tag{2.8}$$

where T denotes the temperature of the photon field, E_e the energy of the electrons and k_B is the Boltzmann constant (Hinton & Hofmann 2009).

In the general case, Eq. 2.7 needs to be integrated over the considered electron and photon spectra to calculate the resulting spectrum of the up-scattered photons. For an electron distribution with a power law spectrum $\mathrm{d}N/\mathrm{d}E \propto E^{-\alpha}$, scattering on a black body target photon field, the resulting Inverse Compton spectrum in the Thomson regime is also given by a power law with spectral index $(\alpha+1)/2$. In the KN regime, the spectrum is a power law as well, but much steeper with an index of $(\alpha+1)$. Consequently, the contribution from softer photon fields will dominate with increasing energy in the lepton spectrum.

Synchrotron emission provides an additional probe to a population of highly energetic non-thermal electrons in the ISM, but at lower energies than IC photons. The typical energy of synchrotron photons emitted by mono-energetic electrons is given by

$$E_{\mathrm{S,eV}} \approx 0.087 E_{e,\mathrm{TeV}}^2 B_{\mu\mathrm{G}} . \tag{2.9}$$

Relating this result to Eq. 2.7, one finds that IC and synchrotron photons trace the same parent lepton distribution, provided that $E_\gamma = 380 E_{\mathrm{S}}(k_B T_{\mathrm{eV}}/B_{\mu\mathrm{G}})$. Assuming scattering on the CMB and $B = 100\,(1)\,\mu$G, 11 TeV electrons produce 1 keV (10 eV) synchrotron photons as well as 1 TeV IC photons (cf. Hinton & Hofmann 2009). For a power-law

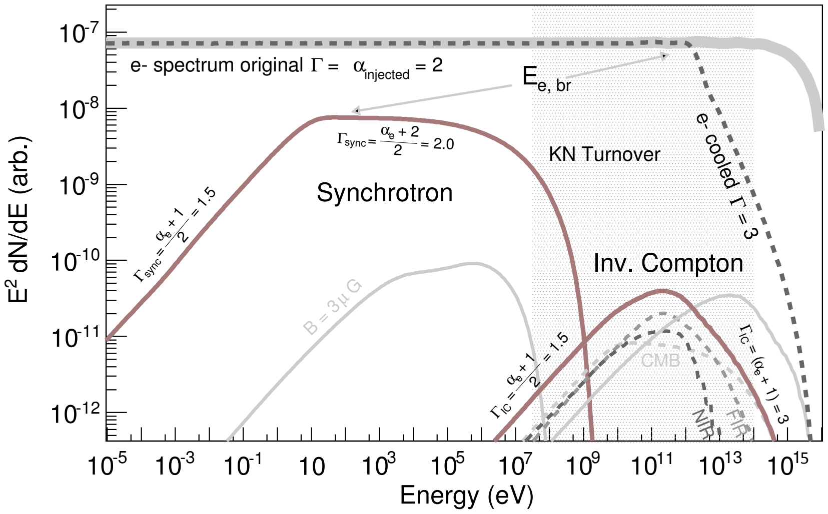

Figure 2.9: IC and synchrotron emission resulting from a non-thermal, cooled electron distribution of age $t = 1000$ years (dark gray). The uncooled, original electron spectrum is shown in light gray (power-law index $\alpha_{\text{injected}} = 2.0$). The assumed magnetic field strength is $100\,\mu$G, whereas the thin gray lines depict the resulting radiation spectra for a lower magnetic field strength of $3\,\mu$G. The gray shaded band marks the region accessible to current γ-ray detectors. A detailed discussion is given in the text. Image credit: Funk (2015).

distribution of the parent electron distribution with spectral index α, the synchrotron spectrum is also given by a power-law with spectral index $(\alpha+1)/2$, as in the IC Thomson regime (cf. Fig 2.9). Hence, the spectra of IC and synchrotron emission show the same basic shape, but at different energies.

The addressed radiation losses lead to a modification of the initial lepton spectrum as soon as the lifetime becomes comparable to the energy-loss time scale, typically referred to as cooling time. For IC scattering, the cooling time can be written as (Hinton & Hofmann 2009)

$$\tau_{\rm IC} \approx 3.1 \times 10^5\, \mathrm{U}^{-1}_{\mathrm{rad,eV\,cm^{-3}}}\, E^{-1}_{e,\mathrm{TeV}}\, f^{-1}_{\mathrm{KN}}\ \mathrm{yr} \tag{2.10}$$

where $f^{\rm KN} \approx (1 + 40 E_{e,\mathrm{TeV}} k_B T_{\mathrm{eV}})^{-1.5}$ is the KN suppression factor, which is in the Thomson regime approximately equal to 1. $U_{\rm rad}$ denotes the radiation field energy density. For 100 TeV electrons scattering on the CMB, the corresponding IC cooling time is 32.2 kyr. The synchrotron cooling time is given by

$$\tau_{\rm S} \approx 1.3 \times 10^7\, B^{-2}_{\mu\mathrm{G}}\, E^{-1}_{e,\mathrm{TeV}}\ \mathrm{yr}\ , \tag{2.11}$$

which gives for a 100 TeV electron in a $3\,\mu$G magnetic field $\tau_{\rm S} = 14.4$ kyr. Hence, depending on the surrounding conditions, one of the cooling mechanism might dominate. The radiative cooling causes a spectral break in the initial particle distribution, in case of a power-law distribution altering the spectral index by $\Delta\alpha = 1$ (steady-state scenario, see Fig. 2.9). In the radiation spectra, an according index shift of 0.5 will become visible.

Electrons also give rise to γ rays via Bremsstrahlung when passing through a medium containing atoms or a plasma, with the loss rate and spectra depending on the properties of the medium. The cooling time for Bremsstrahlung on neutral hydrogen atoms of density n per cm^3 is given by $\tau \approx 4 \times 10^7 n^{-1}$ years. Taking the CMB as targed radiation field, IC scattering dominates at an emission energy of 1 TeV over Bremsstrahlung

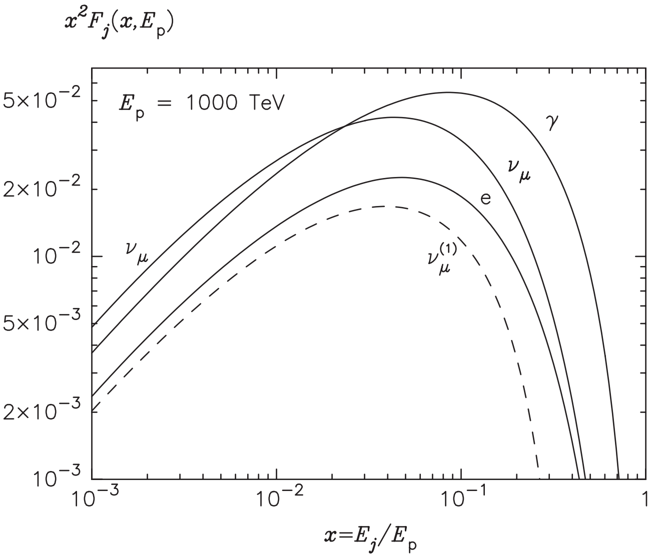

Figure 2.10: Energy spectra of secondary decay products produced in p-p interactions of a mono-energetic proton population of energy 1 PeV. $x = E_j/E_p$ gives the energy of the secondary particle j in terms of the incident proton energy. The spectrum of electronic neutrinos is not shown, as it is nearly identical to that of electrons. Image credit: Kelner et al. (2006).

for $n < 240\,\mathrm{cm}^{-3}$. Electron power-law spectra produce Bremsstrahlung γ-ray power-law spectra with the same spectral index (cf. Hinton & Hofmann 2009).

Hadronic origin of γ rays

In the hadronic production scenario, γ rays are produced by inelastic interactions of highly energetic protons and heavier nuclei with the surrounding interstellar matter. For the given abundance ratios, one typically considers proton-proton (p-p) interactions, in which unstable secondary π-mesons are produced:

$$\mathrm{p} + \mathrm{p} \rightarrow \mathrm{p} + \mathrm{p} + \pi^0 + \pi^\pm + ... \tag{2.12}$$

The higher the energy of the incident particle, the more secondaries get produced, also including a sub-dominant number of heavier hadrons. The decays of the secondary particles give rise to γ rays (π^0-decay), neutrinos, and electrons (positrons) via preceding decay channels:

$$\pi^0 \rightarrow \gamma + \gamma\ , \tag{2.13}$$
$$\pi^\pm \rightarrow \nu_\mu + \mu^\pm \rightarrow \nu_\mu + e^\pm + \nu_e\ . \tag{2.14}$$

By this production mechanism, γ-ray emission traces hadronic CRs and thus their sites of acceleration and interaction. The accompanying produced neutrinos open a window for modern neutrino astronomy, whereas the secondary electrons will give rise to synchrotron radiation which may compete with directly accelerated leptons.

In such a scattering process, typically about half of the energy of the incident particle is carried away by a leading nucleon. The other half splits between charged and neutral pions, indicating that a fraction of about $\kappa = 1/6 \approx 0.17$ of the total primary energy is converted into γ rays (cf. Hinton & Hofmann 2009). Let E_γ denote the photon energy.

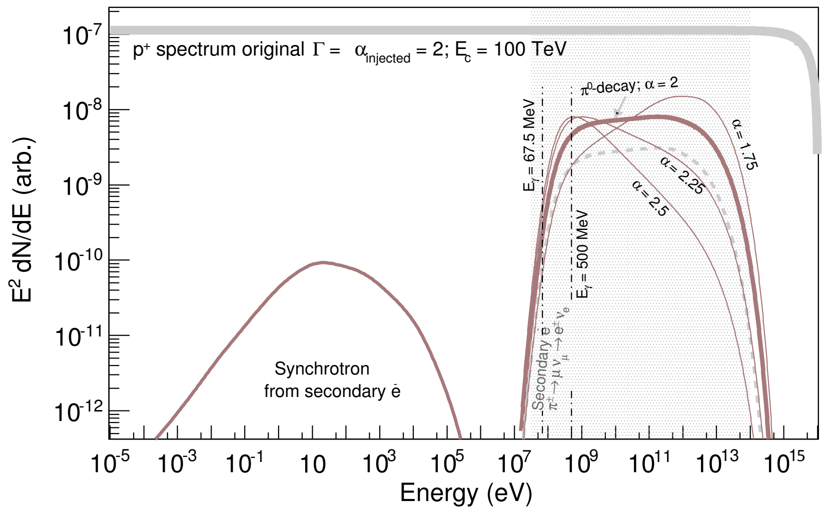

Figure 2.11: Spectral energy distribution of γ rays, resulting from interactions of a power-law proton distribution (power-law index $\alpha_{\text{injected}} = 2.0$, cutoff at 100 TeV) with ambient interstellar matter. The spectral shape of the resulting γ rays (solid red) traces the shape of the parental spectrum quite closely, with the characteristic low-energy cutoff (pion bump) at a few hundreds of MeV. Synchrotron emission from secondary electrons is also shown (assumed source age $t = 1000$ years, magnetic field strength $30\,\mu$G). Thin red lines depict the γ-ray spectra for varying spectral indices of the parent proton spectrum. The gray shaded band marks the region accessible to current γ-ray detectors. Image credit: Funk (2015).

The spectrum of γ rays resulting from p-p interactions of mono-energetic protons of energy E_p, expressed in terms of $x = E_\gamma/E_p$, can be calculated as (Kelner et al. 2006)

$$F_\gamma(x, E_p) = B_\gamma \frac{\mathrm{d}}{\mathrm{d}x}\left[\ln(x)\left(\frac{1 - x^{\beta_\gamma}}{1 + k_\gamma x^{\beta_\gamma}(1 - x^{\beta_\gamma})}\right)^4\right] \tag{2.15}$$

with the parameters

$$B_\gamma = 1.30 + 0.14\,L + 0.011\,L^2\ , \tag{2.16}$$

$$\beta_\gamma = (\,1.79 + 0.11\,L + 0.008\,L^2\,)^{-1}\ , \tag{2.17}$$

$$k_\gamma = (\,0.801 + 0.049\,L + 0.014\,L^2\,)^{-1}\ , \tag{2.18}$$

which depend only on the primary proton energy: $L = \ln(E_p/1\,\text{TeV})$. F_γ implies the number of photons in the energy intervall $(x, x + dx)$ per collision and needs in the general case to be integrated over the proton spectrum. The SED of secondary γ rays, produced by mono-energetic protons, peaks at about 1/10 of the primary proton energy (see Fig. 2.10). For a power-law distribution of the parent proton spectrum, the resulting γ-ray distribution also follows a power law with approximately the same spectral index, cf. Fig. 2.11.

In the rest frame of the π^0 meson, each γ-ray is given half of the pion's rest mass: $E_\gamma = m_{\pi^0}c^2/2 \approx 67.5\,\text{MeV}$. Transforming to the laboratory frame results in a differential number spectrum $\mathrm{d}N/\mathrm{d}E$ which is in a log-log representation symmetric about 67.5 MeV (Stecker 1970). In the usual SED representation, $E^2\mathrm{d}N/\mathrm{d}E$, this symmetry gets destroyed and the characteristic low-energy cutoff at around 400 MeV is created. The exact position of the turnover depends on the spectral shape of the parent proton population (cf. Fig. 2.11, Funk 2015). This so-called pion bump feature is an important spectral characteristic in the high-energy regime in order to unequivocally identify hadronic γ-ray emission.

The cooling time of protons due to inelastic p-p interactions is, assuming a constant cross section of $\sigma_{pp} = 40\,\text{mb}$ and an coefficient of inelasticity of $f \approx 0.5$ (cf. Aharonian 2004), given by:

$$\tau_{pp} = (nc\sigma_{pp}f)^{-1} \approx 5.3 \times 10^7 (n/\text{cm}^{-3})^{-1}\,\text{yr}\ . \tag{2.19}$$

With timescales about an order of 10^7 years, proton cooling plays only a relatively minor role for typical ISM densities of about $n = 1/\text{cm}^{-3}$.

The brightness of a hadronic γ-ray signal is proportional to the density n of the ambient matter. Interactions of local CR populations with dense molecular clouds located in the direct vicinity of a CR accelerator will give rise to bright γ-ray emission. As such, molecular clouds with densities up to several hundred particles per cm^3 provide the generic interaction targets tracing hadronic CRs.

2.2.2 Search strategy

As motivated by the preceding discussion, γ-ray astronomy provides a powerful tool to study current questions of CR astrophysics, and so to search for Galactic PeVatron particle accelerators. The emission characteristics which to search for in γ rays derive from the physical properties of a PeVatron particle accelerator: acceleration of hadronic CRs up to PeV energies and possibly even higher.

This translates to a search for γ-ray sources, exhibiting very hard differential energy spectra, $\text{d}N/\text{d}E \propto E^{-\alpha}$, with spectral index α around 2.0, without indication for strong attenuation in the multi-TeV domain. The power-law spectrum should extend up to several tens of TeV without indication for a cutoff, reaching ~100 TeV, as 100 TeV γ-ray photons are produced by protons of energy of about 1 PeV.
Fig. 2.12 shows proton spectra with a spectral energy distribution following a power-law with exponential cutoff $\text{d}N/\text{d}E \propto E^{-\alpha}\exp(-E/E_{cut})$ for fixed spectral index $\alpha = 2.0$ and different cutoff energies. The corresponding γ-ray spectra resulting from p-p interactions are also shown. It is visible that for cutoff-energies $E_{cut} \gtrsim 1\,\text{PeV}$, the resulting γ-ray spectra show only minor attenuations against a pure power law at the highest energies of the gray shaded band, which depicts the energy range accessible to the H.E.S.S. instrument (CT1-4 observation mode) in the VHE range. A source spectrum which cuts off at around 0.1 PeV would be clearly distinguishable from a potential PeVatron accelerator. Consequently, with dedicated observations and detailed spectral analysis of γ-ray sources with the H.E.S.S. array in the VHE range, it is possible to evaluate the potential PeVatron character of a γ-ray source. Especially the falsification of a PeVatron hypothesis via the detection of a significant cutoff at too small energies in the γ-ray energy spectrum can give a definitive result for such analysis. However, generally spoken, firm conclusions concerning the question of maximum energies in the parent particle spectrum require a modeling of the observed TeV emission starting from this parent particle spectrum and should not be based solely on parameters derived from the γ-ray analysis. To summarize the PeVatron search criteria in VHE γ rays in terms of source properties, they can be formulated as:

- Hard spectral power-law index α: $\alpha \sim 2.0$.
- No early cutoff in γ-ray energy spectrum: $E_{cut,\gamma} \geq 100\,\text{TeV}$.
- The emission must be of hadronic origin.

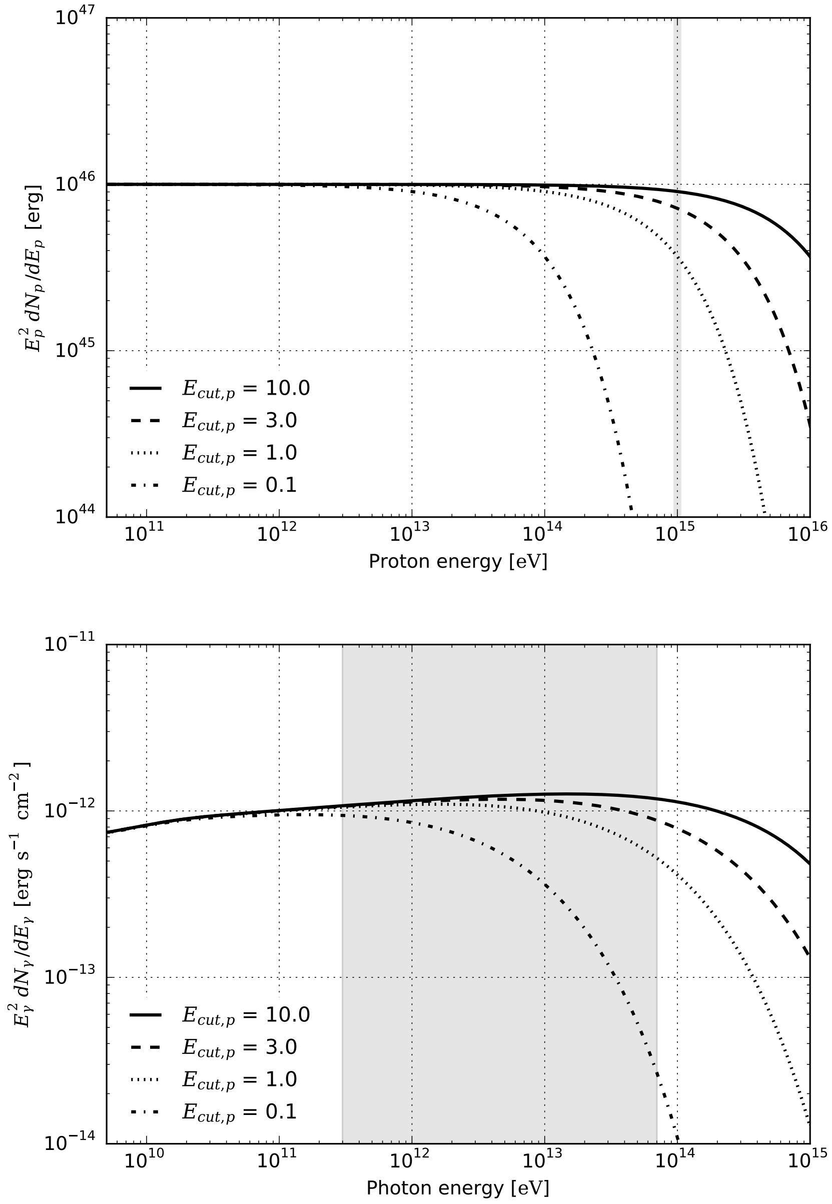

Figure 2.12: Illustration of the spectral signature of a PeVatron particle accelerator. *Top:* Proton spectra following a power law with exponential cutoff for different cutoff energies $E_{cut,p} = 10.0/3.0/1.0/0.1$ PeV and fixed spectral power-law index of 2.0. *Bottom:* Secondary γ-ray spectra resulting from p-p interactions of the corresponding parent proton distribution with ambient matter. The gray shaded band depicts the energy range observable with the H.E.S.S. instrument in CT 1-4 observation mode (exact boundaries depend on observation conditions). For cutoff-energies $E_{cut} \gtrsim 1$ PeV, the attenuation against a pure power law shape is in this energy range rather small, with decreasing impact as the cutoff energy increases. Sources which cutoff at much smaller energies of about 0.1 PeV would be clearly identifiable against potential PeVatrons.

In case of a positive result of an analysis in the VHE range concerning the spectral characteristics, follow-up observations in the high-energy range with Fermi LAT or information from various different wavelengths could help to verify whether or not the emission is indeed of hadronic origin.

In this dissertation, the promising PeVatron candidate source HESS J1826-130 is analyzed using γ-ray data taken with the H.E.S.S. instrument. The detailed study in the VHE band should allow to assess the PeVatron nature of the source as explained above. The spatial location of HESS J1826-130, positioned in direct vicinity of a very bright and strongly extended pulsar wind nebula, constitutes a problematic situation for the standard On-Off region based analysis approach, as the analysis On-region is likely to be contaminated from emission of the neighboring TeV source. For this work, an alternative analysis approach, which is based on a likelihood template-fit, was chosen. The following chapter provides an introduction to VHE γ-ray astronomy with H.E.S.S., including a discussion of the two different addressed analysis approaches.

3 Very-high-energy gamma-ray astronomy with H.E.S.S.

The High Energy Stereoscopic System (H.E.S.S.) is a ground-based γ-ray observatory consisting of five *Imaging Atmospheric Cherenkov Telescopes* (IACTs) located in the Khomas Highlands of Namibia at 1800 m above sea level (Fig. 3.1). In phase I, the H.E.S.S. array consisted of four smaller telescopes, each with a total mirror area of 107 m^2 (CT 1-4). In this initial configuration, H.E.S.S. was fully operational since 2004 and dedicated to VHE γ-ray astronomy between 100 GeV and 100 TeV. In 2012, a much larger fifth telescope (CT 5) with a total mirror area of 614 m^2 was added at the center of the array, launching H.E.S.S. phase II. With CT 5, the energy range of the observatory was extended towards lower energies down to several tens of GeV .

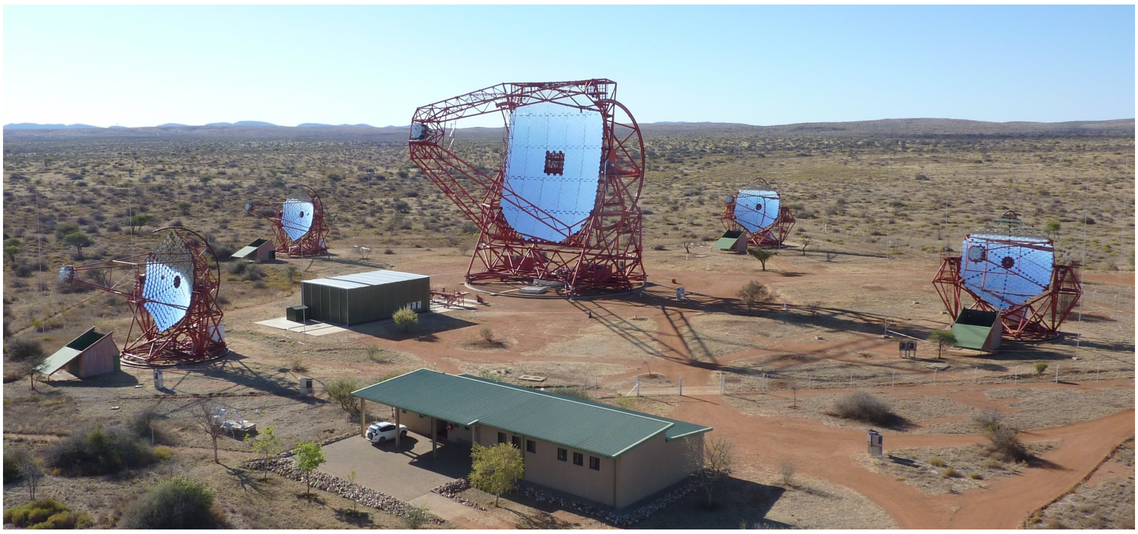

Figure 3.1: The H.E.S.S. γ-ray observatory, in its final phase II configuration consisting of five Imaging Atmospheric Cherenkov Telescopes. Image credit: H.E.S.S. Collaboration.

In the following, the γ-ray measuring technique of IACTs and the analysis chain of H.E.S.S. is described. A special focus will be put on the high-level data analysis, i.e. the analysis procedure starting from the reconstructed data, including source (signal) detection as well as the following morphological and spectral analysis. The discussion of the standard On-Off region approach will be followed by the presentation of an alternative likelihood based template-fit approach, which was applied in this thesis.

3.1 IACT technique

IACTs measure γ rays indirectly by measuring the Cherenkov radiation emitted by secondary particles forming air showers which are initiated by the primary γ rays in the Earth's atmosphere. This detection principle will be described in the following.

Extensive air showers

When a highly energetic particle enters the Earth's atmosphere, a cascade of secondary particles is produced in which the energy of the incident particle gets deposited. Such showers are referred to as extensive air showers (EAS). If the primary is a highly energetic γ-ray photon, an electromagnetic EAS forms: in the Coulomb field of an atmospheric nucleus, the photon gives rise to an electron-positron pair via the pair-creation process. These charged particles will in turn create new photons via Bremsstrahlung. The newly created photons will also undergo pair-creation processes, giving rise to a new charged particle generation in an iteratively developing particle cascade. The number of shower particles grows until their mean energy drops below a critical energy E_{crit} at which they get quickly stopped by ionization losses. The schematic development of such a shower, following the simple Bethe-Heitler model (Bethe & Heitler 1934), is shown in Fig. 3.2. The radiation length X_0 for Bremsstrahlung and pair production are assumed to be equal, doubling the number of particles in the shower within each traversed distance of length X_0.

Air showers produced by hadronic CR particles initiate nucleonic cascades, similar to electromagnetic showers, but including a vast range of nucleonic (strong) interactions. In these interactions, secondary mesons (like pions, kaons) and baryonic particles as well as photons and leptons (muons, electrons, neutrinos), which result from the decays of the unstable secondaries (cf. Fig. 3.2), are produced. Several hadronic and electromagnetic sub-showers might develop besides the main shower branch. Hadronic EAS caused by CRs represent a background signal for γ-ray astronomy which needs to be distinguished from the γ-ray induced air showers. This is reached by separation cuts on the reconstructed shower shape (see chapter 3.2), as electromagnetic air showers develop much more uniformly and with smaller lateral spread than hadronic showers, cf. Fig. 3.3.

Cherenkov light emission

The secondary particles which are created in air showers are highly energetic and move with velocities faster than the speed of light in the ambient medium, the atmosphere. Along their path, the particles polarize the ambient molecules, which will in response emit blueish electromagnetic radiation, so-called Cherenkov radiation (cf. Cerenkov 1937). For particles moving with a velocity v faster than the speed of light in the medium, $v > c/n$ with n the refraction index of the medium, the emitted light interferes constructively, leading to a wave front with a characteristic opening angle

$$\cos\Theta_\mathrm{C} = \frac{c}{n\,v} = \frac{1}{n\,\beta} \tag{3.1}$$

with respect to the direction of movement of the particle (Fig. 3.4). The number of photons emitted per unit path length x per unit wavelength λ of a particle of charge Ze is given

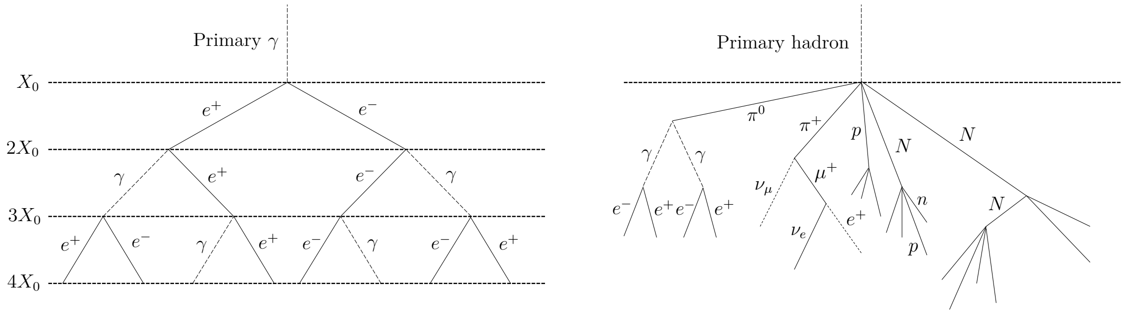

Figure 3.2: *Left*: Schematic illustration of an electromagnetic air shower. The distance between the dotted lines corresponds to one radiation length. *Right*: Schematic illustration of an hadronic air shower. The formation of sub-showers is indicated. Hadronic air showers induce hadronic, electromagnetic and muonic components as well as neutrinos.

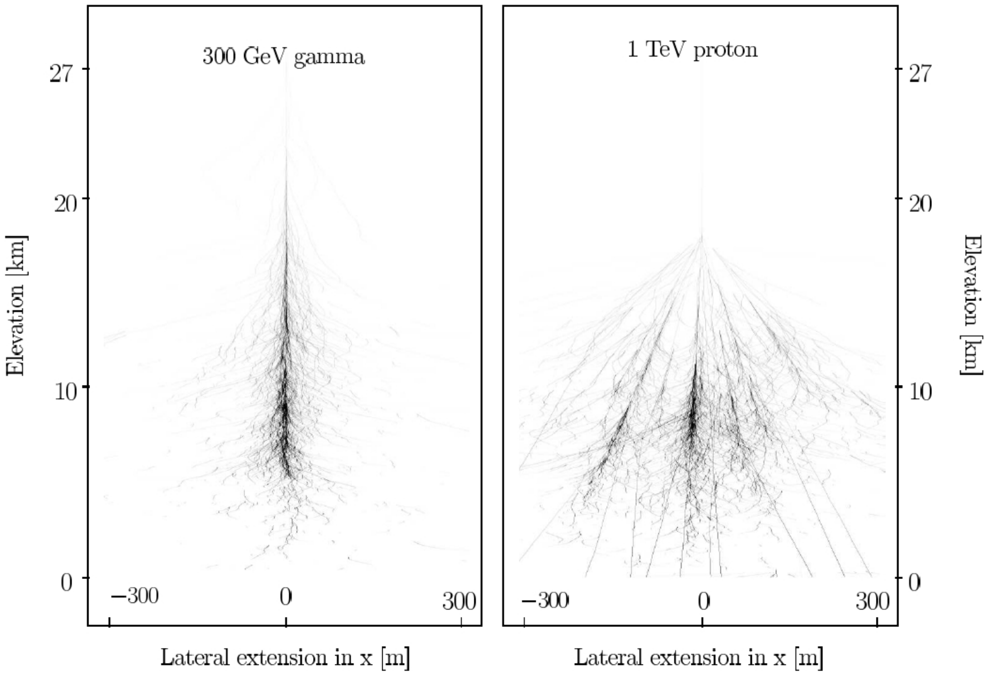

Figure 3.3: Comparison between an electromagnetic (left) and hadronic (right) air shower by Monte Carlo simulation. The hadronic shower develops several sub-showers and exhibits a much larger lateral spread compared to the electromagnetic one, due to strong transverse momentum transfer. Image credit: Berge (2006).

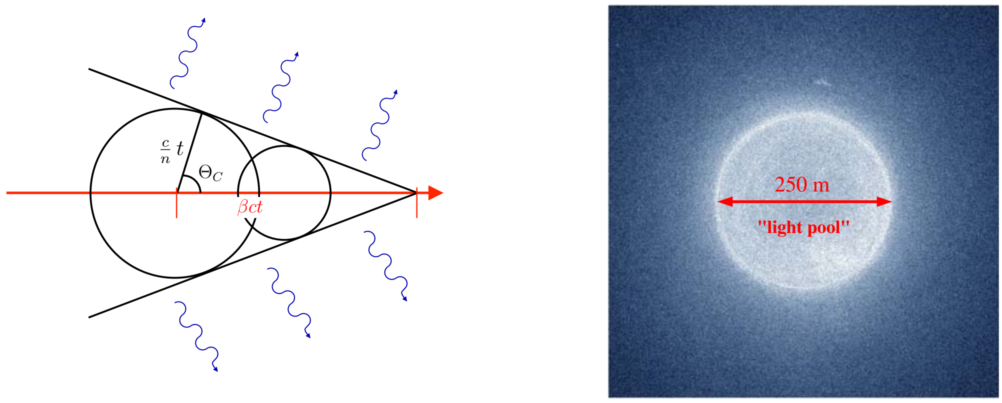

Figure 3.4: *Left:* Cherenkov radiation emitted by a single particle moving faster than the speed of light. *Right:* Cherenkov light pool of an electromagnetic air shower at an observation level of 1800 m, induced by a 1 TeV γ-ray photon. Image credit: Völk & Bernlöhr (2009).

by the Frank-Tamm formula (Frank & Tamm 1937)

$$\frac{\mathrm{d}^2N}{\mathrm{d}x\mathrm{d}\lambda} = \frac{2\pi\alpha Z^2}{\lambda^2}\left(1 - \frac{1}{\beta^2 n^2(\lambda)}\right). \tag{3.2}$$

α denotes the fine structure constant. Given the λ^{-2} dependence, the peak emission is typically reached towards the blue to UV wavelength range. However, below about 300 nm the radiation suffers strong absorption losses in the atmosphere. The maximum number of photons reaching ground level is therefore at about 330 nm (see e.g. Doering et al. 2001). The characteristic opening angle Θ_C is about $0.5°$ at an altitude of 13 km, increasing downwards to about $1°$. The collective emission of Cherenkov radiation from all particles in an air shower results in a rather homogeneously illuminated light pool on the ground, centered on the shower core, with a typical radius of about 125 m for an incident γ-ray photon of primary energy of 1 TeV (cf. Fig. 3.4). The signal time is at the order of a few nano seconds. Near the edge of the light pool most radiation of the shower arrives within $\Delta t \approx 2\,\mathrm{ns}$ (Völk & Bernlöhr 2009). Thus, very short time integration intervals can be used to suppress night sky background signals.

Shower imaging

IACTs measure the emitted Cherenkov light of air showers via large mirror telescopes which focus the radiation on the focal plane of a fast imaging camera. As the air shower is detectable from every location within the illuminated area on the ground, the effective detection area of single IACTs reaches typical values of about $\pi(125\,\mathrm{m})^2 \approx 5 \times 10^4\,\mathrm{m}$. The imaging geometry is illustrated in Fig. 3.5. A typical γ-ray induced shower will generate a characteristic elliptical shower image in the camera, due to the uniform shower development of an electromagnetic EAS. The direction of the incident primary particle can be reconstructed from the geometry of the shower image while the amplitude of the signal correlates to its energy (see chapter 3.2). By observing with more than one telescope, an EAS is simultaneously recorded from different angles. This stereoscopic reconstruction approach allows for a combination of the different shower images for analysis which improves the reconstruction accuracy concerning directional reconstruction, energy reconstruction as well as γ/hadron separation.

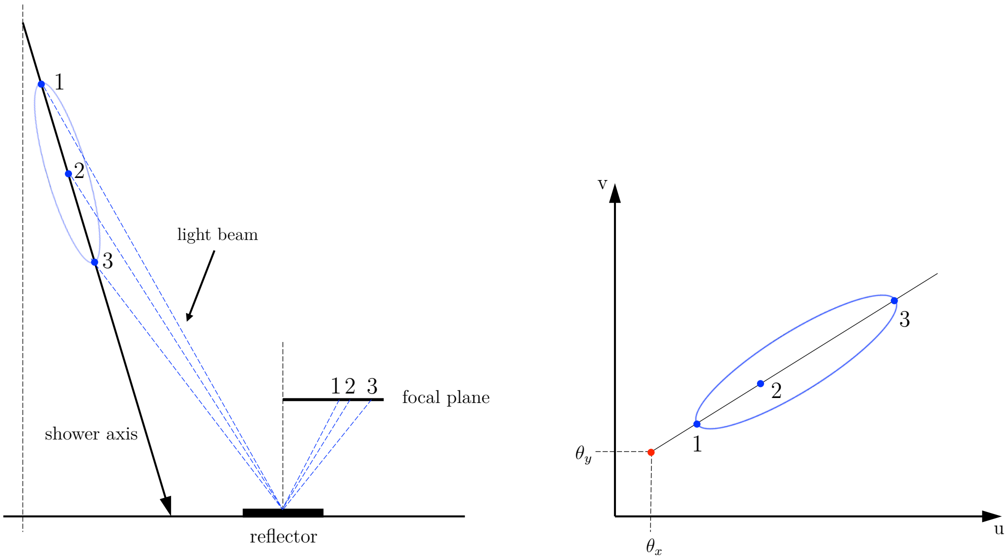

Figure 3.5: Schematic illustration of the air shower imaging of IACTs. The shower is reflected to the focal plane onto a fast imaging camera. The characteristic shower shape of γ-ray induced air showers in the camera focal plane (right) can be approximated by an ellipse.

The H.E.S.S. phase I telescopes

The data analyzed in this work have been taken in CT 1-4 observation mode, the H.E.S.S. phase I configuration. These telescopes are of steel construction and installed in altitude/azimuth mount. Each of them consists of 382 round mirror facets with a diameter of 60 cm (Fig. 3.6), arranged in a hexagonal Davies-Cotton layout (Davies & Cotton 1957) with a flat-to-flat diameter of 13 m. The total effective mirror area thus comprises 107 m^2. The focal length of the system (distance of the mirror dishes to camera) is 15 m. For a detailed description of the optical structure and system, see Bernlöhr et al. (2003); Cornils et al. (2003). Each camera of the four telescopes consists of 960 photomultiplier tubes (PMTs), with each tube corresponding to an area of about 0.16° in diameter on the sky. The total field of view of the camera is about 5° in diameter. Arranged in a hexagonal array, the PMTs are equipped with Winston cones to collect the light which would fall in between them and to minimize the influence of ambient background light. The PMT array is grouped in 60 drawers of 16 tubes each, which contain the electronics for readout and the trigger system and provide the high voltage supply. The trigger system of the telescope array consists of three levels: a single pixel trigger threshold, equivalent to 4 photo electrons reaching the PMT cathode within a time interval of 1.5 ns. The second level is the coincidence requirement within a sector, where one sector comprises a square group of 64 pixels and each camera is subdivided into 38 overlapping sectors (camera trigger). 3 triggered pixels are required within one sector. Third, a coincidence of two telescopes triggering within a time window of 80 ns constitutes the central trigger threshold. Only cameras which triggered individually are read out when the central trigger is hit. Typical observation trigger rates are about 220 Hz. The trigger system and behavior is described in detail in Funk et al. (2004).

Observations with H.E.S.S. are carried out in individual runs with observation times of 28 minutes. Each run is checked for good quality before being used for analysis. This includes checks on the trigger stability of the system (atmospheric influences, sky conditions) as

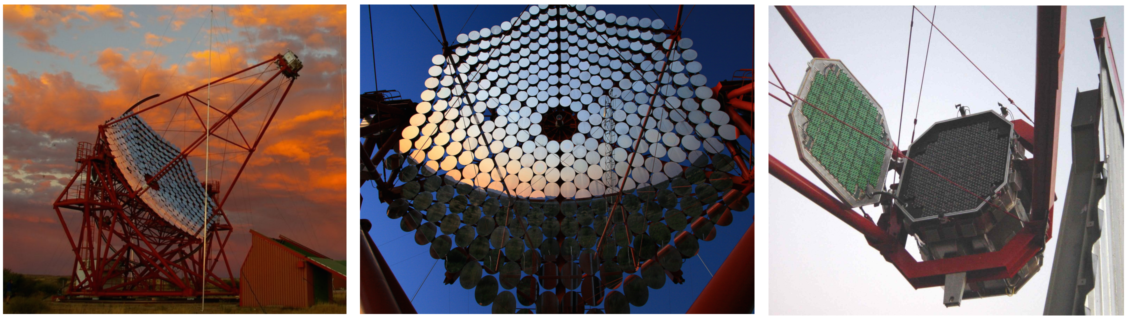

Figure 3.6: Detailed view to one of the H.E.S.S. phase I telescopes. In the middle, a zoom in to the mirror surface comprising 382 mirrors, each of 60 cm diameter, is shown, which focus the light on the camera (right) at a focal distance of 15 m. Image credit: H.E.S.S. Collaboration.

well as on hardware problems. For an overview of the standard data quality selection, see Aharonian et al. (2006a).

3.2 Event reconstruction and γ/hadron separation

The H.E.S.S. low-level analysis, described in detail in Aharonian et al. (2006a), is based on the air shower images of the individual telescopes which recorded the shower.

Image cleaning

The first stage of the reconstruction is the image cleaning, required to only select those pixels which recorded the Cherenkov light against random fluctuations, such as night sky background (NSB) signals. This cleaning applies a threshold based cut on the number of photo electrons (p.e.) which selects only pixels above a number of 5 p.e. and with at least one neighboring pixel above 10 p.e. (also combinations of 4 p.e. and 7 p.e. have shown to work, might however be more sensitive to NSB fluctuations). After this cleaning, an image of a γ-ray air shower can be approximated by a center-filled ellipse, while images of hadronic background events are wider and much more irregular, often showing small isolated sub-showers besides the main shower core, see Fig. 3.7.

Hillas parametrization and γ/hadron separation

Following the cleaning, the images are processed to measure the Hillas parameters based on a statistical momentum analysis of the shower image (Hillas 1985). These parameters include the centroid position of the image, its distance from the camera center as well as its length and width, cf. Fig. 3.8. In addition, the total amplitude of the image (total charge of all pixels after cleaning), the so-called size value, is calculated. This set of parameters is used to characterize the image. Pre-selection cuts based on the shower distance and the size value are applied to ensure good reconstruction quality (excluding truncated images and events of poor statistics).
In the standard approach, the *mean scaled width* method, the reduced width and length values extracted from the Hillas parametrization are used to classify the images as either γ-ray like or hadron like, in order to suppress non γ-ray background signals. A lookup table, constructed from Monte Carlo simulations, is used to predict the mean width and length

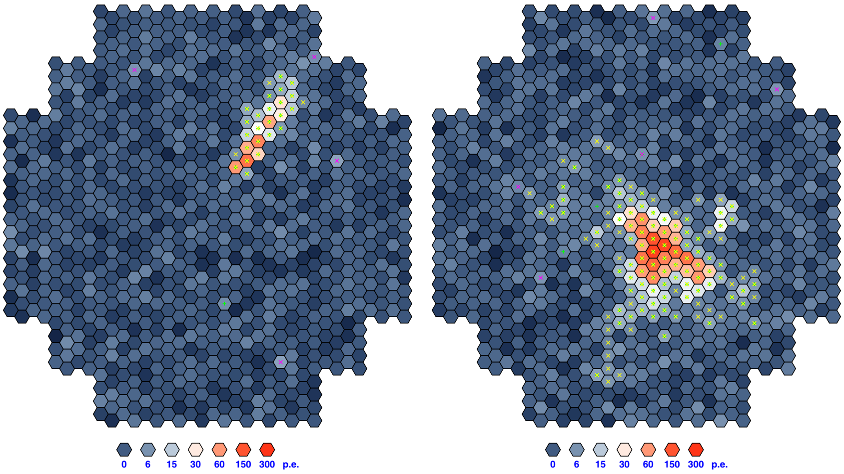

1.0 TeV gamma shower   2.6 TeV proton shower

Figure 3.7: Comparison of camera shower images between a γ-ray induced (left) and CR induced (right) air shower. Hadronic showers exhibit a much more irregular shape compared to the characteristic elliptical structure of γ-ray induced showers. This structural difference provides the opportunity for effective γ/hadron separation (see text for further discussion). Image credit: Völk & Bernlöhr (2009).

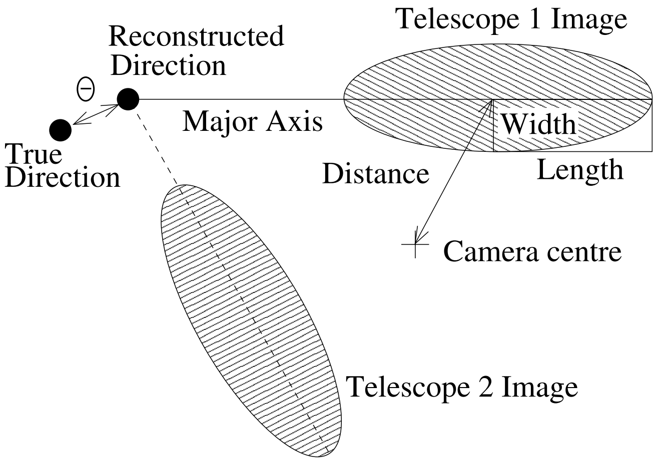

Figure 3.8: Illustration of the Hillas parameters which are used to characterize the shower images. The important parameters for the analysis are distance, width and length and are calculated for each image. The superimposed second image demonstrates the geometrical technique used to reconstruct the source position. θ depicts the angular offset between reconstructed and true shower direction. Image credit: Aharonian et al. (2006a).

for a γ-ray induced shower as a function of total image amplitude and impact parameter (distance of shower impact point on the ground to the telescope). The measured values from the analysis are, for each telescope i, compared to the expected one, and combined to the mean reduced scaled width/length (MRSW, MRSL) values for a measured event:

$$\mathrm{MRSW} = \frac{1}{N_{\mathrm{tel}}} \sum_{i}^{N_{\mathrm{tel}}} \frac{w_i - \langle w \rangle_i}{\sigma_{w,i}} \quad , \quad \mathrm{MRSL} = \frac{1}{N_{\mathrm{tel}}} \sum_{i}^{N_{\mathrm{tel}}} \frac{l_i - \langle l \rangle_i}{\sigma_{l,i}} \ . \tag{3.3}$$

w_i denotes the measured image width, $\langle w \rangle_i$ and $\sigma_{w,i}$ the expected image width and its scatter (analogous, the quantities for the length l_i). A cut on the MRSW value is one of the most discriminating variables which can be used for γ/hadron separation. For an overview of common cut configurations applied in the analysis of H.E.S.S. data, see Aharonian et al. (2006a), Table 2. The total set of cuts applied in the standard analysis (γ/hadron separation cuts including angular θ^2 cut as explained below) retain about 40% of γ-ray events and about 0.024% of CRs (Benbow 2005), resulting in signal to noise ratios of about 1:1 for strong point sources of about 10% of the Crab flux. These numbers illustrate the essential need for an effective separation of the strong hadronic CR background signal for ground-based VHE γ-ray astronomy.

An even improved separation can be reached using modern machine learning algorithms applying multivariate data analysis approaches like boosted decision trees (BDTs), which invoke complex combinations of sets of discrimination parameters. The successful application of BDTs for γ/hadron separation to H.E.S.S. data analysis has been demonstrated by Ohm et al. (2009), improving the sensitivity by about 20% against the classical cut on Hillas parameters. The BDT based separation approach is included in the standard H.E.S.S. analysis chain HAP-TMVA, which has been used for the low-level data analysis in this work.

Directional reconstruction and point spread function

The direction of each event is reconstructed tracing the projected direction of the shower in the field of view, given by the main shower axis of the image, to the point of origin of the particle. For stereoscopic observations, this point is given by the intersection point of the shower main axes from the images of the multiple cameras. This simple geometric method provides directional reconstruction with a typical accuracy of about 0.1°, quantified by the 68% containment radius of the point spread function of the instrument. The point spread function (PSF) is defined as the distribution of the reconstructed angular offsets θ (as defined in Fig. 3.8) of observed events against the true source position for the observation of a point-like source. The PSF is typically considered as a function of θ^2, ensuring a constant solid angle per bin on the sky. Its exact shape depends on the observation conditions: zenith angle, offset angle of the true source position with respect to the camera center (pointing position), optical efficiency of the telescopes, telescope pattern (number of telescopes which observed the shower) and event energy. Lookup tables for the PSF are constructed for various combination sets of these parameters. An example plot showing the PSF for two different zenith angles is given in Fig. 3.9. For the standard analysis, a cut on θ^2 around a considered test position defines the analysis On-region and its exact value is optimized for maximum significance.

In addition to the reconstruction of the sky direction, the impact parameter, defined as the distance of the impact point of the original particle track on the ground relative to the telescope, is calculated. This quantity is of crucial information for the lookup based energy reconstruction scheme, as it directly correlates to the amount of light originally

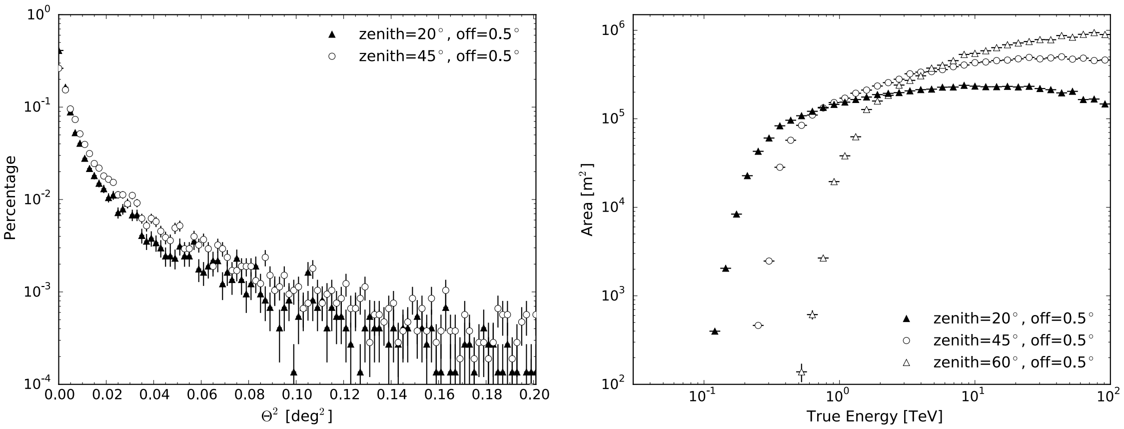

Figure 3.9: *Left:* PSF of the HESS CT1-4 array at an energy of 1 TeV for two different zenith angles and constant offset angle of 0.5°. The 68% containment radius is 0.08° (20° zenith) and 0.11° (45° zenith), illustrating the dependence on the exact observation conditions. *Right:* Effective area of the HESS CT1-4 array for different zenith angles and constant offset angle of 0.5°. Both plots refer to analysis configuration std_zeta, telescope pattern = 30, MC muon phase 101 (see text for further discussion).

emitted by the shower and thus the shower energy.

Energy reconstruction and effective areas

The energy of the primary particle inducing the observed air shower is estimated for each telescope as a function of the image amplitude (size in units of p.e.) and impact parameter, using a lookup table constructed from Monte-Carlo simulations. As the image amplitude is affected by the changing optical efficiency of the telescopes, the energy esimate E_{MC} is corrected by the ratio of the simulated optical efficiency ϵ_{MC} and the measured optical efficiency ϵ_{N} for each telescope N: $E_{\mathrm{N}} = (\epsilon_{\mathrm{MC}}/\epsilon_{\mathrm{N}})E_{\mathrm{MC}}$. The resulting energy measure is calculated as the mean value of the individual telescope estimates: $E_{\mathrm{reco}} = (\sum_N E_{\mathrm{N}})/N$. The energy bias and resolution, depicting the uncertainties in the energy reconstruction, are calculated from the reconstruction error $\Delta E = (E_{\mathrm{reco}} - E_{\mathrm{true}})/E_{\mathrm{true}}$. As for the PSF, the exact values depend on the given observation conditions. The energy bias (mean value of ΔE) defines the safe energy threshold for analysis, requiring a bias smaller than 10% towards the low energy range. Away from threshold effects, the bias is very small (at a level of a few percent, compatible with zero), while typical values for the energy resolution (defined by the width of the distribution of ΔE) are about 15%. Fig. 3.10 shows the energy bias as a function of zenith angle, as well as an example distribution of ΔE.

The effective detection area of the telescope array as a function of energy is needed to convert the number of detected γ-ray photons into physical flux values. It is determined from Monte Carlo simulations: $A_{\mathrm{eff}}(E) = (N_{\mathrm{det}}(E)/N_{\mathrm{MC}}(E))\, A_{\mathrm{MC}}$, the ratio of the number of detected events over the number of simulated events times the area used for the simulation. As the PSF and the energy resolution, it depends on the exact observation conditions. Fig. 3.9 shows typical $A_{\mathrm{eff}}(E)$ curves for different zenith angles.

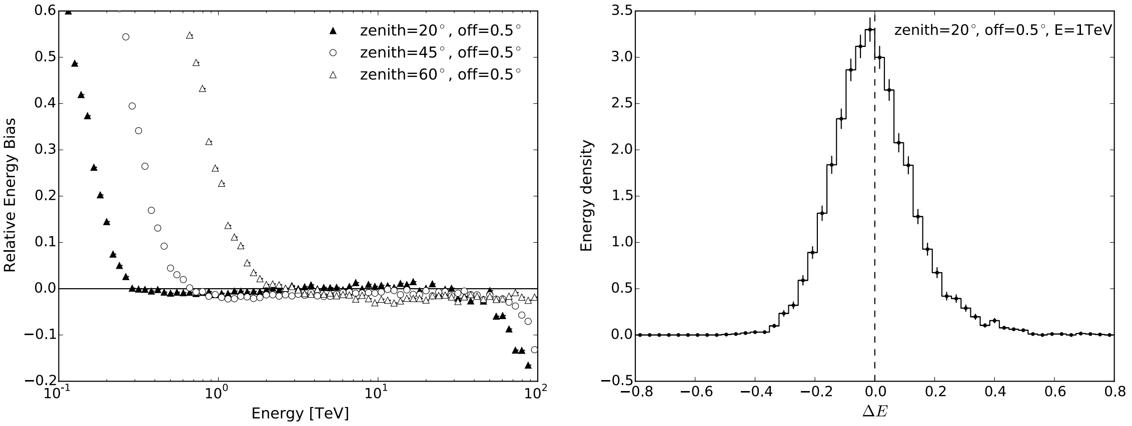

Figure 3.10: *Left:* Relative energy bias of the HESS CT1-4 array for different zenith angles. The safe energy threshold (bias $< 10\%$) rises with increasing zenith angle. *Right:* Example distribution of the energy reconstruction error ΔE for a zenith angle of $20°$, offset angle of $0.5°$ at an energy of 1 TeV. The mean value gives the energy bias, while the width (root mean square) of the distribution gives the energy resolution. For the given parameters, the mean value is -0.4%, the width is 14%. Both plots refer to analysis configuration std_zeta, telescope pattern = 30, MC muon phase 101.

Instrument Response Functions

The Instrument Response Functions (IRFs) give the link between the true physical properties of an observed astrophysical object and the measurement (detector response). The measured quantities $\vec{d}$ of an event are linked to the true quantities of the incident photon. Generally, these properties comprise true/reconstructed event time, event energy and event direction.

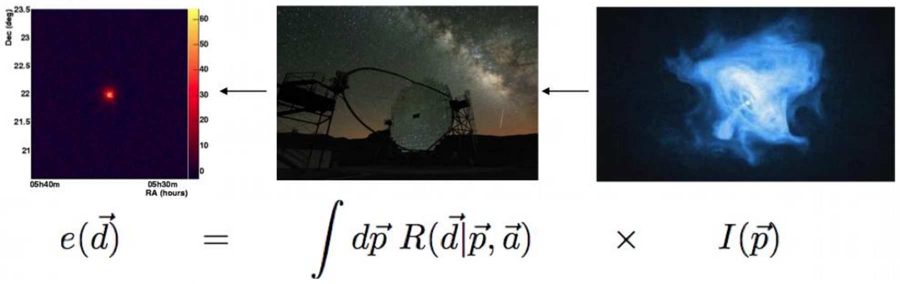

Figure 3.11: Schematic illustration of the instrument response functions. Image credit: `http://cta.irap.omp.eu/ctools/user_manual/getting_started/response.html`.

Let $I(\vec{p})$ denote the γ-ray intensity arriving on Earth, then the expected event rate $e(\vec{d})$ is given by convolving this intensity with the IRFs $R(\vec{d}|\vec{p},\vec{a})$, where $\vec{a}$ takes into account any parameter on which the response function depends. The IRFs can be factorized in the following quantities:

- the PSF, giving the probability density function (PDF) for observing an event at offset angle θ^2 from the true event position.
- the energy dispersion (distribution of ΔE), giving the PDF for reconstructing an event of true energy E_{true} at energy E_{reco}.

- the effective area of the instrument, giving the conversion between physical flux values and number of detected counts.

Additionally, a time dependence might be included. All of these IRFs have been introduced and discussed above. Within the H.E.S.S. analysis chain, lookup tables for the IRFs are produced for various sets of the following parameters: zenith angle of observation, offset angle of true source position with respect to pointing position, telescope pattern and true event energy. The construction of these lookup tables is based on simulation codes such as the air shower generator CORSIKA (Heck et al. 1998), combined with the detector simulation sim_telarray (Bernlöhr 2008). The lookups are reprocessed regularly to take into account the change in the optical efficiency of the telescopes, which minimizes uncertainties (corrections) in the energy reconstruction. This introduces different time intervals for the validity of the lookups, referred to as MC muon phases. During analysis, the lookup tables are queried and interpolated to calculate the IRF value for the exact requested parameter combination.

3.3 Classical On-Off region analysis approach

The classical high-level data analysis in VHE γ-ray astronomy follows a region based analysis approach. Given a test position, defined by the hypothesis of a source being located at this position, an analysis On-region is defined. It is centered on this test position, while its radius is determined by the assumption of an extended or point-like source. For point-like sources, the standard size is $\theta \approx 0.11°$ ($\theta^2 = 0.0125°$), with θ the opening angle (radius) of the On-region. The after separation cuts still remaining γ-like hadronic background is estimated by defining background control Off-regions. Spatial regions of known γ-ray emission or for which emission might be expected are excluded. The number of excess events is given by:

$$N_{\text{excess}} = N_{\text{on}} - \alpha N_{\text{off}} \ , \tag{3.4}$$

where N_{on} and N_{off} refer to the measured number of counts in the On-region and the Off-regions, respectively. The parameter α is a normalization factor which takes into account differences in the On-region and the Off-regions. These concern differences in solid angle coverage, exposure time and detector acceptance for γ-like background events. This acceptance specifies the relative probability of accepting a γ-ray like background event across the FoV and depends on the event energy and the zenith angle of observation. In very good approximation, it can be assumed that it is radially symmetric, i.e. depends only on the distance to the telescope pointing position (for details, see Berge et al. 2007).

Different approaches to construct and locate the Off-regions have been developed, with the ring-background model and the reflected-region background model being of most frequent use. For the ring-background model, a ring around a trial source position (defined in sky coordinates) is used to define the background Off-region, see Fig. 3.12, left. This method is applicable to any point in the FoV and typically used to calculate excess sky maps or significance sky maps. The parameter α is approximately given by the ratio of the solid angle of the ring to the trial source region, $\alpha \approx \Omega_{\text{on}}/\Omega_{\text{off}}$. Additionally, the difference in the acceptance needs to be corrected due to different offsets of the background ring segments and the On-region relative to the pointing position. This is done by an acceptance correction function, applied in the determination of the normalization factor α for each spatial position on the considered regions. Applying the reflected-region method, the On- and Off-regions used for analysis have the same size and are placed with equal offset from the pointing position. Due to the reflection symmetry of the regions with respect to the observation position, no radial acceptance correction is required with this method.

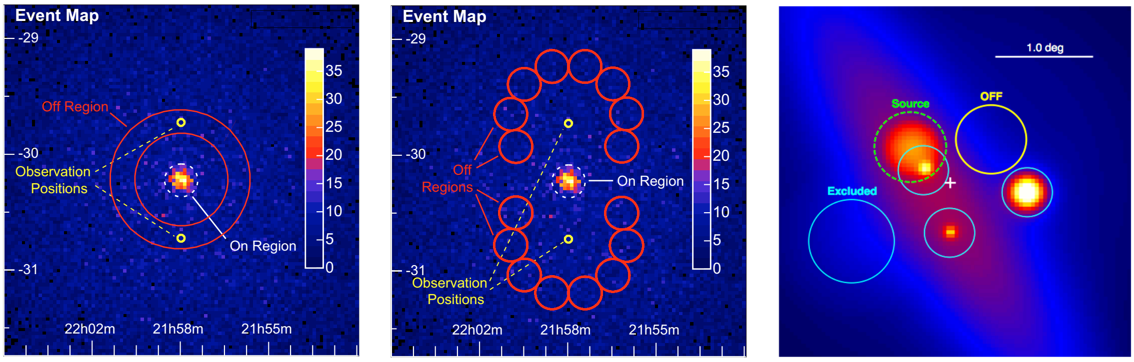

Figure 3.12: *Left/Middle:* Illustration of the ring- and reflected-region background model approach. Shown are count maps of γ-like events from 5 h of H.E.S.S. observations of the active galaxy PKS 2155-304, observed under two wobble offsets in ±0.5° in declination. Image credit: Berge et al. 2007. *Right:* Simulated event map of a complex FoV including several source components spatially overlapping each other. The only possible reflected Off-region for the source of interest (green) is indicated in yellow and is contaminated by remaining emission from neighboring and underlying γ-ray sources. Image credit: Mayer 2014.

The factor α is simply given by $1/n_{\text{off}}$, with n_{off} denoting the number of Off-regions. This method is usually applied for spectral analysis, as it avoids uncertainties related to acceptance corrections. The reflected-region background method was originally developed for the wobble offset observation mode in which tested source positions are observed under a typical angular offset of 0.5° with respect to the pointing position (Aharonian et al. 2001). Wobble observations with different offset positions relative to the trial source position are the standard observation pattern in VHE γ-ray astronomy. The method is illustrated in the middle of Fig. 3.12: two wobble offsets of ±0.5° define the observation pattern, respectively eight reflected Off-regions are defined to estimate the background.

The statistical significance of an extracted signal is derived following the approach presented by Li & Ma 1983, Eq. 17: it is calculated as the square-root of the test statistic $-2\ln\lambda$, where λ is defined by the maximum likelihood ratio of the null hypothesis $\mu_{\text{s}} = 0$ (no extra source exists and all events are due to background) against the alternative hypothesis $\mu_{\text{s}} \neq 0$:

$$S = \sqrt{(-2\ln\lambda)} = \sqrt{2}\left\{N_{\text{on}} \ln\left[\frac{1+\alpha}{\alpha}\frac{N_{\text{on}}}{N_{\text{on}}+N_{\text{off}}}\right] + N_{\text{off}} \ln\left[(1+\alpha)\frac{N_{\text{off}}}{N_{\text{on}}+N_{\text{off}}}\right]\right\}^{1/2} . \tag{3.5}$$

For spectral analysis, the entire considered energy range is subdivided into energy bins. Differential flux values per bin are calculated using the effective area information stored in the lookup tables and the live-time information of the individual runs. A spectral model can be fitted to the reconstructed differential energy spectrum using a forward folding method. Details on spectral reconstruction and modeling can be found in Aharonian et al. (2006a); de Naurois (2012).

Sky maps are generated by introducing a spatial binning on the considered FoV. These maps are filled using the reconstructed directions of the individual events and allow for the construction of raw count maps, excess count maps or significance maps by applying the above outlined scheme pixel-wise. The morphological analysis is based on the excess count map. An assumed model describing the spatial source morphology (e.g. point like or radial symmetric Gaussian model) is fitted to it applying a spatial forward folding which takes into account a mean PSF, averaged in energy. By this procedure, a position and extension estimate of the source morphology is derived. For a more detailed description, see de Naurois (2012).

The outlined On-Off region based analysis scheme constitutes a statistically robust approach for the analysis of isolated point-like sources. It can also be applied to spatially extended sources, though the background estimate gets more complicated as the background control Off-regions need to be located far enough from any region of potential γ-ray emission. In the case of strongly extended sources covering a wide range of the 5° size of the H.E.S.S. FoV, this might not be possible. Concerning the analysis of more complex, crowded FoVs, including several individual γ-ray sources, which might in parts spatially overlap each other, the method clearly reaches its limits: all spatial regions of known γ-ray emission need to be excluded from the background estimate. If this is not the case, the estimated background rate does not represent the true background rate in the On-region. Moreover, if the On-region is contaminated by emission from neighboring sources or is located on top of a faint diffuse large scale component, the On-count estimate will be incorrect. Such a complicated analysis situation is illustrated in Fig. 3.12, right.
The number of detected TeV γ-ray sources increases steadily. With a current count of about 200 firmly established VHE emitters, it has more than doubled during the last decade (see e.g. Degrange & Fontaine 2015), in addition to the detection of a faint, large-scale Galactic diffuse component (Abramowski et al. 2014). In consequence, topics such as source confusion and source region contamination in complex FoVs like the region of HESS J1826-130/HESS J1825-137, considered in this work, have become of increasing importance, demanding for alternative, more advanced analysis methods. Therefore, in the following section, an alternative high-level analysis approach will be introduced.

3.4 ctools template-fit analysis approach

This section presents a high-level analysis approach which is based on a maximum likelihood template-fit: A model holding a spectral and morphological description of the entire FoV is fitted to the measured data and evaluated via the remaining residuals. In the first subsection, the mathematical background and the basic analysis procedure will be outlined. Subsequently, the open and community-driven developed GammaLib/ctools software framework (Knödlseder et al. 2016), which provides the functionality of this analysis approach and was used in this work, is introduced. A brief overview of the open high-level gamma-ray data format (Deil et al. 2017), needed to define common data format specifications for open high-level software frameworks such as Gammalib/ctools, is given. The H.E.S.S. open data format exporters, exporting H.E.S.S. low-level data results to this format specifications and enabling the use of public analysis software tools, will be described briefly.

3.4.1 Maximum likelihood template-fit approach

Maximum likelihood parameter estimation

The maximum likelihood approach is a statistical method for parameter estimation, which allows to fit a model depending on a set of parameters to measured data. Given the PDF of the model, the maximum likelihood estimators are derived by maximizing the likelihood for obtaining the measured data given the parameters. This parameter estimation is usually referred to as maximum likelihood fitting.

The application of likelihood-based data analysis to photon-counting experiments was first described by Cash (1979). In Mattox et al. (1996), a dedicated overview of its application to EGRET γ-ray data is summarized. Also the Fermi-LAT standard analysis framework is based on the maximum likelihood method, see e.g. Abdo et al. (2009b). The overview given here follows Knödlseder et al. (2016).

Let the index i relate to a specific observation. The likelihood function $L_i(M)$ quantifies the probability to obtain the data measured during the observation i given the model M. Its exact formula depends on the applied analysis. In case of unbinned data, the likelihood function is given by

$$-\ln L_i = e_i(M) - \sum_k \ln f_i(\boldsymbol{p}'_k, E'_k, t'_k|M) \ . \tag{3.6}$$

The sum takes into account all events k measured during the observation i. Each event is characterized by a measured direction $\boldsymbol{p}'_k$, measured energy E'_k and measured time t'_k. $f_i(\boldsymbol{p}'_k, E'_k, t'_k|M)/e_i(M)$ denotes the PDF to measure such an event given the model M, while $e_i(M)$ denotes the total number of events predicted to be observed. Per construction of the likelihood function, it is given by

$$e_i(M) = \int\limits_{GTI} \int\limits_{Erange} \int\limits_{ROI} f_i(\boldsymbol{p}', E', t'|M) \ d\boldsymbol{p}'dE'dt' \ . \tag{3.7}$$

The temporal integration is defined by the so-called Good Time Intervals (periods of contiguous data taking), the spatial integration refers to the region of interest (ROI). The energy bounds are given by the considered energy range.
For binned data following a Poisson distribution per bin, the likelihood function is given by summing over all data cube bins:

$$-\ln L_i = \sum_k e_{k,i}(M) - n_{k,i} \ln e_{k,i}(M) \ , \tag{3.8}$$

where $n_{k,i}$ is the number of measured events in bin k and $e_{k,i}$ the predicted number of events. It is given by integrating the PDF over the bin boundaries, or by approximating this integral and evaluating the PDF at the bin center:

$$e_{k,i}(M) = f_i(\boldsymbol{p}'_k, E'_k, t'_k|M) \times \Omega_k \times \Delta E_k \times \Delta T_k \ . \tag{3.9}$$

Accordingly, Ω_k denotes the solid angle of the bin k, ΔE_k its energy width and ΔT_k its exposure time.

Analyzing a set of unbinned observations or combining observations from different instruments, the joint maximum likelihood is calculated, using the following equation:

$$-\ln L = -\sum_i \ln L_i \ . \tag{3.10}$$

In case of combining several observations from the same instrument in a binned analysis, a so-called stacked analysis will be conducted. The same event cube will be filled from all observations. Accordingly, the IRF cubes needed for the analysis are averaged over the invoked observations. For details, see Knödlseder et al. (2016).

The presented maximum likelihood ansatz is a forward folding analysis approach: it uses the IRFs to evaluate a given model in the hyperspace of measured quantities at a certain position in space, energy and time. Besides the intrinsic properties of the considered model component, the IRFs define the PDFs in the respective dimensions. Considering a sky model component $M_j(\boldsymbol{p}, E, T)$ defined as a function of true quantities, the event probability density is calculated by convolving this model with the appropriate IRFs R_i (cf. section 3.2):

$$f_i(\boldsymbol{p}', E', t'|M_j) = \int\limits_{\boldsymbol{p},E,t} R_i(\boldsymbol{p}', E', t'|\boldsymbol{p}, E, t) \times M_j(\boldsymbol{p}, E, t)\, \mathrm{d}\boldsymbol{p}\, \mathrm{d}E\, \mathrm{d}t \ , \tag{3.11}$$

where the model is assumed to factorize in a spatial, spectral, and temporal component:

$$M_j(\boldsymbol{p}, E, t) = M_S(\boldsymbol{p}|E, t) \times M_E(E|t) \times M_T(t) \ . \tag{3.12}$$

This definition allows for energy- and time-dependent spatial models as well as for time-dependent spectral model components and is by this definition implemented in the GammaLib/ctools software framework.

Likelihood ratio tests

The likelihood ratio test (LRT, introduced by Neyman & Pearson 1928) is used for hypothesis testing. Comparing a restricted model M_0 (null hypothesis) describing the data to a more general model M_1 (alternative hypothesis), the test statistic (TS) is defined as the maximized likelihood of the null hypothesis L_0 for the data divided by the maximized likelihood of the alternative hypothesis L_1 for the same data:

$$\mathrm{TS} = -2\, \ln \lambda = -2\, \ln \frac{\max(L_0)}{\max(L_1)} \ . \tag{3.13}$$

For M_0 and M_1 being nested and a sufficiently large sample size, TS will follow a χ^2_n distribution under the null hypothesis with n degress of freedom, where n denotes the number of additional parameters of M_1 compared to M_0 (Wilks 1938). This allows for the calculation of a p-value, given by the probability to observe a TS value larger than the one obtained by the measurement.

FoV template-fit: the data analysis procedure

The likelihood based analysis approach is applied to a given FoV as follows: a template model which holds a spectral and morphological description of the entire FoV is fitted to the measured data, using the maximum likelihood method by optimizing Eq. 3.6/3.8. The resulting best-fit model is compared to the measured data by inspecting the remaining residuals. For an unknown FoV, the start-model will (for analysis in the VHE range) only include a single component describing the γ-like hadronic background. If an excess region of remaining emission is left over in the residuals, a source component holding its individual spectral and morphological model will be added to the FoV template to describe this emission. By this procedure, the FoV model is iteratively improved until no regions of significant excess remain and all sources in the FoV are detected.

The TS value which is obtained by comparing the extended model including a newly introduced source component against the model without it gives a measure of the statistical significance of the source detection. If the component was introduced with one additional free parameter, the flux normalization, the p-value of the source detection is given by (Mattox et al. 1996)

$$p = \int_{\mathrm{TS}}^{\infty} \frac{1}{2}\,\chi_1^2(\zeta)\,\mathrm{d}\zeta = \int_{\mathrm{TS}}^{\infty} \frac{\mathrm{e}^{-\zeta/2}}{2(2\pi\zeta)^{1/2}}\,\mathrm{d}\zeta\ , \tag{3.14}$$

where the factor 1/2 takes into account that only positive fluctuations are tested in the analysis (physical source flux > 0), but both negative and positive fluctuations would contribute equally to TS > 0. Substituting the integrand for $\xi = \zeta^{1/2}$ yields

$$p = \int_{\sqrt{\mathrm{TS}}}^{\infty} \frac{\mathrm{e}^{-\xi^2/2}}{(2\pi)^{1/2}}\mathrm{d}\xi\ , \tag{3.15}$$

which corresponds to the (1-p) quantile of the standard normal distribution. In turn, the significance S of the source detection is simply given by $S = \sqrt{\mathrm{TS}}$.

Unknown sources are typically added with more than one additional free parameter, as their spatial position (and extension) as well as spectral dependency is unknown and to be estimated by the fit. The χ^2 distribution with the corresponding degree of freedom should rather be used to calculate the p-value. From a stringent mathematical point of view, the probability distribution is however generally not exactly known for the considered situation (source over background) due to limited applicability of Wilks' theorem (e.g. the source position degenerates in the null hypothesis, because there is no flux). More appropriately, MC simulations are needed to derive the exact probability distribution of the TS value to allow for a calculation of the p-value. Such simulations have however shown to give results close to 1/2 of the χ^2 distributions with the according degrees of freedom (cf. Mattox et al. 1996, Abdo et al. 2009b, discussing the cases of 1, 2, 3 degrees of freedom).

The described analysis approach represents the standard high-level analysis scheme of the high-energy γ-ray range, at the time dominated by Fermi-LAT. Until now, it is rather uncommon in the VHE range. This situation is however likely to change, as the likelihood based approach provides the strong advantage of simultaneously taking into account all sources which are located in the field of view. This allows for the derivation of a spectral and morphological characterization of the sources in the FoV free of any contamination effects and makes the likelihood based analysis scheme well suited for the analysis of complex multi-source regions as depicted in Fig. 3.12, right.

3.4.2 The GammaLib/ctools software framework

The Gammalib/ctools software package (Knödlseder et al. 2016) is an open source high-level data analysis framework for γ-ray astronomy based on the above outlined likelihood analysis approach. It constitutes one of the promising candidates for the official Science Tools software of the next generation IACT instrument, the CTA observatory (Acharya et al. 2013), currently in the pre-construction phase. The development of the framework is strongly driven by the needs of the CTA project at the moment.

GammaLib[1] is developed with "the ambition to provide a unified framework for the high-level analysis of astronomical γ-ray data". It constitutes a "self-contained, instrument-independent, open source, multi-platform C++ library that implements all code required

---

[1] `http://gammalib.sourceforge.net`

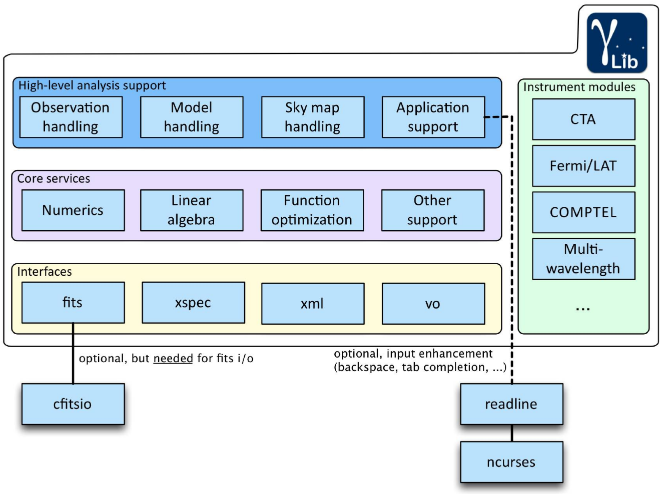

Figure 3.13: Organizational structure of the Gammalib library. Three instrument-independent main layers take care of data handling and analysis core services, while instrument modules support the handling of instrument specific analysis. Image credit: (Knödlseder et al. 2016).

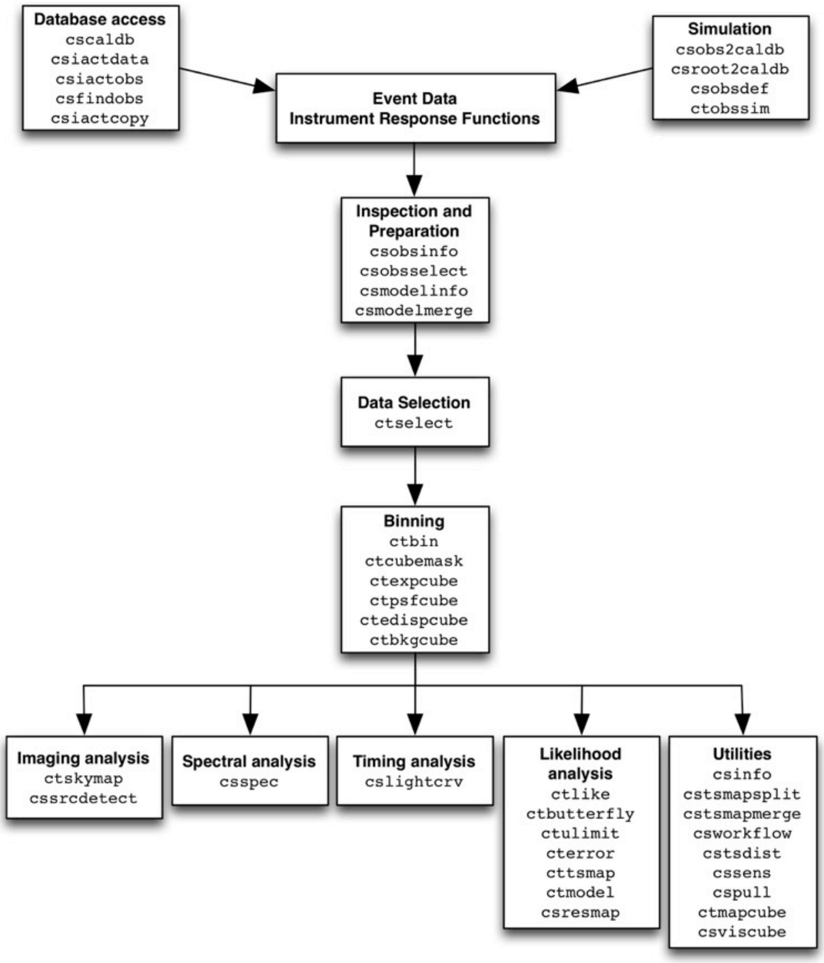

Figure 3.14: Overview of the set of currently available ctools. Each ctool is dedicated to a well defined analysis-step such as data inspection and selection, data binning or performing of the likelihood fit. Image credit: (Knödlseder 2017).

for high-level science analysis of astronomical gamma-ray data" (Knödlseder 2012). It allows for data analysis of current and future γ-ray detectors as well as for combined analysis of data from different experiments. The software layout is organized in three instrument-independent main layers which are subdivided into several modules, see Fig. 3.13. The first layer provides high-level support for the handling of observations, models, and sky maps as well as for the creation of ctool applications. The second layer comprises several analysis core services related to numerical computations and function optimization. The third layer provides the interface to different input/output (I/O) formats. The main data I/O format of GammaLib is based on the Flexible Image Transport System (FITS) data format (Pence et al. 2010), a standard widely used within astronomy. The HEASARC's cfitsio library[2], providing the interface to this data format, constitutes the only required external dependency of the GammaLib/ctools software framework.
The ctools[3] package has been developed building on the functionality of the GammaLib library. It constitutes a set of executable software tools directly applicable to the science analysis of IACT event data. Each ctool performs a well defined analysis step, which allows for a customized workflow matching the specific needs of the analysis. The ctools philosophy and layout, similar to the Fermi Science tools, is based on the ftools (Pence et al. 1993) which are widely used in X-ray astronomy. An overview of the ctools currently available is given in Fig. 3.14. A detailed documentation of each ctool can be found in the online reference manual[4].
Application Programming Interfaces (APIs) to GammaLib and ctools are provided for C++ and for Python using the Simplified Wrapper and Interface Generator (SWIG[5]). This allows, depending on user preferences, for a command-line or script-based in-memory workflow.

The development of the GammaLib/ctools framework is at its current stage in large parts community-driven by feature requests and feedback from the γ-ray astronomy community. The author of this dissertation is co-developer of the GammaLib/ctools framework and contributions to its further development have been achieved within the scope of this work. These comprise contributions to model development, error handling in spectral analysis, significance residual map calculations as well as thorough testing and improving of the CTA module.

3.4.3 Open data formats for gamma-ray astronomy

Currently existing ground-based IACT experiments (e.g. H.E.S.S., Veritas, Magic) are operating independently. Each experiment has defined its individual data structure based on different formats and data can only be read and processed with proprietary software private to the respective collaborations. The development of open source high-level science tools for VHE γ-ray astronomy such as ctools or Gammapy (Donath et al. 2015) however requires common, well-defined high-level data-format specifications to ensure compatibility between different projects. Also CTA will be operated as open observatory and data as well as analysis software will be public.
The gamma-astro-data-formats project[6] (Deil et al. 2017) has been initiated with the aim to develop such common high-level data-format specifications for γ-ray astronomy. It is

---

[2] `http://heasarc.gsfc.nasa.gov/fitsio`
[3] `http://cta.irap.omp.eu/ctools/`
[4] `http://cta.irap.omp.eu/ctools/users/reference_manual/index.html`
[5] `http://www.swig.org`
[6] `https://gamma-astro-data-formats.readthedocs.io/en/latest/`

currently driven by the movement of ground-based IACT experiments towards the usage of newly developed open source science software and can in large parts be seen as a prototyping effort for CTA. The project is an open multi-mission effort, consisting of members from different major γ-ray astronomy experiments currently under operation, not only restricted to the VHE range.
The developed format specifications give a reference for the so-called data level 3 (DL3) which corresponds by CTA specifications to the interface data level between the low-level analysis pipeline and the high-level science tools (Lamanna et al. 2015). DL3 observation data comprise low-level analyzed event-lists (reconstructed events passing γ/hadron separation cuts) together with corresponding IRF tables and housekeeping meta data. Current specifications are based on the FITS data format and have developed out of existing DL3 data format exporters of different operating IACT experiments aiming to provide their data in the requested formats which allow for the usage of software packages like ctools. The H.E.S.S. FITS open data format exporters will be briefly described in the following.

3.4.4 The H.E.S.S. FITS open data format exporters

The H.E.S.S. FITS open data format exporters are needed to convert the output of the standard H.E.S.S. low-level data analysis at the DL3 level to the according open FITS data format specifications as provided by the gamma-astro-data-formats (cf. previous section). This ensures compliance with the data input format required by open source analysis tools, especially the GammaLib/ctools framework or Gammapy.

The development and maintenance of the H.E.S.S. FITS open data format exporters and the production of FITS data set releases is organized within the H.E.S.S. experiment by the HESS FITS data task group. The author of this dissertation is a member of this task group and continuous contributions to this effort have been made within this work. In the following, a basic overview of the FITS data export tools of the H.E.S.S. HAP-HD analysis chain and the resulting data structure is given.

The exporter workflow is organized by the Python wrapper script `hap-data-fits-export` which executes the FITS export within a series of consecutively executed sub-commands. The script takes several options to define basic settings such as the analysis configuration. A detailed description is provided by an internal documentation[7]. The main sub-steps of the FITS export are:

- `hap-data-fits-export --hap-config $CONF --runs-file $RUNLIST events`
- `hap-data-fits-export --hap-config $CONF --runs-file $RUNLIST irfs`

The first sub-command will create the event-list files by running the HAP low-level analysis in mode `hap --FITS/Generate=true`, which will invoke internal exporter conversion routines to FITS data format. The second sub-command will create the FITS IRF files by running `hap-to-irf`, which calls the internal HAP IRF lookup routines for the given run conditions and writes the IRFs out into the specified FITS file format. Other invoked sub-commands take care of data structure and formatting.

Each observation run is exported individually to FITS format and holds its own event-list FITS file and a set of FITS files providing the exported IRF information, e.g. for run `104570` the following file list is created:

---

[7] `https://hess-confluence.desy.de/confluence/display/HESS/HESS+Open+Source+Tools+-+HOWTO+export+HD-HAP+data+and+IRFs+to+FITS`, H.E.S.S. intern

- `hess_events_104570.fits.gz`
- `hess_aeff_2d_104570.fits.gz`
- `hess_edisp_2d_104570.fits.gz`
- `hess_psf_3gauss_104570.fits.gz`
- `hess_psf_table_104570.fits.gz`

The first file is the event-list, which contains the low-level analysis results of each event observed during the run passing the γ/hadron separation cuts. These results comprise event arrival time, reconstructed event-energy and reconstructed event-direction in different coordinate systems. Run meta-data such as date and time of the observation are stored in the header of the FITS event-list file. The second file is the effective area IRF lookup, provided as a function of energy and offset angle. The same for the energy dispersion IRF (third file) and the PSF IRF (files four and five). The PSF is provided in two different formats. The first one uses an analytical description given by the superposition of three 2D Gaussian functions. The second one holds the PSF as a simple histogram (table), directly exported as provided by the HAP lookup scheme without an analytical fit to its functional dependency.

The data access of high-level science tools like GammaLib/ctools is steered by index tables which have to be created during the export step. A master index file holds the information on the different available FITS data sets and provides access to the according observation and data index tables. The exact format and structure is still under development.

The described H.E.S.S. FITS open data format exporters have been used to produce the H.E.S.S. DL3 data analyzed with Gammalib/ctools in this work.

4 Analysis of HESS J1826-130 in VHE gamma rays

This chapter presents a detailed analysis of the unidentified PeVatron candidate source HESS J1826-130 in the VHE energy band. The studied data have been taken with the H.E.S.S. array in CT1-4 observation mode (H.E.S.S. phase I telescopes). The first subsection gives a basic introduction to the studied sky region including a discussion of its multi-wavelength picture. HESS J1826-130 is spatially located in the immediate vicinity of the bright γ-ray emitter HESS J1825-137 and has previously remained unnoticed in the emission tails of this strongly extended PWN. This complex situation points to a contamination of the analysis region of HESS J1826-130 by emission coming from HESS J1825-137 and constitutes a severe problem for the classical On-Off region analysis approach without any standard way to correct for this influence (cf. discussion section 3.3). The analysis results derived using the standard On-Off region analysis approach will be presented and discussed. The main part of this chapter is focused on the alternative ctools analysis approach based on the above presented maximum-likelihood template-fit ansatz. Applying the likelihood template-fit analysis, a spectral and morphological characterization of HESS J1826-130 free of any contamination effects due to emission from neighboring γ-ray sources is reached. The results of both analysis procedures will be compared and discussed. This work presents the first detailed stacked template-fit analysis of a complex FoV using VHE γ-ray data of the H.E.S.S. experiment. Different checks that have been performed to verify this new analysis approach will be presented. The last subsection gives a summary of the most important analysis results.

4.1 Introduction to the field of view

This section provides a basic introduction to the analyzed FoV as seen in the VHE range and summarizes the most recent developments concerning dedicated re-observations and analysis of HESS J1826-130. The currently available H.E.S.S. data sets are described. To give a comprehensive overview, the multi-wavelength (MWL) picture of the region, which has strongly developed within the last decade, will be discussed. This discussion puts the latest results from the VHE range in a more global context, revealing the overall complexity of the considered sky region.

4.1.1 Review on the current status

The VHE γ-ray PWN HESS J1825-137 was discovered with H.E.S.S. in 2005 (Aharonian et al. 2005a). A detailed analysis of the source is presented in Aharonian et al. (2006b), from which the excess count map is shown in Fig. 4.1, left. HESS J1825-137 is strongly extended, showing a clear morphological asymmetry with a somewhat larger tail towards the south-western direction. The extraction region for the overall spectrum

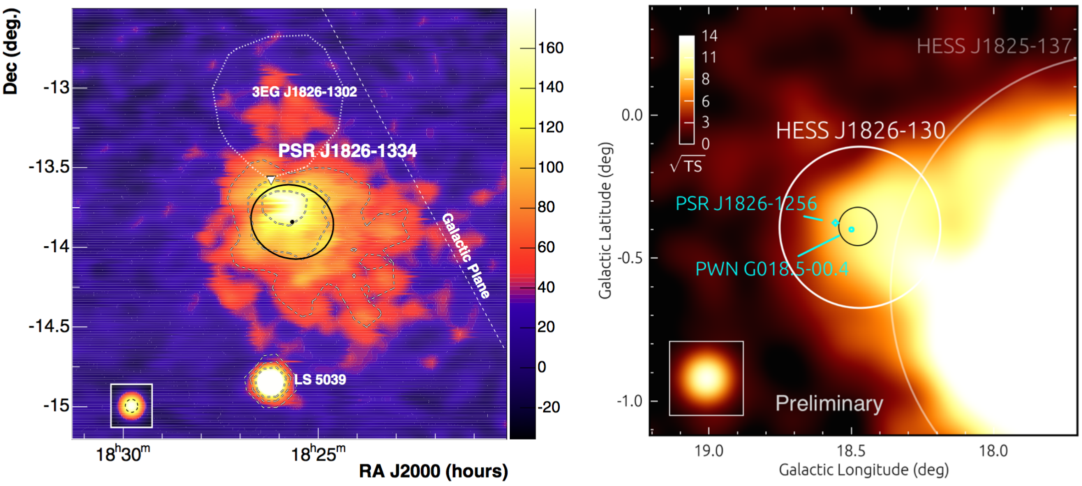

Figure 4.1: *Left:* Smoothed γ-ray excess count map of the HESS J1825-137 region at the status of 2006. The strongly extended, bright central source is the PWN HESS J1825-137. The white contours depict the $5\,\sigma$, $10\,\sigma$ and $15\,\sigma$ significance levels. The bottom left inset depicts the PSF, with the black dotted line showing the applied smoothing radius of $2.5'$. The best-fit position of HESS J1825-137 is marked by a black square, the best extension parameters by a black ellipse. The position of the associated pulsar PSR J1826-1334 is marked by a white triangle. Already in this map, there seems some indication for an additional emission region north to the PWN, located within the emission region of 3EG J1826-1302, indicated by the white dashed line. See text for a detailed discussion. Image credit: Aharonian et al. (2006b). *Right:* Significance ($\sqrt{\mathrm{TS}}$) map of the northern region of the HESS J1825-137 complex at the status of 2015, shown in Galactic coordinates. With improved statistics, the new source HESS J1826-130, depicted by the white line (70% containment radius) has been detected in VHE γ rays. The black circle at the center marks the 68% uncertainty in the best fit position. The inset in the bottom left depicts the PSF. Image credit: Deil et al. (2015).

was defined by an integration radius of 0.8° around the best fit position, which is marked by a black square. The derived spectral index assuming a pure power-law dependency is 2.38 ± 0.02. A detailed spectral analysis at different distances from the PWN center towards the southern emission tail however revealed an energy-dependent morphology, with the spectral index becoming gradually softer from a value of about 1.8 (at a distance of 0.05°) to about 2.4 (at a distance of 1.2°). Interestingly, indication for some additional excess towards the north of HESS J1825-137, at the nowadays firmly established emission region of HESS J1826-130, can already be seen in this excess map. It is located centrally within the 95% positional confidence contour of the EGRET source 3EG J1826-1302 (cf. MWL discussion below), indicated by the white dotted line. However, at that point in time, it was not clear if this feature is related to the strong PWN itself or connected to a new, separate VHE source. In the bottom part of the excess map, the massive radio emitting X-ray binary (XRB) system LS 5039 is visible as a strong point-like source. It was the first XRB system firmly detected to emit VHE γ rays (Aharonian et al. 2005b). Its binary nature in the VHE domain was doubtlessly proven by measuring flux modulations matching the 3.9 days orbital modulation of the system (Aharonian et al. 2006c). LS 5039 is not of importance concerning the analysis of HESS J1826-130, and not further discussed in this work.

With more observation data accumulated over time, re-analysis of the FoV helped to improve the VHE view of the sky region dominated by the luminous HESS J1825-137 complex. A new source, named HESS J1826-130 was announced to be detected within the H.E.S.S. Galactic plane survey in 2015 (HGPS, Deil et al. 2015; H.E.S.S. Collaboration et al. 2018). It is spatially located at the aforementioned northern region of HESS J1825-137, with first parameter estimates of (R.A., Dec.) = $(276.51°, -13.02°)$ and an extension of 0.15° (Deil et al. 2015). The HGPS detection map is shown in Fig. 4.1, right. The overall emission morphology of HESS J1825-137 shows a pronounced edge towards the north-eastern direction. The spatial separation of about 0.7° center to center distance of HESS J1826-130 from HESS J1825-137 together with a clear difference in its spectral emission characteristics is to be taken as direct evidence for a new separate source of VHE emission in the direct vicinity north to the PWN complex. The new VHE source became of special interest due to its extraordinary hard energy spectrum, which made it one of a few candidates proposed to be re-observed within the H.E.S.S. PeVatron campaign, dedicated to the study of potential Galactic PeVatron particle accelerators. In the re-observation proposal for the summer period 2015, HESS J1826-130 was listed with a spectral index of 1.96 ± 0.06, derived assuming a pure power law as spectral model (Aharonian et al. 2014). A likelihood ratio test against a power-law model with exponential cutoff resulted in a statistical significance of 2.0σ, which showed that for the given statistics, no significant evidence ($> 3.0\sigma$) for a cutoff or a strong attenuation up to tens of TeV was found. The depicted situation led to a dedicated re-observation of the source in summer 2015. In this work, these new data have been analyzed with the aim to evaluate the potential PeVatron character of HESS J1826-130 and to provide a detailed spectral and morphological characterization of the source.

4.1.2 Available H.E.S.S. data sets

The data available for the analysis of HESS J1826-130 can be split in two main categories. First, there are archival H.E.S.S. I era data, taken before the installation of CT5 in 2012. The data selection from these H.E.S.S. I data results in a set of 227 runs of spectral quality, corresponding to a total live-time of 97.7 hours (maximum offset angle of target position with respect to observation pointing of 2.0°, minimum number of 3 participating telescopes). These data enabled the detection of HESS J1826-130 within the HGPS. The targets of these observations were LS 5039 and HESS J1825-137, which however leads to large offset angles with respect to the first position estimate of HESS J1826-130. The average offset angle of the data set is 1.60° with a spread of 0.45°.

The second data set consists of those data taken during the dedicated observation campaign on HESS J1826-130 in summer 2015. These data have been taken in CT1-4 observation mode, equal to the H.E.S.S. phase I array. The data selection for the analysis of these data will be discussed in detail below. To reduce systematic uncertainties using the new likelihood template-fit analysis approach, it was decided to restrict the analysis of this work to only this data set. It will be referred to as **data set N** in the following.

Additionally, a standard On-Off region analysis combining the archival H.E.S.S. I era data with the new data set N was carried out by E. O. Angüner and the analysis effort on HESS J1826-130 was split within a dedicated, collaborative task group of the H.E.S.S. collaboration. This combined data set will be referred to as **data set C**. The results of the standard analysis on data set C will be presented alongside the results achieved within this work. They provide a more extensive study on the region within the standard analysis approach, whereas the work carried out in this thesis is focused on the ctools analysis approach. Both analyses developed concurrently and can be seen as mutual cross-check.

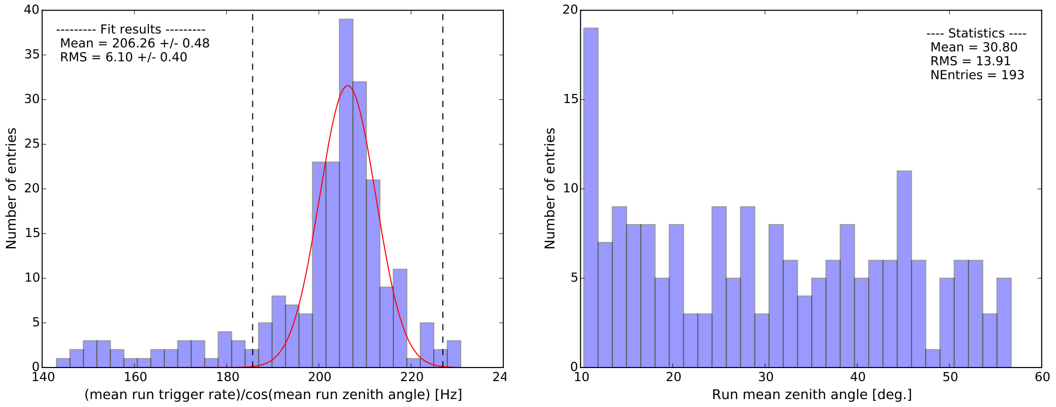

Figure 4.2: *Left:* Illustration of the data selection according to a ±10% deviation from the mean run trigger rate, corrected by the cosine of the mean run zenith angle. The mean of the distribution is determined using a Gaussian fit to the data (red), the dashed black lines indicate the ±10% boundary from the fitted mean value. 193 runs out of 228 lie within this selection boundary. *Right:* Zenith angle distribution of the selected data set. Most runs have been taken under large zenith angles ($> 20^\circ$) to optimize the IRF response in the high energy range. The mean zenith angle of the data set is 30.80°.

Data selection

The data taken on HESS J1826-130 in summer 2015, which have been used for the analysis of this work, data set N, have been selected applying the standard H.E.S.S. hardware data selection cuts described in Hahn et al. 2013. To ensure good data quality for spectral analysis, atmosphere selection cuts checking for stable run-wise trigger rates have been applied (δ_1 and δ_2 cut, see Hahn et al. 2013). This results in a set of 228 runs. Additionally, a cut on the difference of the mean run trigger rate, which has been corrected with the cosine of the mean run zenith angle, is applied to ensure stable long-term atmospheric observation conditions. A cut on ±10% deviation from the mean value of the 228 runs results in a final data set of 193 runs (see Fig. 4.2, left), corresponding to a total live-time of 80.2 hours. Most of these runs have been taken under a large zenith angle ($> 20^\circ$). The zenith angle distribution of the selected runs is shown in Fig. 4.2, right. For the energy range of tens of TeV, which is of special interest for this analysis, this ensures an effective area as large as possible and minimizes uncertainties concerning the energy reconstruction (cf. section 3.2).

At the time of conducting this analysis, no lookup tables for a CT1-4-only observation pattern were available for the optical phase 202 in which the data set N has been taken. Therefore, the IRF lookup tables from the optical phase 101 have been used. This is the phase for which the MC optical efficiency values (the optical efficiency values used for construction of the lookups) match closest to those from phase 202 among all available optical phases. The corresponding nominal values for the two phases are listed in Tab. 4.1 and only show minor differences. The 101 lookups are hence well suited for this analysis. The resulting optical efficiency correction factors (MC optical efficiency over measured optical efficiency) are shown in Fig. 4.3. The values cluster around 1.0, whilst a clear outlier region is visible at run numbers around 50-80. These runs have additionally been checked without showing any conspicuous problematic observation conditions. The muon correction is expected to correct those outliers appropriately and potential threshold effects should not have a major impact given the small fraction of those runs among all analyzed ones ($\sim 16\%$). The complete list of the 193 analyzed runs is given in the appendix.

	CT1	CT2	CT3	CT4
MC eff. phase 101	0.05781	0.05766	0.05734	0.05747
MC eff. phase 202	0.05972	0.05772	0.05439	0.05605
rel. deviation [%]	3.3	0.01	-5.1	-2.5

Table 4.1: Monte Carlo muon efficiency values, used for the creation of the lookup tables for the optical phases 101 and 202. The bottom row shows the relative deviation which is 5.1% at a maximum.

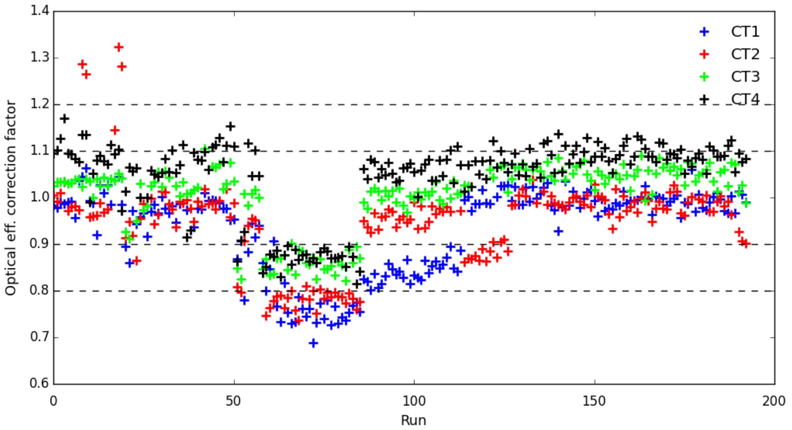

Figure 4.3: Optical efficiency correction factor (muon correction factor) as a function of chronological runlist-number for the 193 runs selected for analysis.

4.1.3 Multi-wavelength picture

First hints for γ-ray emission originating from the north of PSR J1826-1334 (formerly PSR B1823-13) were found by EGRET in the high-energy range with the detection of 3EG J1826-1302 (also called GeV J1825-1310, Hartman et al. 1999), already listed in the first EGRET catalog in 1994 (Fichtel et al. 1994). Its catalog position is (R.A., Dec.) = $(276.55°, -13.04°)$, the radius of the circle which encompasses the same solid angle as the 95% contour is given by 0.46°, cf. Fig. 4.1, left. The pulsar PSR J1826-1334 was detected in the Jodrell Bank 20 cm radio pulsar survey (Clifton et al. 1992). It has a high spin-down power of 2.8×10^{36} erg/s, its exact position being determined to (R.A., Dec.) = $(18^{\mathrm{h}}26^{\mathrm{m}}13.175^{\mathrm{s}}, -13°34'46.8'')$ (Yuan et al. 2010), with a dispersion measured distance of 3.9 ± 0.4 kpc. Consecutive X-ray observations undertaken with ROSAT (Finley et al. 1996), ASCA (Sakurai et al. 2001) and XMM-Newton (Gaensler et al. 2003) showed the presence of a PWN surrounding PSR J1826-1334: a compact emission core of size $30''$ is surrounded by a larger diffuse structure with a size of $\sim 5'$ extending asymmetrically in southern direction. Given the spatial proximity, it was shown early on that an association between PSR J1826-1334 and 3EG J1826-1302 seems plausible by considering the required conversion efficiency in pulsar spin-down power to γ rays for the measured EGRET flux (Zhang & Cheng 1998). Hints for variability in the flux of 3EG J1826-1302 have been detected by Nolan et al. (2003), which led to further association between the PSR J1826-1334 and the EGRET source, finally considered as PWN candidate.

In 2001, ASCA observations in the 2-10 keV energy band of the region of 3EG J1826-1302 however revealed a so far unknown X-ray source, AX J1826.1-1300 (Roberts et al.

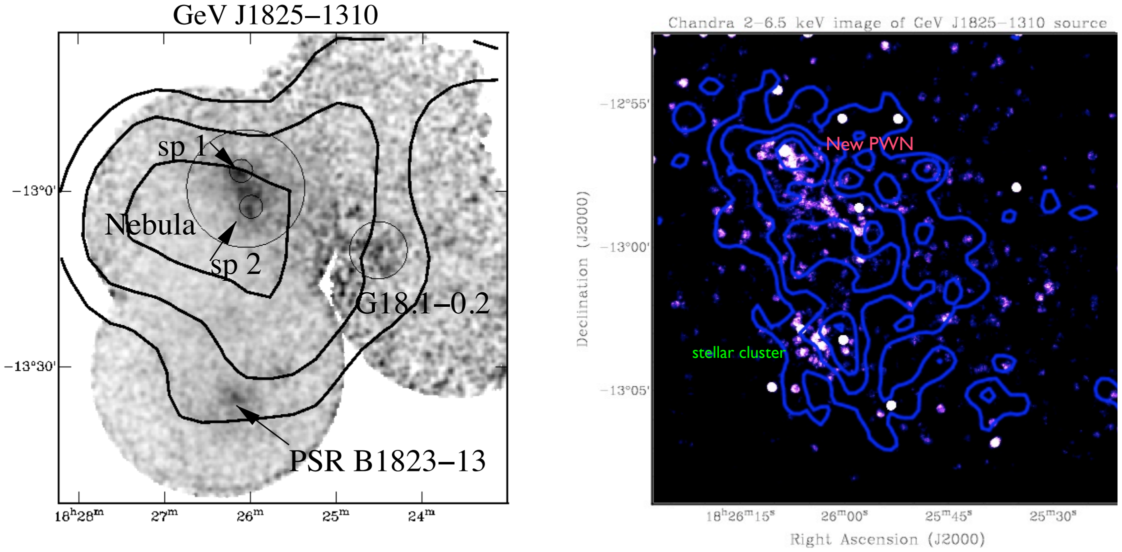

Figure 4.4: *Left:* ASCA X-ray sky map of GeV J1825-1310 = 3EG J1826-1302. The contours give the 86%, 95% and 99% confidence regions of 3EG J1826-1302. The diffuse X-ray source AX J1826.1-1300 is marked as Nebula, containing two distinct emission sub-peaks. The position of PSR J1826-1334 = PSR B1823-13 is indicated. Additionally, the supernova remnant G 18.1-0.2 is located towards the right edge of the FoV. Circles represent spectral extraction regions. Image credit: Roberts et al. (2001). *Right:* Chandra 2-6.5 keV image of the center of 3EG J1826-1302. The blue lines depict the contours of AX J1826.1-1300. Image credit: Roberts (2009).

2001), positioned at (R.A., Dec.) = $(276.5240°, −12.9967°)$. The extended ASCA excess ($> 15'$) is characterized by two sub-peaks, located within a diffuse nebula. The ASCA sky map is shown in Fig. 4.4, left. The new X-ray source is marked as “Nebula”. Additionally, the contours of the 86%, 95% and 99% confidence regions of 3EG J1826-1302 are shown. From this sky map, it is clear that the new X-ray source AX J1826.1-1300 is located much closer to the center of the EGRET source than PSR J1826-1334, which is located outside the 95% confidence level. Hence, from that point on, an association of 3EG J1826-1302 with the new ASCA source seemed more plausible than a connection to PSR J1826-1334. The X-ray picture got resolved in more detail by means of 15 ks exposure of Chandra observations centered on the ASCA nebula (Roberts et al. 2007). The southern sub-peak was found likely to be associated with a stellar cluster, while the northern sub-peak was resolved to host a point-like source connected to a faint, remarkably long ($\sim 4'$) trail of hard (>2 keV) X-ray emission (see Fig. 4.4, right). Due to this long, thin structure, Roberts et al. (2007) referred to this new nebula source as the Eel Nebula. At that point in time, the H.E.S.S. Collaboration had just presented the results of a detailed study of HESS J1825-137, interpreted as the TeV PWN of PSR J1826-1334. Based on their new findings and the fact that some indication for additional TeV excess in northern direction of HESS J1825-137 was already visible in the H.E.S.S. analysis (cf. Fig. 4.1 left, Aharonian et al. 2006b), Roberts et al. (2007) were the first to introduce a new, separate TeV source north to HESS J1825-137, which they named HESS J1826-131 and associated it to the Eel Nebula. A key aspect for the MWL picture, supporting this new scenario, was the following discovery of the radio-quiet γ-ray pulsar PSR J1826-1256 with Fermi LAT(Abdo et al. 2009a). The position of PSR J1826-1256 is consistent with the ASCA source AX J1826.1-1257, sub-peak 1 of the diffuse ASCA nebula (cf. Fig. 4.4, left). In

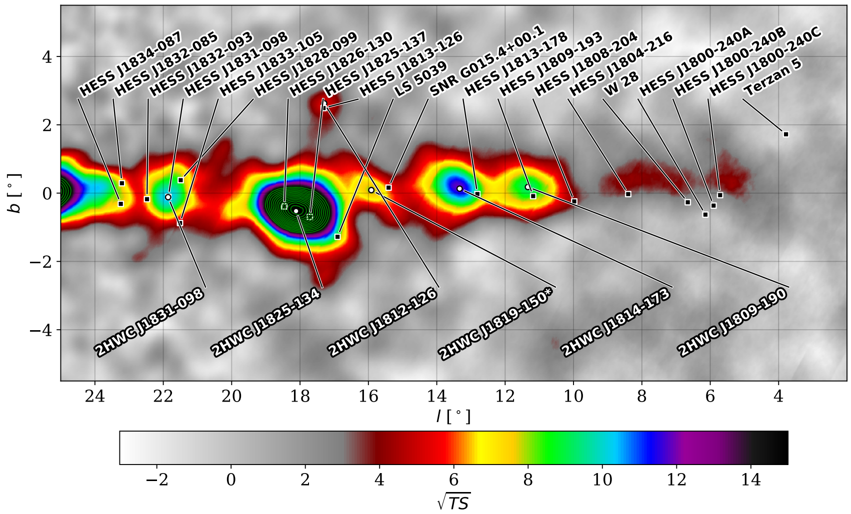

Figure 4.5: Significance ($\sqrt{TS}$) map from the second HAWC catalog, covering the sky region of HESS J1825-137. The source 2HWC 1825-134 overlaps both the source region of HESS J1825-137 and HESS J1826-130, with a distance of about 0.4° to each of them. 2HWC 1825-134 is one of the two brightest sources of the second HAWC catalog. Image credit: Abeysekara et al. (2017).

2011, an improved timing analysis allowed to determine the position of PSR J1826-1256 with an accuracy of about $1''$ to (R.A., Dec.) $= (276.5355°, -12.9425°)$ (Ray et al. 2011), consistent with the position of the Eel Nebula. This timing position is $1.6''$ away from the position of the X-ray point-source as determined from an updated Chandra image (M. Roberts 2010, see Ray et al. 2011). The distance of the PSR J1826-1256 is not known, its high spin-down power of 3.6×10^{36} erg/s and characteristic age of $\tau_c = 14.4$ kyr suggests that it powers the Eel.

The HE counterpart of HESS J1825-137 was detected by the analysis of 20 months of survey data from Fermi LAT (Grondin et al. 2011), whereas no counterpart of the Eel PWN was found in the Fermi data (Ackermann et al. 2011; The Fermi-LAT Collaboration et al. 2017). In 2015, HESS J1826-130 was announced to be detected in VHE γ rays by H.E.S.S. (Deil et al. 2015), spatially located at the emission region of 3EG J1826-1302 and covering the excess region of AX J1826.1-1300. Its first position estimate is located close to PSR J1826-1256 and thus the Eel PWN, see Fig. 4.1. It should be noted that in Fig. 4.1, the position of the Eel Nebula (marked as PWN G018.5-00.4) and PSR J1826-1256 are displayed using catalog positions rather than the improved position estimates derived in Ray et al. (2011), which leads to a larger offset than the above quoted $1.6''$ between the two shown objects.

Additionally, the two supernova remnants G018.1-00.1 and G018.6-00.2, detected in the radio band (Brogan et al. 2006), are located in the emission region, see Fig. 4.6. Also the HAWC instrument detects a bright, extended source at the discussed FoV in the VHE range, named 2HWC 1825-134 (Abeysekara et al. 2017), see Fig. 4.5. However, due to the large spatial extent of the HAWC source covering both the emission regions of HESS J1825-137 and HESS J1826-130, a firm association with one of the two H.E.S.S. sources is currently not possible.

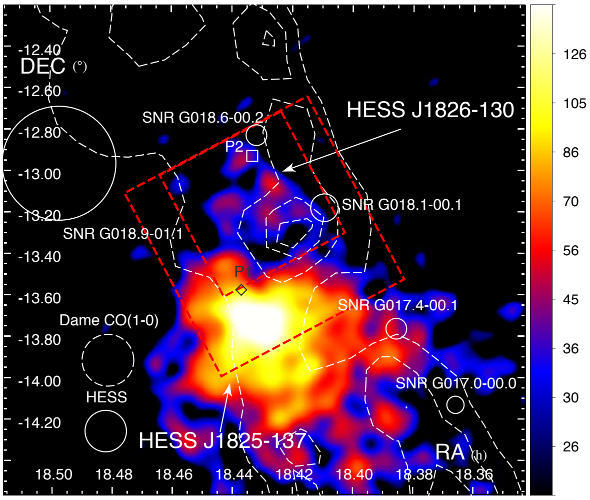

Figure 4.6: H.E.S.S. excess counts image (>100 GeV) towards the region HESS J1825-137, overlaid with the integrated CO(1-0) intensity contour between $v_{\mathrm{LSR}} = 40 - 60\,\mathrm{km/s}$ from Dame et al. (2001), and revealed by Lemiere et al. (2006). The white circles depict different SNRs present in the FoV. P1 indicates PSR J1826-1334, powering HESS J1825-137. P2 shows the position of PSR J1826-1256. The emission region of HESS J1826-130 is indicated. The red dashed boxes give the coverage of the 12 mm and 7 mm Mopra survey coverage. Image credit: Voisin et al. (2016).

ISM gas studies towards the FoV of HESS J1826-130

Detailed ISM gas studies towards the emission region of HESS J1826-130 have been carried out by Voisin et al. (2016), following the discovery of a molecular cloud north to PSR 1826-1334 by Lemiere et al. (2006). The survey region is shown in Fig. 4.6, in which the H.E.S.S. VHE image of the FoV is overlaid with the CO(1-0) contour from Dame et al. (2001). The molecular cloud first revealed by Lemiere et al. (2006) is clearly visible. It has been proposed to explain the asymmetric morphology of HESS J1825-137 by the scenario of a reverse shock forming in the dense medium and crushing back into the PWN, shifting its position towards the southern direction as observed (e.g. Aharonian et al. 2005c).
The molecular gas might be overlapping with the emission region of HESS J1826-130, which was the main motivation for the more detailed study carried out by Voisin et al. (2016), who focus on a possible association between HESS J1825-137 and HESS J1826-130. For their new studies, they used data from a dedicated 7 mm and 12 mm Mopra survey, as well as data from the Nanten CO(1-0) and the GRS ^{13}CO(1-0) surveys.
In agreement with previous results, dense molecular matter was found in the study, with several dense core regions with density values up to $n_{\mathrm{H}_2} \sim 7 \times 10^2\,\mathrm{cm}^{-3}$. Of the observed clouds, one is located at $v_{\mathrm{LSR}} = 45 - 60\,\mathrm{km/s}$, corresponding to a kinematic distance of 4 kpc, similar to the dispersion measured distance of the HESS J1825-137 system of 3.9 kpc. Assuming this cloud to be spherical of radius 18 pc and centered at position (R.A., Dec.) = $(276.47°, -13.26°)$, an averaged density of $n_{\mathrm{H}} = 6.1 \times 10^2\,\mathrm{cm}^{-3}$ and a total mass of $\mathrm{M}_{\mathrm{H}_2} = 3.3 \times 10^5\,\mathrm{M}_{\odot}$ have been derived. The region is depicted by a red circle in Fig. 4.7.

Voisin et al. (2016) conclude that the general spatial match between the observed TeV emission and the detected molecular cloud might suggest a hadronic origin of HESS J1826-130. In this case, the presence of a nearby hadronic accelerator would be required, which might indicate that the progenitor SNR of PSR J1826-1334 leaving behind HESS J1825-

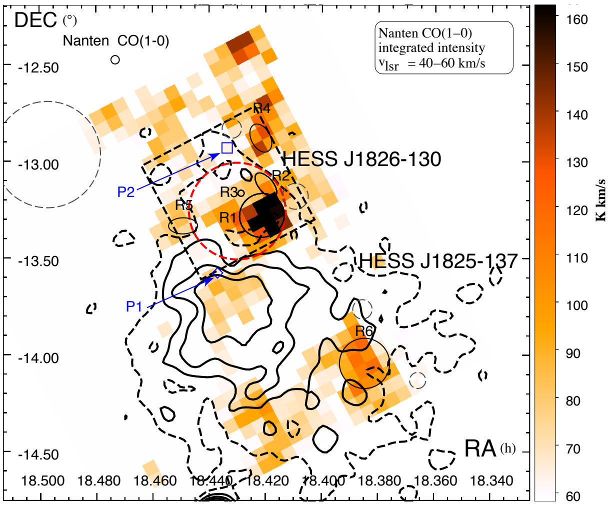

Figure 4.7: Nanten CO(1-0) integrated intensity between $v_{\rm LSR} = 40 - 60\,{\rm km/s}$. The different black ellipses represent dense clump cores identified by Mopra using the NH_3(1-1) and CS(1-0) tracers. The TeV emission measured with H.E.S.S. is overlaid in black contours. The region covered by the Mopra 7 mm survey is shown by the black dashed box. The red dashed circle represents the region whose mass and density has been estimated. Image credit: Voisin et al. (2016).

137 might also be connected to the HESS J1826-130 TeV emission. However, a leptonic emission scenario, in which the TeV emission would be connected to the Eel PWN powered by PSR J1826-1256 could not be excluded.

4.2 Classical On-Off region analysis

In this section, the results from the standard On-Off region analysis on HESS J1826-130 will be presented. This includes a presentation of the results gained from the analysis of the combined data set C (archival HESS I era data and new data from the summer observation campaign 2015, cf. Sec. 4.1.2), as well as the results of a separate analysis of only the new data set N, the identical data set as used for the ctools analysis.

4.2.1 Analysis of the combined data set C

The On-Off analysis of the combined data set C on HESS J1826-130 was carried out by E.O. Angüner in a collaborative effort. Preliminary results have already been published in the conference proceedings Angüner et al. (2017a,b). In the following, a summary of the conducted analysis and the derived results, as presented in these publications, is given.

The analysis is carried out using the HAP-HD TMVA analysis framework. The run list used for detection and morphological studies corresponds to a total live-time of 206 h, without applying any cuts on atmospheric observation conditions (no spectral selection). Hard cuts requiring a minimum of 160 p.e. per image are applied to reach an improved angular resolution to avoid contamination from the nearby source HESS J1825-137 (analysis configuration = `hard_zeta_fullEnclosure`). The ring-background model was used to estimate the remaining level of the cosmic-ray background. The position and extension

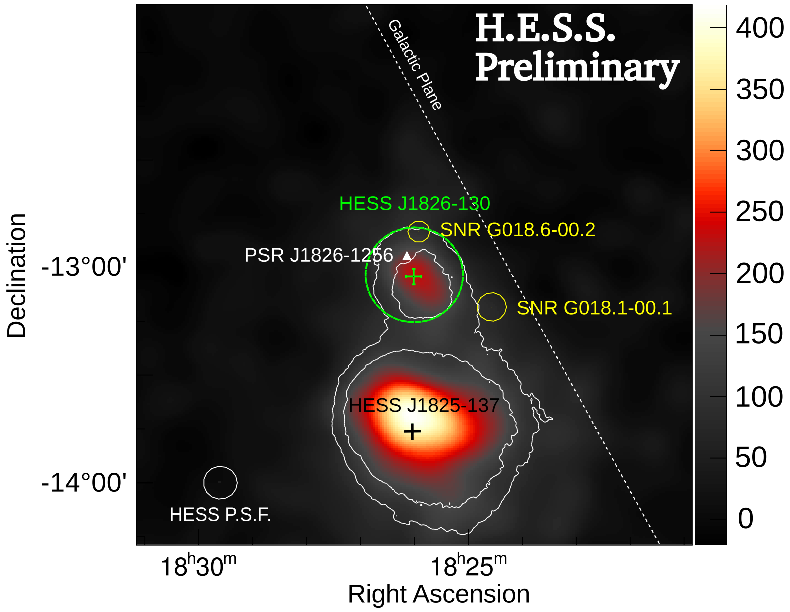

Figure 4.8: Acceptance corrected excess count map (E>2 TeV) of the analysis region for the combined data set C. The map was smoothed with the H.E.S.S. PSF, the color scale is excess counts per smoothing Gaussian width. The white circle in the bottom left shows the 68% containment radius of the PSF. The green cross indicates the best-fit position of HESS J1826-130 and its uncertainty, while the green circle depicts the analysis On-region. The white lines represent the 15σ and 20σ contours. The two SNRs G018.6-00.2 and G018.1-00.1 are marked with yellow circles, the position of PSR J1826-1256 is marked with a white triangle. Image credit: Angüner et al. (2017a).

of HESS J1826-130 was derived fitting a symmetric 2D Gaussian model to the H.E.S.S. excess counts map in the region of the TeV excess of the source. The derived position estimate is R.A. = $276.50° \pm 0.03°$, Dec. = $-13.03° \pm 0.03°$. The fitted extension is $0.17° \pm 0.02°$. The derived best-fit position was used to define the test-position for the analysis. The size (radius) of the analysis On-region was chosen to be 0.22°. By this procedure, HESS J1826-130 is detected with 21.0σ, calculated using Eq. 3.5. Fig. 4.8 shows the acceptance corrected excess count map of the analysis smoothed with the H.E.S.S. PSF for energies above 2 TeV.

Excess count maps for different energy thresholds of $1, 2, 3, 4, 5$ TeV are given in Fig. 4.9. These maps show that HESS J1826-130 becomes more visible with increasing energy threshold due to its very hard energy spectrum and illustrates that the source can easily be hidden by or confused with the bright emission of the nearby neighbor HESS J1825-137.

For spectral analysis, a subset of the detection data set fulfilling spectral selection criteria was used and the background estimate was derived applying the reflected region method. The spectrum is extracted from the analysis On-region of size 0.22°, using the forward-folding technique (e.g. Piron et al. 2001). The spectral reconstruction marks a crucial point in the analysis concerning the question of particle acceleration up to PeV energies. If a cutoff is detected in the γ-ray energy spectrum at energies significantly lower than 100 TeV, the PeVatron hypothesis gets strongly disfavored.
A fit to the measured data assuming a power-law dependency with exponential cutoff $\mathrm{d}N/\mathrm{d}E = \Phi_0(E/1\,\mathrm{TeV})^{-\Gamma}\exp(-\lambda E)$, with $\lambda = 1/E_{cut}$ the inverse cutoff energy, is com-

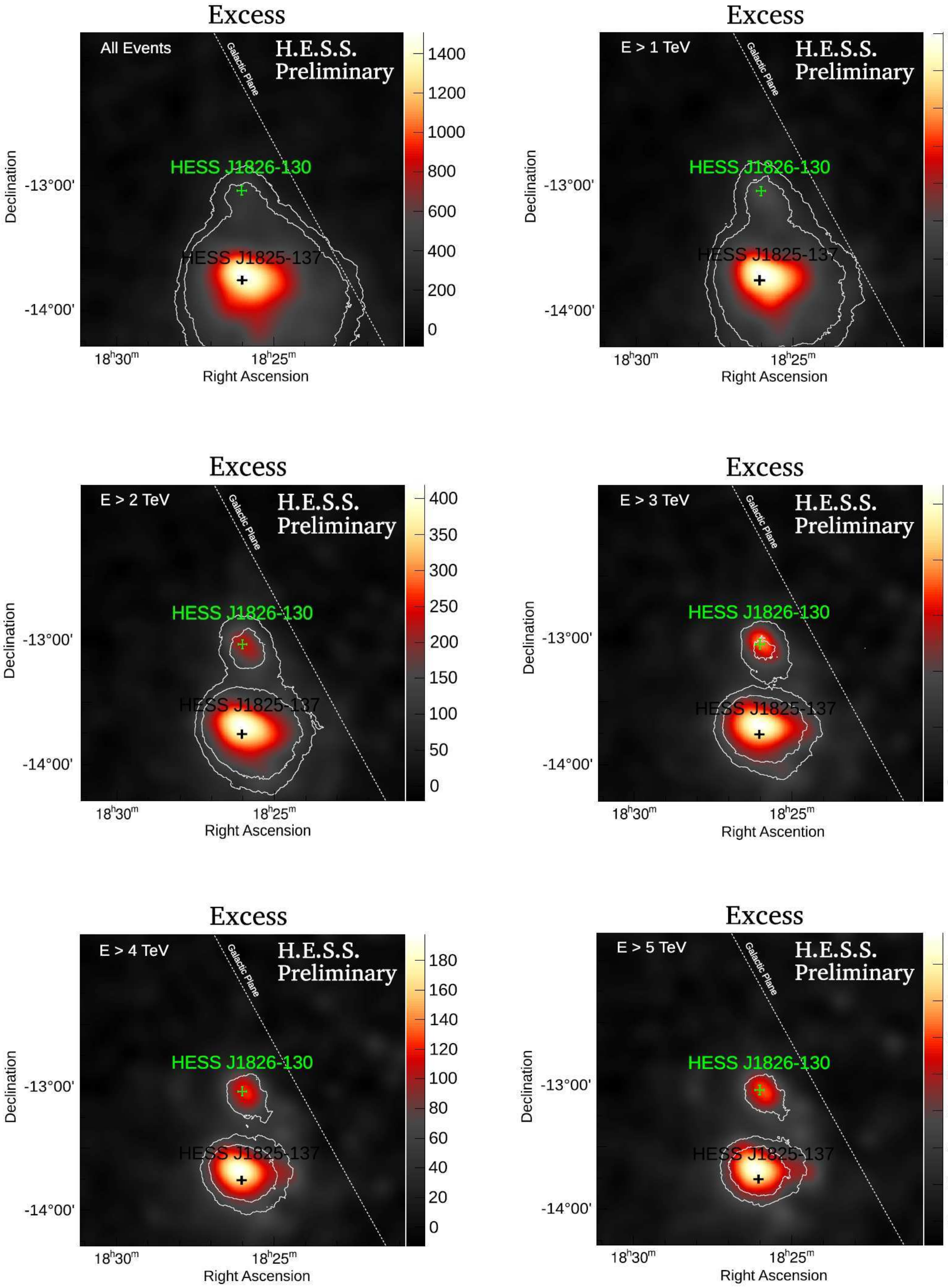

Figure 4.9: Same as Fig. 4.8, but for different energy thresholds, as indicated in the maps. Due to its very hard energy spectrum, HESS J1826-130 becomes more and more visible with increasing energy threshold, clearly separated from HESS J1825-137. Image credit: Angüner et al. (2017a).

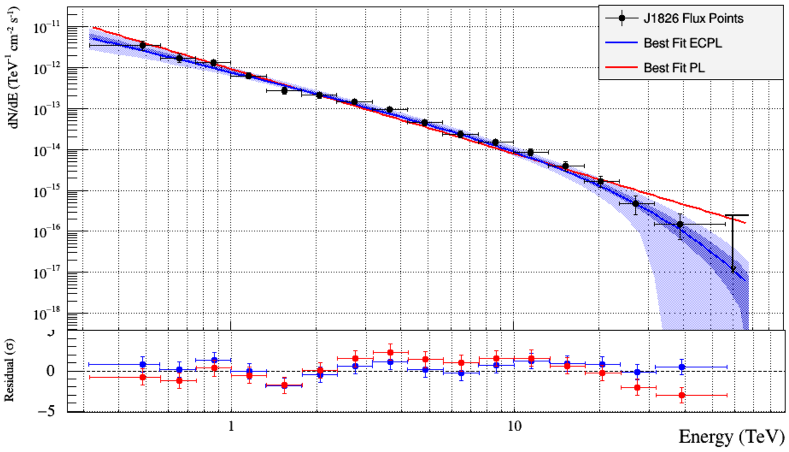

Figure 4.10: VHE γ-ray spectrum of HESS J1826-130, derived from the analysis of data set C within a classical On-Off region analysis approach. The best-fit power-law (PL) and power-law with exponential cutoff (ECPL) models are indicated in color. The blue (light blue) shaded band represents the 68% (99%) confidence interval of the ECPL fit. Image credit: Angüner et al. (2017b).

pared to a pure power-law assumption $\mathrm{d}N/\mathrm{d}E = \Phi_0(E/1\,\mathrm{TeV})^{-\Gamma}$ by means of a likelihood ratio test. The resulting TS value is TS = 12.7, corresponding to 3.6σ (two-sided distributed p-value) preference for the cutoff power-law model. The fit-parameters are summarized in Table 4.2, the fitted cutoff-energy is $E_{cut} = 13.5^{+4.7}_{-2.7}\,\mathrm{TeV}$. Fig. 4.10 shows the derived energy spectrum of HESS J1826-130 including the two best-fit models.

Data set	Fit model	Spectral index	λ	E_{cut}	Φ_0
C	PL	2.07 ± 0.04	-	-	9.37 ± 0.61
C	ECPL	1.66 ± 0.11	0.07 ± 0.02	$13.5^{+4.7}_{-2.7}$	8.92 ± 0.73

Table 4.2: Best-fit model parameters for the spectral assumptions of a pure power law (PL) and power law with exponential cutoff (ECPL). The differential flux normalization at 1 TeV, Φ_0, is given in units of $10^{-13}\,\mathrm{cm}^{-2}\mathrm{s}^{-1}\mathrm{TeV}^{-1}$. λ is the inverse cutoff energy, given in units of TeV^{-1}. The cutoff energy E_{cut}, calculated from this fitted parameter, is given in units of TeV.

4.2.2 Analysis of the new data set N

In addition to the presented results derived from an On-Off region analysis on data set C, an On-Off region analysis of only the new data set N was carried out as part of this work to provide a reference for the ctools analysis with exactly the same data set and the same analysis settings. For this analysis, standard cuts (analysis configuration = `std_zeta_fullEnclosure`) have been used, with the data selected according to spectral selection criteria (see section 4.1.2, data selection). The test position is defined by the best-fit position from the analysis on data set C and the same integration region of size 0.22° was used to define the analysis On-region.

With these analysis settings, HESS J1826-130 is detected with a significance of 11.5σ using the ring-background model. Fig. 4.11 shows the smoothed excess count map. HESS J1826-130 is visible as a northern outlier in the 5σ contour (outer white line) of the emission

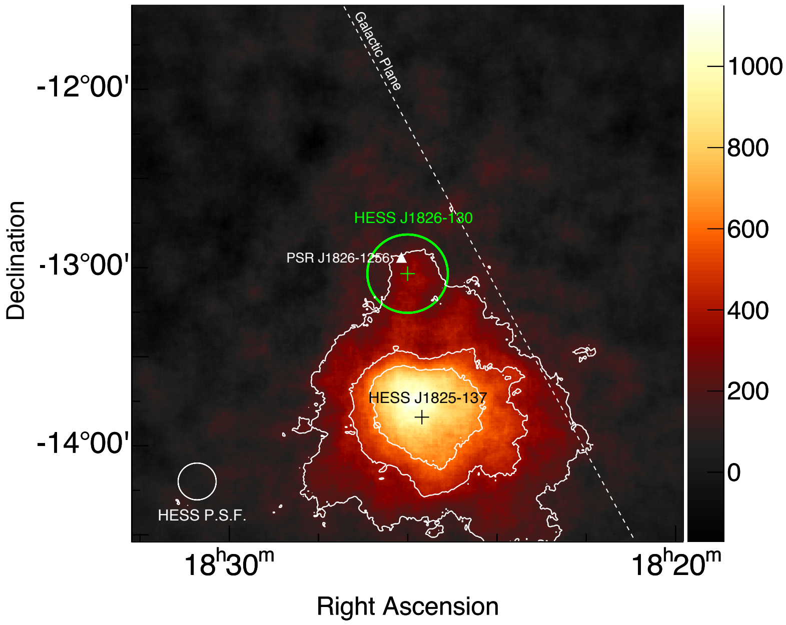

Figure 4.11: Excess count map of the analysis region for the new data set N. The map was smoothed with the H.E.S.S. PSF, the color scale is in units of integrated excess counts per smoothing width. The white circle in the bottom left shows the 68% containment radius of the PSF. The green cross indicates the best-fit position of HESS J1826-130, the green circle depicts the analysis On-region. The white lines represent the 5σ, 10σ and 15σ contours. The position of PSR J1826-1256 is marked with a white triangle.

Data set	Fit model	Spectral index	λ	E_{cut}	Φ_0	$\chi^2/d.o.f.$
N	PL	2.03 ± 0.06	-	-	8.25 ± 0.83	20.6/11
N	ECPL	1.69 ± 0.14	0.05 ± 0.02	$19.6^{+12.9}_{-5.5}$	7.67 ± 0.98	8.4/10

Table 4.3: Best-fit model parameters for the spectral assumption of a pure power law (PL) and a power law with exponential cutoff (ECPL). The differential flux normalization at 1 TeV, Φ_0, is given in units of $10^{-13}\,\mathrm{cm}^{-2}\mathrm{s}^{-1}\mathrm{TeV}^{-1}$. λ is the inverse cutoff energy, given in units of TeV^{-1}. The cutoff energy E_{cut}, calculated from this fitted parameter, is given in units of TeV.

tails of HESS J1825-137.

For spectral analysis, the reflected region background method was applied. The extracted spectrum is shown in Fig. 4.12, together with the best-fit models for a power law and a power law with exponential cutoff dependency. The resulting best-fit parameters are summarized in Tab. 4.3. Their values are compatible with those derived within the analysis of the data set C, cf. Tab. 4.2. The $\chi^2/d.o.f.$ values ($d.o.f. =$ degrees of freedom of the fit) indicate that the power law model with exponential cutoff yields an appropriate description of the data. However, also the hypothesis that the data can be described by the pure power law model cannot be rejected with high statistical significance (p-value = 0.04). Comparing the two models directly by means of a likelihood ratio test results in a TS value of TS = 4.3, corresponding to 2.1σ preference for the power-law model with exponential cutoff.

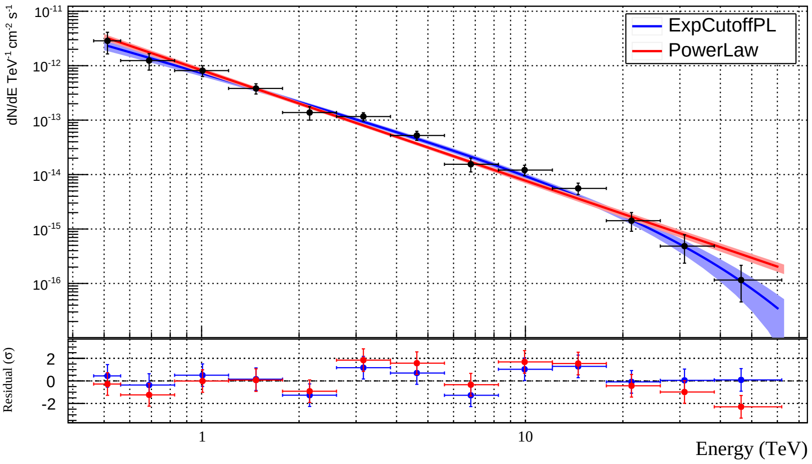

Figure 4.12: VHE γ-ray spectrum of HESS J1826-130, derived from the analysis of data set N within a classical On-Off region analysis approach. The best-fit power-law (red) and power-law with exponential cutoff (blue) models are indicated in color. The shaded bands represent the 68% confidence intervals of the best-fit models.

4.2.3 Discussion

The presented results give a morphological and spectral characterization of HESS J1826-130. The spectral results from the analysis of data set C and data set N are compatible within errors. For the spectral analysis of data set N, the power law model with exponential cutoff is preferred by 2.1σ when being compared to a pure power law model by means of a likelihood ratio test. This result does not give significant evidence for a cutoff in the energy spectrum at tens of TeV, similar to the analysis situation before the new data have been available. For the spectral analysis of data set C, the amount of data is approximately doubled and the same comparison results in a considerably higher value of 3.6σ preference for the power law model with cutoff. This result indicates that there is a cutoff in the energy spectrum of HESS J1826-130, with a cutoff energy of $13.5^{+4.7}_{-2.7}$ TeV. For a hadronic emission scenario, this cutoff energy value is to be seen as clear indication against the PeVatron hypothesis.

The results derived with the On-Off region analysis approach however face a critical problem, which has caused long-standing discussions about the analysis. There might be a non-negligible influence in the analysis due to remaining emission of the neighboring source HESS J825-137 contaminating the analysis On-region of HESS J1826-130. This effect would also influence the spectral reconstruction. A potential contamination effect is likely to be energy-dependent, as seen from the energy-dependent excess maps. It is expected to reduce with increasing energy, due to the fact that the energy spectrum of HESS J1826-130 is much harder than the spectrum in the outer emission regions of HESS J1825-137. In turn, this would indicate that the intrinsic, uncontaminated energy spectrum of HESS J1826-130 might even be harder than derived in this analysis. The question whether or not there is a cutoff in the energy spectrum is, however, expected to not be affected by a potential contamination which increases towards lower energies.

To derive a quantitative estimate of this contamination effect, test regions of same size and same distance as the analysis On-region of HESS J1826-130, placed next to HESS J1825-

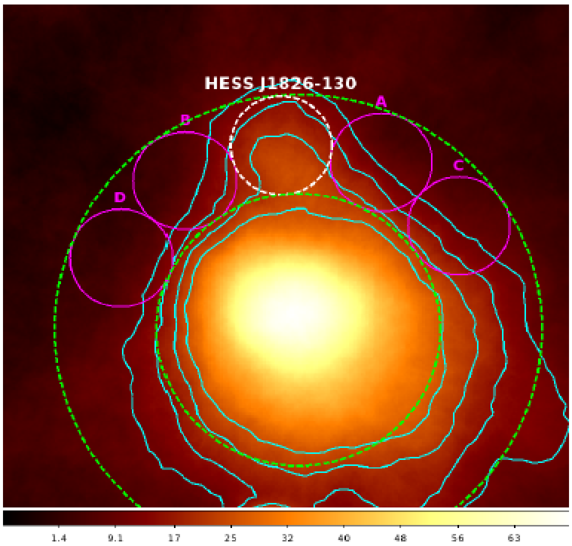

Figure 4.13: FoV significance map of the analysis region. The cyan contours depict the 10σ, 15σ and 20σ levels. The green circles are centered on the best fit position of HESS J1825-137, while the white circle gives the analysis On-region of HESS J1826-130. The test regions used to estimate the contamination from HESS J1825-137 on the HESS J1826-130 region are shown in magenta. Image credit: E.O. Angüner, private communication.

137 were analyzed and taken as reference. These regions are labeled A, B, C, D in Fig. 4.13, showing a FoV significance map for the analysis of data set C. For each region, a standard On-Off analysis was carried out, yielding significant detections ($> 5\sigma$) of γ-ray emission from regions A, B and C. These three regions have consequently been used to estimate the contamination in different energy bins by using the definition

$$\text{contamination (\%)} = \frac{F_{\gamma,\Delta E}\,(\text{test region})}{F_{\gamma,\Delta E}\,(\text{J1826})} \times 100\,, \tag{4.1}$$

the ratio of the integral energy fluxes over the considered energy bin of the test-region to the HESS J1826-130 On-region. The results seem to indicate what is expected: a high contamination at lower energies around 1 TeV, which is at a level of about 45%, decreasing with increasing energy. The contamination estimates are summarized in Tab. 4.4. However, a severe problem in this estimation is the fact that the test regions are located close to HESS J1826-130 itself, which might lead to a significant overestimation of the contamination caused by self-contamination of the test-regions by HESS J1826-130. Due to the asymmetric morphological structure of HESS J1825-137, the test-regions however need to be located as close as possible to the analysis On-region and not in the south-western direction, in which the emission of HESS J1825-137 shows stronger offshoots than in the northern direction.

The complicated situation gives rise to the conclusion that uncertainties are remaining in the spectral characterization of HESS J1826-130 due to contamination effects. The overall agreement is therefore to refer to the energy spectrum derived within the classical On-Off region analysis as contaminated spectrum, which might differ from the intrinsic one. The following presentation of the likelihood based analysis approach circumvents this problem by taking the emission of HESS J1825-137 inherently into account and provides the opportunity to derive the intrinsic spectrum of HESS J1826-130.

Interval [TeV]	[1 – 2]	[2 – 3]	[3 – 4]	[4 – 5]	[5 – 6]	[6 – 7]
Region A	46.7	34.0	28.5	25.4	23.7	22.6
Region B	44.4	33.6	28.8	26.2	24.8	23.9
Region C	44.3	28.7	22.2	18.8	16.7	15.3

Table 4.4: Contamination estimate (percentage) of the analysis On-region of HESS J1826-130, estimated using the test regions A, B, C shown in Fig. 4.13. The values are calculated according to Eq. 4.1. Credit: E.O. Angüner, private communication.

4.3 ctools analysis

In this section, the ctools analysis of HESS J1826-130, based on the presented likelihood template-fit approach (see Sec. 3.4.1), is presented. At the beginning, an overview of the analysis configuration is given, followed by a description of the background template model. This model is used to describe the hadronic background which remains after γ/hadron separation cuts. The analysis procedure is described in detail and the derived spectral and morphological results of the analysis are presented.

4.3.1 Analysis configuration

The likelihood based template-fit analysis is carried out using the data set N, which is described in Sec. 4.1.2. The H.E.S.S. FITS open data format exporters have been used to process the data to DL3 level (cf. Sec. 3.4.4). The low-level analysis was conducted with the HAP-HD TMVA chain, using standard cuts (analysis configuration = `std_zeta_fullEnclosure`).

The ctools analysis is conducted in binned (stacked) mode. The FoV is centered on the position (R.A., Dec.) = (276.50°, −13.50°), with a size of 2° × 2°. This choice relates to the central position in between HESS J1826-130 and HESS J1825-137. The binning is done with the following specifications:

- spatial binning: 0.02° × 0.02° bin-size, resulting in 100 × 100 bins.
- spectral binning: 10 bins/decade, evenly spaced on a logarithmic scale in the interval $\log_{10,\mathrm{TeV}} = [-0.3, 1.8]$, corresponding to the linear energy range from about 0.5 to 63.1 TeV and a total number of 21 energy bins.

The binning was done with the standard analysis tools of the ctools software. `ctbin` was used to bin the event data (event cube), while the response cubes have been built using the tools `ctpsfcube` (PSF cube), `ctexpcube` (exposure cube) and `ctbkgcube` (background cube). The energy dispersion is not taken into account for the ctools analysis. The energy range of the analysis is however restricted to an interval where the energy bias is smaller than 10%, which yields good accuracy. A potential influence was also tested within the spectral reconstruction of the standard On-Off region analysis, in which a reconstruction of the energy spectrum of HESS J1826-130 was conducted with and without the forward folding method. The derived results are of very good agreement, well compatible within the 1σ statistical errors for all fit parameters (for details, see appendix Sec. A.2).

The count map of the analysis is shown in Fig. 4.14. It is smoothed with a normalized Gaussian kernel with a width (standard deviation) of 1 pixel, corresponding to a smoothing radius of $1.2'$. All maps presented within the ctools analysis have been smoothed applying these specifications. The pointing positions of the analyzed observations are indicated by

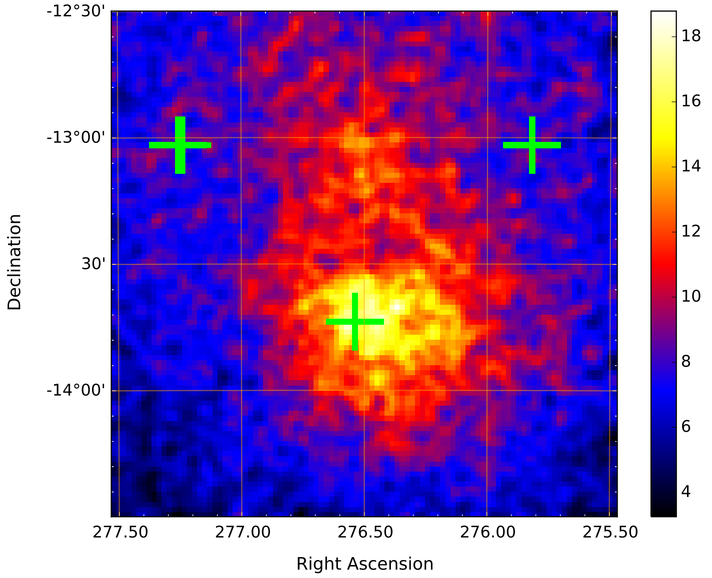

Figure 4.14: VHE γ-ray count map of the FoV as defined for the ctools likelihood template-fit analysis of data set N. The map was smoothed using a normalized Gaussian kernel with smoothing radius of $1.2'$. The color scale is given in units of raw counts after smoothing. The FoV is centered on the position $(\text{R.A., Dec.}) = (276.50°, -13.50°)$ and has a total width of $2° \times 2°$. The green crosses depict the pointing positions of the analyzed observations. HESS J1825-137 is clearly identifiable as bright emission spot. The emission of HESS J1826-130 seems identifiable in northern direction of it.

green crosses. The wobble offset of the runs to the position estimate of HESS J1826-130 is about 0.7°. The number of observations of the individual pointings are 52 runs in northern, 30 in southern, 58 in western and 53 in eastern offset direction. The northern pointing position is not visible in Fig. 4.14. Already in the raw count map, the emission of HESS J1826-130 seems identifiable in northern direction of the bright emission spot of HESS J1825-137, which is coincident with the southern observation pointing position.

4.3.2 Background template model

For the likelihood template-fit approach, a model component yielding an appropriate description of the hadronic background is needed. This background template model is constructed in the following way.

All available CT1-4 (H.E.S.S. I era) off-runs (runs without γ-ray sources in the FoV) and extragalactic runs are used for its construction. These observation runs are grouped in altitude and azimuth bins. For each of these bins, it is assumed that the background rate is constant with respect to observational conditions. All runs corresponding to one bin are stacked to calculate a mean expected differential background rate across the FoV. For the extragalactic runs, known γ-ray sources in the FoV are cut out. The stacking is done in a coordinate system which describes the distribution of events in the camera, the so-called instrument coordinate system (referred to as nominal coordinate system within H.E.S.S.), at each time defined by the current pointing position of the instrument. In this way, a three-dimensional background template model is constructed for each altitude azimuth bin. The background rate depends on the position (x,y) in the detector system and the

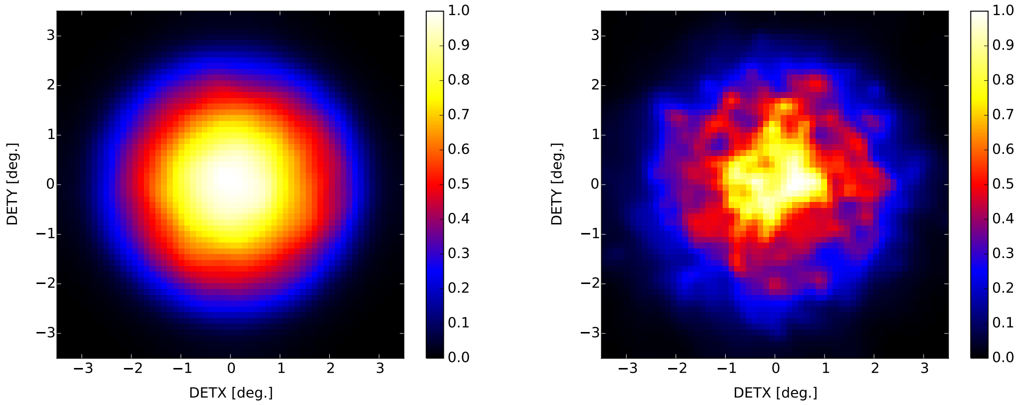

Figure 4.15: Background model templates in detector coordinates for the zenith angle band $[10°, 25°]$ and an energy of 1.0 TeV (left) and 9.6 TeV (right). The azimuth is 0°. The color scale represents the differential background rate, which is normalized to the maximum value, respectively.

event energy.

It is assumed that the hadronic background of each individual run can be described using the template model of the corresponding altitude azimuth bin, constructed prior to the analysis. Fig. 4.15 shows this template model exemplarily for the zenith angle range $10° - 25°$ and two different energies. In a first approximation, the background models are radially symmetric with respect to the camera center, where the background rate reaches its maximum. For a more detailed description and evaluation of the described background model, see Mayer (2014).

4.3.3 FoV template model development

The template model describing the entire FoV to be analyzed is developed iteratively in the following way.

In a first approach, the only component included in the FoV template is the background model component. The FoV template is fitted to the measured data using the standard maximum likelihood fitting ctool `ctlike`. After the fit, the residuals are inspected. At the position of remaining excess, a new model component is added to describe the remaining excess. The extended model is again fitted to the measured data. The TS value associated with each new source component is a measure of the source significance, cf. Sec. 3.4.1. If there is a significant improvement in the FoV description, the new component is added to the FoV template model. In this analysis, a TS improvement of $TS > 25$ is required in each step. The FoV model is developed using radial Gaussian components, with a pure power law assumption as spectral model description:

$$M_{Spat.}(\theta|E) = \frac{1}{2\pi\sigma^2}\exp\left(-\frac{1}{2}\frac{\theta^2}{\sigma^2}\right), \quad M_{Spec.}(E) = \Phi_0(E/1\,\mathrm{TeV})^{-\Gamma}\ . \tag{4.2}$$

θ denotes the angular separation from the center of the Gaussian distribution and σ its width. In very good approximation, projection effects are negligible for the given FoV and the radial Gaussian model can be considered being equivalent to a symmetric 2D Gaussian

Iter.	Model components	NPars	Changes	TS	$\sqrt{\text{TS}}$
1	Background	2 (2 free)	-	-	-
2	Background	2 (2 free)	-	2743.1	52.4
	1825	5 (5 free)	add		
3	Background	2 (2 free)	-	85.0	9.2
	1825	5 (4 free)	fix index		
	1825b	5 (4 free)	add (fixed index)		
4	Background	2 (2 free)	-	172.4	13.1
	1825	5 (1 free)	fix spatial p.		
	1825b	5 (1 free)	fix spatial p.		
	1826	5 (5 free)	add		
5	Background	2 (2 free)	-	53.6	7.3
	1825	5 (4 free)	free spatial p.		
	1825b	5 (4 free)	free spatial p.		
	1826	5 (5 free)	-		
	1825c	5 (4 free)	add (fixed index)		
6	Background	2 (2 free)	Re-fit	36.4	6.0
	1825	5 (5 free)	(free all model		
	1825b	5 (5 free)	parameters)		
	1826	5 (5 free)			
	1825c	5 (5 free)			

Table 4.5: Overview of the iterative FoV template model development. The TS values characterize the improvement in the FoV description and are a measure for the significance of the new components, which is approximated by calculating $\sqrt{\text{TS}}$. The spatial model of all components is given by a radial Gaussian model, the spectral model by a power-law. The total number of parameters per component is given (NPars), the number of free parameters and changes on each component are indicated. A detailed discussion is given in the text.

model. Φ_0 is the flux normalization at an energy of 1 TeV and Γ the spectral index of the power law model. During the development of the FoV template, it turned out that it is necessary to fix some of the parameters of the already established model components at certain points to ensure a stable fitting procedure and convergence of the fit. For a complex FoV as considered here, also the physical relation between different components describing the same source can be taken into account to stabilize the model development.

The steps of the iterative model development are summarized in Tab. 4.5. In Fig. 4.16 and Fig. 4.17, the model count map and the corresponding residual map is shown for each of the successive steps. The residual map is calculated as the difference in measured counts minus model counts.

In the first iteration, the model component describing the hadronic background is clearly visible: it is radially symmetric with respect to the center of the 4 observational pointing positions, mirroring the radially symmetric FoV acceptance of the H.E.S.S. instrument. The normalization of the background template is left free in all steps. Additionally, the spectral shape can be adjusted according to the assumption of a pure power law. The spectral index for this assumption is also left free. Both free parameters of the background model constitute corrections to the background template constructed from measured off-data and are consequently expected to be close to 1 (normalization) and 0 (spectral index) for the final FoV description.
In step two, a radial Gaussian component is added to describe the emission of HESS J1825-

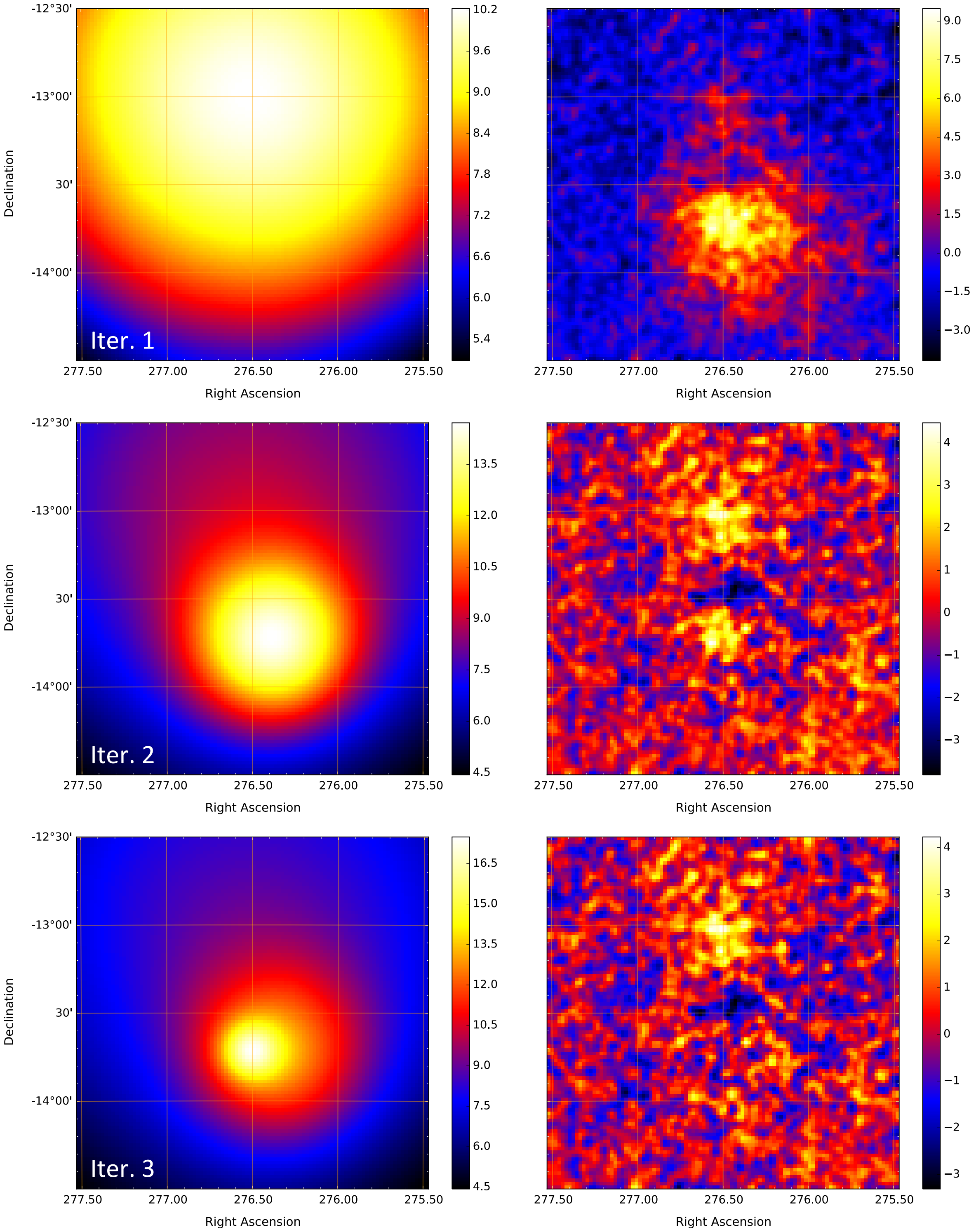

Figure 4.16: Successive development of the FoV model template. The left hand side shows the model count map for each step of the analysis, on the right hand side the residual map. The maps are smoothed with a Gaussian kernel, the color scale corresponds to raw counts after smoothing. HESS J1826-130 seems already identifiable in the residual map of the first iteration and gets clearly visible in the residuals in the second iteration step, after adding a first component to describe the bulk of the emission of HESS J1825-137.

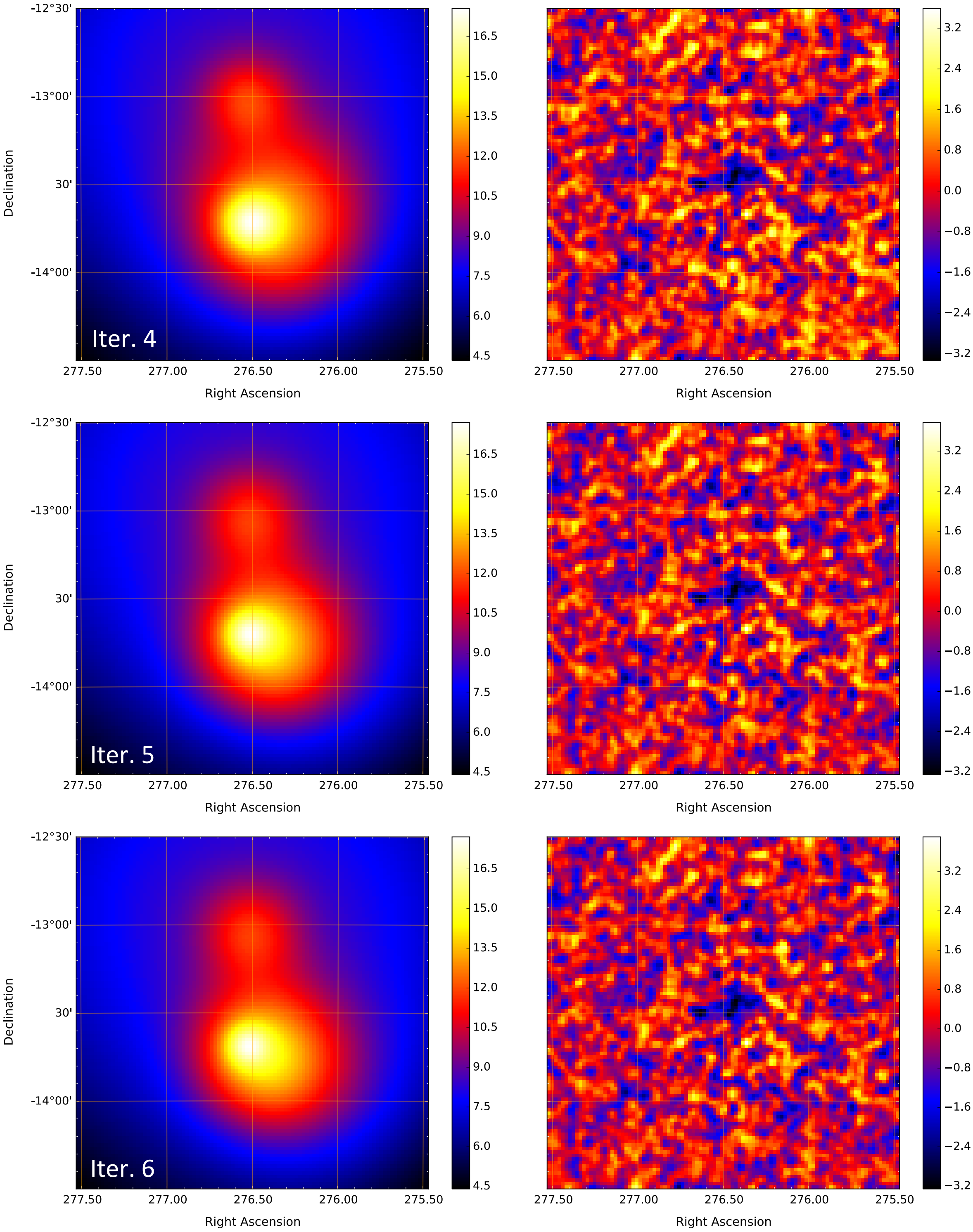

Figure 4.17: Same as Fig. 4.16, but for iteration steps 4-6. In the last iteration step, the parameters of all model components are set free and a global re-fit is carried out which allows for a fine adjustment of the found FoV description. After this step, the residuals are flat and no region of obvious significant γ-ray excess is left over.

137, clearly visible as a bright emission spot in the residuals of step one. The TS improvement of this component named 1825 in Tab. 4.5 results in an accordingly high value of 2743.1, corresponding to about 52.4σ in significance. The new component holds five free parameters in total. Three are needed for the spatial description covering position and extension of the Gaussian model. The other two free parameters are used for the spectral model, given by a power law assumption. The spectral index and the normalization is fitted. In the residuals, one identifies remaining emission of HESS J1825-137 as well as HESS J1826-130 in northern direction to it. Assuming that this first fitted model component results in parameters describing the bulk emission of HESS J1825-137, the spectral index of it is fixed.

The third step constitutes an improvement in the model description of HESS J1828-137. A second Gaussian component is added at the position of remaining emission of HESS J1825-137. The procedure is analogous to the one before, with the difference that the spectral index of the new component 1825b is fixed and set to the same value as for the component 1825. Thus, the 1825b component has 4 free parameters for the fit. The TS improvement is 85.0, corresponding to about 9.2σ. After this iteration, the residuals around the core region of HESS J1825-137 seem reasonably smooth without any obvious feature of excess left over. This indicates a first stable description of the emission of HESS J1825-137 by the two components 1825 and 1825b. The spatial parameters of these two components are fixed at this step.

The fourth iteration marks the detection step of HESS J1826-130. A Gaussian component is added at the position of remaining excess of step three. The new model component, named 1826, has five free parameters for the fit. Three of them belong to the spatial model (position and extension of the Gaussian), for the power law assumption the normalization and the spectral index is fitted. The TS improvement is 172.4, which corresponds to about 13.1σ significance. Thus, HESS J1826-130 is clearly detected in the ctools analysis.

In the residual map of step four, indications for a faint large scale excess towards the bottom right corner, potentially connected to HESS J1825-137, becomes visible. To test a further improvement of the FoV model, another Gaussian component 1825c with the same fixed spectral index as the already established two components describing HESS J1825-137 is added in iteration step five. The spatial parameters of the components 1825 and 1825b are freed again to allow for adjustment. The new component 1825c holds three free parameters belonging to the spatial model (position and extension), for the spectral description the normalization is fitted. The TS improvement in this step is 53.6, corresponding to about 7.3σ. After this iteration, no region of excess seems left over in the residuals for the entire FoV. This indicates a completion of the FoV template model.

The last step in the model development is a global re-fit. For this purpose, the spectral indices of the three components describing the emission of HESS J1825-137 are also freed. In the steps before, these have been fixed to the same value derived from the fit of the first iteration, which helps to stabilize the complex FoV model development. Thus, for the sixth iteration step, all parameters of all model components are free. This allows for a fine adjustment in the found FoV description. In total, there are 22 free parameters for the fit, 4×5 for the Gaussian components and two for the background model. The TS improvement for this last iteration is 36.4, which shows that there is indeed a significant improvement reached in this final step.

Having derived this FoV template model, two major aspects demand further discussion. The first one concerns the topic of spectral reconstruction and testing for a cutoff in the energy spectrum of HESS J1826-130, which is presented in the following section. The second one targets the question of a validation of the presented analysis approach and a

Comp.	Model type	Parameter	Fitted vale	Unit
1825	Power law	Normalization	8.22±2.40	$10^{-12}\,(\mathrm{s\,cm^2\,TeV})^{-1}$
		Spectral index	2.26±0.06	
	Radial Gaussian	R.A.	276.44±0.03	deg.
		Dec.	−13.78±0.03	deg.
		Sigma	0.27±0.03	deg.
1825b	Power law	Normalization	0.53±0.19	$10^{-12}\,(\mathrm{s\,cm^2\,TeV})^{-1}$
		Spectral index	1.91±0.12	
	Radial Gaussian	R.A.	276.53±0.02	deg.
		Dec.	−13.69±0.02	deg.
		Sigma	0.07±0.01	deg.
1825c	Power law	Normalization	8.88±2.45	$10^{-12}\,(\mathrm{s\,cm^2\,TeV})^{-1}$
		Spectral index	2.49±0.09	
	Radial Gaussian	R.A.	276.07±0.11	deg.
		Dec.	−14.03±0.07	deg.
		Sigma	0.40±0.03	deg.
1826	Power law	Normalization	1.70±0.22	$10^{-12}\,(\mathrm{s\,cm^2\,TeV})^{-1}$
		Spectral index	2.12±0.06	
	Radial Gaussian	R.A.	276.51±0.02	deg.
		Dec.	−13.04±0.02	deg.
		Sigma	0.18±0.02	deg.
BG	Background template	Prefactor	1.05±0.01	
		Spectral index	0.04±0.01	

Table 4.6: Overview of the final FoV description derived in the ctools analysis. The different components are listed together with the model types used for spatial and spectral modeling. The resulting best-fit values are given together with their statistical uncertainties. The normalization (prefactor) for the spectral models refers to an energy of 1 TeV.

verification of the found FoV description through advanced analysis checks. This aspect will be discussed in detail in Sec. 4.5.

4.3.4 Spectral and morphological results

The derived best-fit values for the parameters of the different model components of the found FoV description are summarized in Tab. 4.6. The fitted values of the two free background template parameters lie close the expectation, indicating small corrections on the constructed background template and thus a proper description of the hadronic background as being present in the measured data. The results for the individual model components give a morphological and spectral description for the VHE γ-ray emission from both HESS J1825-137 and HESS J1826-130. The main focus of this analysis is on the source HESS J1826-130, on which the following discussion will concentrate. The derived results characterizing HESS J1825-137 will be discussed in more detail in Sec. 4.5, providing the opportunity for a validation of this analysis approach via a comparison of the derived results with already published analysis results.

Comp.	Model type	Parameter	Fitted vale	Unit
1825	Power law	Normalization	7.77±2.36	$10^{-12}\,(\mathrm{s\,cm^2\,TeV})^{-1}$
		Spectral index	2.26±0.06	
	Radial Gaussian	R.A.	276.45±0.03	deg.
		Dec.	−13.79±0.03	deg.
		Sigma	0.27±0.03	deg.
1825b	Power law	Normalization	0.56±0.20	$10^{-12}\,(\mathrm{s\,cm^2\,TeV})^{-1}$
		Spectral index	1.92±0.12	
	Radial Gaussian	R.A.	276.53±0.02	deg.
		Dec.	−13.68±0.02	deg.
		Sigma	0.07±0.01	deg.
1825c	Power law	Normalization	9.21±2.43	$10^{-12}\,(\mathrm{s\,cm^2\,TeV})^{-1}$
		Spectral index	2.47±0.08	
	Radial Gaussian	R.A.	276.07±0.10	deg.
		Dec.	−14.01±0.06	deg.
		Sigma	0.40±0.03	deg.
1826	Power law with exponential cutoff	Normalization	2.02±0.27	$10^{-12}\,(\mathrm{s\,cm^2\,TeV})^{-1}$
		Spectral index	1.73±0.13	
		Cutoff Energy	14.2±4.6	TeV
	Radial Gaussian	R.A.	276.51±0.02	deg.
		Dec.	−13.06±0.02	deg.
		Sigma	0.21±0.02	deg.
BG	Background template	Prefactor	1.05±0.01	
		Spectral index	0.04±0.01	

Table 4.7: Overview of the final FoV description derived in the ctools analysis, using a power law with exponential cutoff for the spectral model of HESS J1826-130. The different components are listed together with the model types used for spatial and spectral modeling. The normalization for the spectral models refers to an energy of 1 TeV.

Testing for a cutoff in the energy spectrum of HESS J1826-130

To approach the question whether or not there is a cutoff in the energy spectrum of HESS J1826-130, the spectral model of a pure power law is replaced by the assumption of a power law with exponential cutoff:

$$M_{Spec}(E) = \Phi_0(E/1\,\mathrm{TeV})^{-\Gamma}\,\exp\left(-E/E_{cut}\right)\,, \tag{4.3}$$

with E_{cut} denoting the cutoff energy. The other model components of the FoV description remain unchanged. Iteration step number six is re-evaluated with the changed spectral model of HESS J1826-130, i.e. a re-fit is carried out.

The TS value calculated from the likelihood ratio of the FoV model using the power law against the FoV model using the cutoff power law as spectral description of HESS J1826-130 is 19.3, corresponding to 4.4σ preference for the cutoff power law model.

The best-fit values from the re-fit are summarized in Tab. 4.7. Minor changes in the results for the components describing HESS J1825-137 are observed in comparison to Tab. 4.6, well compatible within the 1σ errors. At the level of accuracy of the statistical

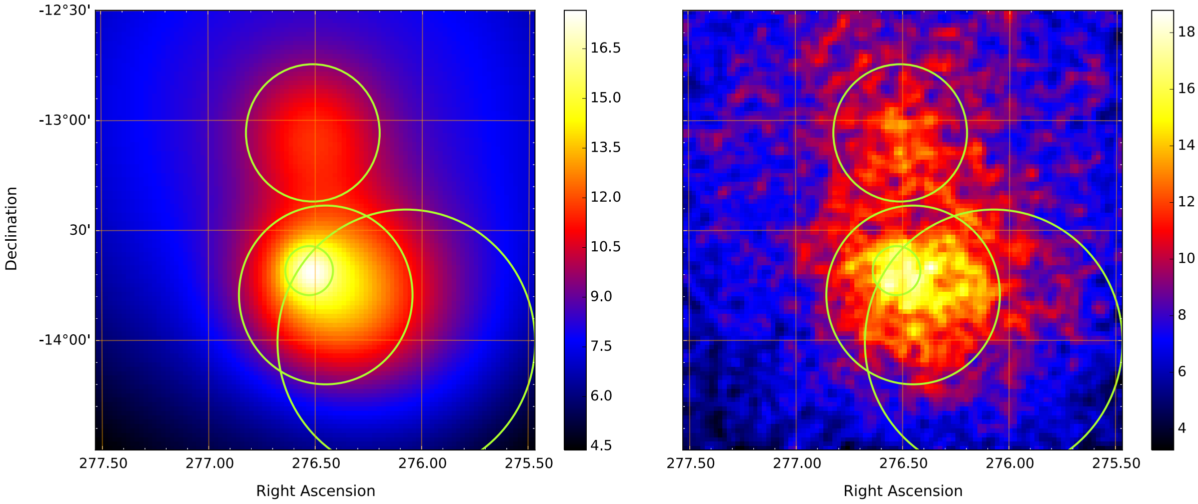

Figure 4.18: Model count map of the FoV template model derived within the ctools analysis (left). The individual components of the FoV model are depicted by the green lines, showing the 68% containment radius of the individual components as given in Tab. 4.7. The map on the right hand side is the FoV count map (measured counts) and is shown for comparison. Both maps are smoothed with a Gaussian kernel, the color scale corresponds to raw counts after smoothing.

errors, no changes are observed in the best-fit values for the parameters of the background component. The extension and consequently the normalization of the component 1826 are found at slightly larger values, however also compatible with the previous results regarding the statistical errors. A significant change is observed in the spectral index of this component, which changes from 2.12 ± 0.06 to 1.73 ± 0.13 when changing to the cutoff power law assumption. The fitted value of the cutoff energy is 14.2 ± 4.6 TeV.

The presented results show that the FoV description derived by the FoV model using the exponential cutoff power law assumption for HESS J1826-130 yields the best description of the measured data. To give an illustrating overview of this model, the corresponding FoV model map, overlaid with the individual components is shown in Fig 4.18 together with the FoV count map for comparison.

Spectral reconstruction

The energy spectrum of HESS J1826-130 is reconstructed using the cscript `csspec` of the ctools software. The script computes the source spectrum by re-fitting the provided FoV model in a set of predefined spectral bins. All model parameters except the normalization of the source of interest and the ones of the background template are fixed for the calculation. If the source cannot be detected with $\mathrm{TS} > 4$, an upper limit is calculated for the corresponding energy bin.

The reconstructed spectrum for both spectral model assumptions of HESS J1826-130 are shown together with the best-fit models in Fig. 4.19. The likelihood based analysis approach allows for a comparison of the two different model assumptions, but does not directly provide a goodness-of-fit estimate. Therefore, the corresponding χ^2 values are calculated. For this calculation, also the non-significant spectral points ($\mathrm{TS} < 4$ per bin) are used. The resulting values are $\chi^2/d.o.f. = 23.5/9$ for the power law model, the

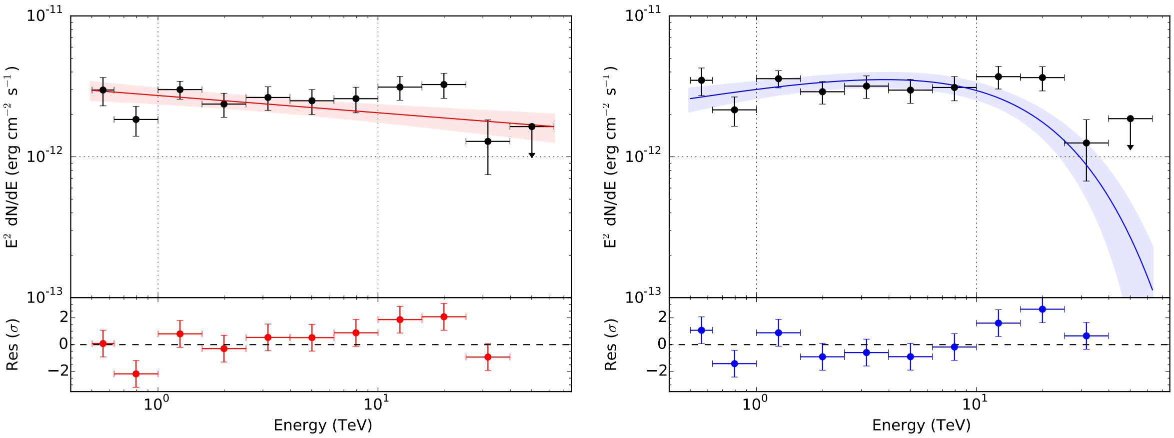

Figure 4.19: Energy spectrum of HESS J1826-130 as reconstructed within the ctools analysis shown together with the best-fit models of a power law (left) and power law with exponential cutoff (right). The shaded bands represent the 68% confidence region of the best-fit models. Note that the fit is based on the full fine-binned data set while the shown spectral data points are calculated thereafter and are model dependent. See text for further discussion.

equivalent p-value being 0.005. For the cutoff power law the result is $\chi^2/d.o.f. = 16.1/8$, corresponding to a p-value of 0.04. These results also indicate that the pure power law assumption seems not well suited to describe the data, whilst the exponential cutoff model provides a more adequate description.

An interesting question is how the results derived by the likelihood based ctools analysis approach compare to the ones derived by the standard analysis approach presented before. This topic is addressed in the following section.

4.4 Comparison of analysis results

This section provides a direct comparison of the analysis results for HESS J1826-130 derived by the standard On-Off region analysis approach to those derived by the ctools analysis approach. An overview of the morphological characterization is followed by a detailed comparison of the derived energy spectra.

4.4.1 Morphological characterization

For both analysis approaches, the source morphology was assumed to follow a symmetric 2D Gaussian model. One should note the main difference in the derivation of the presented results. The morphological analysis for the standard On-Off region approach is based on analysis of the excess count map and thus decoupled from any spectral model assumption of the source. In contrast, the likelihood based template-fit approach of the ctools analysis takes the morphological and spectral description simultaneously into account.

Table 4.8 gives a summary of the derived results. For completeness, these are given for the ctools analysis for both different spectral model assumptions of a pure power law and power law with exponential cutoff. The derived position estimates are in good agreement. The extension of the Gaussian is for the cutoff power law model found at a slightly larger value than derived within the standard analysis approach, however also well compatible within statistical errors.

Analysis	R.A. [deg.]	Dec. [deg.]	Width σ [deg.]
HAP (sherpa fit)	276.50 ± 0.03	-13.03 ± 0.03	0.17 ± 0.02
ctools (PL)	276.51 ± 0.02	-13.04 ± 0.02	0.18 ± 0.02
ctools (ECPL)	276.51 ± 0.02	-13.06 ± 0.02	0.21 ± 0.02

Table 4.8: Overview of the fitted parameter values of the 2D symmetric Gaussian model describing HESS J1826-130 for the different analysis approaches. HAP denotes the results derived within the standard On-Off region analysis approach. For the ctools analysis, the results derived using the two different spectral model assumptions of a power law (PL) and power law with exponential cutoff (ECPL) are given.

	ctools data set N	HAP data set N	HAP data set C
Power law model			
Spectral index	2.12 ± 0.06	2.03 ± 0.06	2.07 ± 0.04
Flux normalization	1.70 ± 0.22	0.83 ± 0.08	0.94 ± 0.06
Flux > 1 TeV	1.52 ± 0.21	0.79 ± 0.06	0.87 ± 0.05
Cutoff power law model			
TS (ECPL-PL)	19.3 (4.4σ)	4.3 (2.1σ)	12.7 (3.6σ)
Spectral index	1.73 ± 0.13	1.69 ± 0.14	1.66 ± 0.11
E_{cut} [TeV]	14.2 ± 4.6	$19.6^{+12.9}_{-5.5}$	$13.5^{+4.7}_{-2.7}$
Flux normalization	2.02 ± 0.27	0.77 ± 0.10	0.89 ± 0.07
Flux > 1 TeV	1.96 ± 0.37	0.82 ± 0.06	0.91 ± 0.05

Table 4.9: Overview of the spectral best-fit parameter values for HESS J1826-130 derived from the ctools and the standard On-Off region analysis approach. The different data sets used for analysis are indicated. The flux normalization refers to an energy of 1 TeV and is given in units of $10^{-12}\,\mathrm{s}^{-1}\mathrm{cm}^{-2}\mathrm{TeV}^{-1}$. The total flux above 1 TeV is given in units of $10^{-12}\,\mathrm{s}^{-1}\mathrm{cm}^{-2}$. The TS values of the corresponding likelihood ratio tests comparing the cutoff power law model with the pure power law model are also given.

4.4.2 Reconstructed energy spectrum

This section gives a comparison of the derived energy spectra and corresponding best-fit spectral model parameters of HESS J1826-130. First, this comparison is given for the energy spectra derived from the standard On-Off analysis but for the different data sets N and C. This is followed by a comparison to the results from the ctools analysis which is based on data set N.

The energy spectra from the standard On-Off region analysis for the two different data sets are shown in Fig. 4.20. There is a good agreement between the reconstructed flux points and the overall spectral shape. For the analysis of data set C, the cutoff seems however a bit more pronounced, found at a lower energy than for the analysis of data set N. This is also mirrored in the resulting best-fit parameter values, summarized in Tab. 4.9. The results are however compatible within errors, both for the power law model and the power law model with exponential cutoff. The main difference is the fact that the cutoff power law model is only significantly preferred (TS $>$ 9) for the analysis of the combined data set C, i.e. the cutoff is only detected for the larger statistics data set.

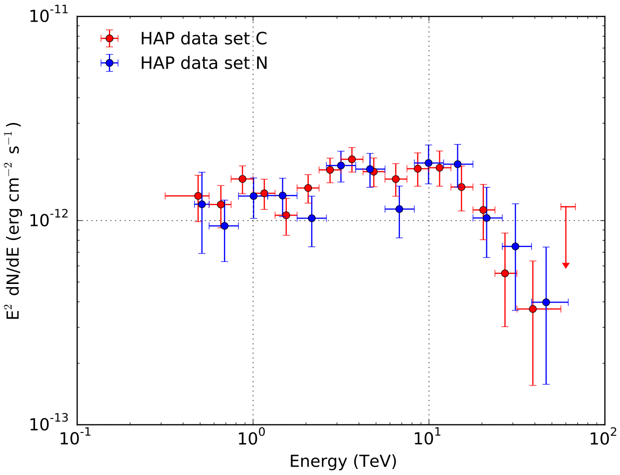

Figure 4.20: Comparison of the reconstructed energy spectrum of HESS J1826-130 from the standard On-Off region analysis approach for the two different data sets C and N. There is an overall good agreement of the reconstructed data points. For the larger data set C, the cutoff is more pronounced and found at a slightly smaller energy than for new data set.

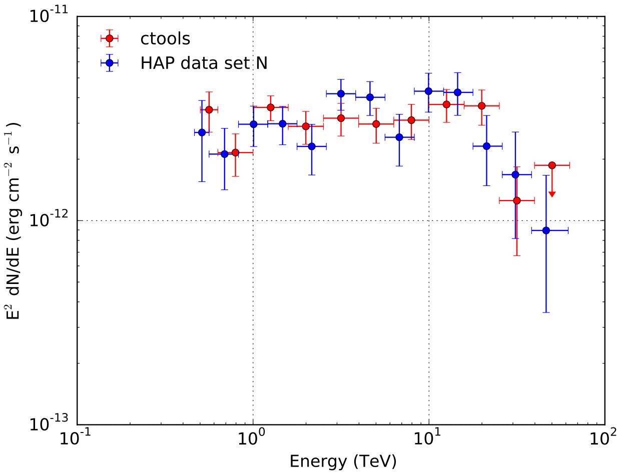

Figure 4.21: Comparison of the reconstructed energy spectrum of HESS J1826-130 from the standard On-Off region analysis approach and the ctools analysis. The flux points of the HAP On-Off analysis have been corrected to the same solid-angle coverage as the ctools Gaussian model to allow for direct comparison. See text for further discussion.

Comparing the best-fit results from the ctools analysis to those of the standard On-Off analysis (Tab. 4.9), one main difference becomes visible. The flux normalization and thus the total flux above 1 TeV differs significantly. To explain this difference, it is necessary to take into account the fact that the On-Off results are derived from a region of fixed size which may lead to cutting off the emission tails of the source. This effect can, depending on the source morphology, lead to a significant loss of flux from the source. For a radial Gaussian model, the fractional loss compared to a restricted region of size s is

$$c_{spat}^{-1} = \int_0^{2\pi} \mathrm{d}\varphi \int_0^{s} \theta \, \mathrm{d}\theta \, \frac{1}{2\pi\sigma^2} \, \exp\left(-\frac{1}{2}\frac{\theta^2}{\sigma^2}\right) = 1 - \exp\left(-\frac{s^2}{2\sigma^2}\right) \; . \tag{4.4}$$

To get to a correct physical flux estimate for the On-Off analysis and to enable a direct comparison to the ctools analysis results, it is therefore necessary to take into account a spatial correction factor c_{spat}, given by the inverse of the fractional loss as defined in Eq. 4.4. The radius of the On-region in the analysis is $s = \sqrt{(0.05)}^\circ \approx 0.22^\circ$. The fitted width of the Gaussian model from the ctools analysis is $\sigma = 0.21^\circ$ (cf. Tab. 4.7). Thus, for a direct comparison to the ctools analysis, a correction factor of $c_{spat} = 1/0.43 = 2.32$ needs to be taken into account. Fig. 4.21 shows a comparison of the spectral data points derived within the ctools analysis and the On-Off region analysis using the same data set N, with the flux points from the On-Off analysis being accordingly corrected. After this correction, there is a good agreement in terms of absolute values of the flux points, as well as a good agreement of the overall spectral shape. Concerning a comparison of the best-fit results characterizing the spectral shape such as spectral index or cutoff energy between the ctools analysis and the On-Off analysis, these are compatible within errors. Interestingly, the cutoff power law is for the ctools analysis using only the new data set N significantly preferred over the pure power law assumption, whereas for the standard On-Off region analysis, this is only the case for enlarged statistics shown by the analysis of data set C.

Note that overall systematic errors for spectral analysis with H.E.S.S. are estimated to be 20% for the flux measurement, while for the spectral index it is about 0.1. The systematic error on the cutoff energy is also expected to be about 20% (cf. Aharonian et al. 2006a).

4.5 Analysis verification and advanced analysis checks

The likelihood based template-fit analysis approach is a rather new analysis technique in the VHE domain and thus for the analysis of H.E.S.S. data. Therefore, different checks have been carried out to verify the analysis procedure and the gained results of the ctools analysis, which will be presented in this section.

4.5.1 Result stability

To check the robustness of the results derived for HESS J1826-130 in the sense of a potentially strong dependence on the FoV model description of the emission from HESS J1825-137, the model description of HESS J1825-137 with three Gaussian components was reduced to a description with only two Gaussian components. Only minor differences in the final parameter values derived for HESS J1826-130 are observable for this change, well compatible within statistical errors. Tab. 4.10 gives an overview. This result indicates a robust description of the emission of HESS J1826-130, not dependent on the exact model description of HESS J1825-137. To illustrate the difference in the FoV models using two or three Gaussian components, these are overlaid on the FoV count map in Fig. 4.22.

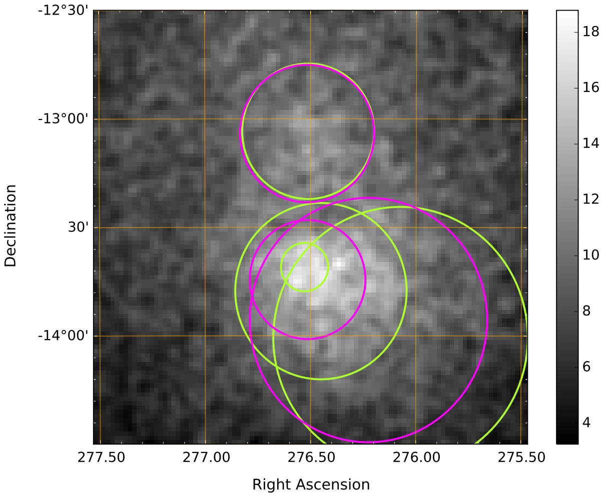

Figure 4.22: Comparison of a FoV template which uses a 3 Gaussian model (green) to describe the emission of HESS J1825-137 and a model using only 2 Gaussian components (magenta). The circles decpict the 68% containment radius, respectively. The smoothed count map is shown in gray-scale to allow for a better comparison.

	ctools (3 Gaussian)	ctools (2 Gaussian)
Spectral index	1.73 ± 0.13	1.69 ± 0.13
E_{cut} [TeV]	14.2 ± 4.6	13.3 ± 4.1
Flux normalization	2.02 ± 0.27	2.01 ± 0.27
R.A.	276.51 ± 0.02	276.52 ± 0.02
Dec.	-13.06 ± 0.02	-13.07 ± 0.02
Width (σ)	0.21 ± 0.02	0.21 ± 0.02

Table 4.10: Comparison of the resulting best-fit parameter values for the model description of HESS J1826 when changing the model which describes the emission of HESS J1825-137 from three Gaussian components to only two Gaussian components. The flux normalization refers to an energy of 1 TeV and is given in units of $10^{-12}\,\mathrm{s}^{-1}\mathrm{cm}^{-2}\mathrm{TeV}^{-1}$. The total flux above 1 TeV is given in units of $10^{-12}\,\mathrm{s}^{-1}\mathrm{cm}^{-2}$.

4.5.2 Pull distributions

The calculation of pull distributions can be seen as a self-consistency check on the analysis procedure and provides the opportunity to check for a potential bias of the parameter estimators of the individual model components. The pull distributions are generated in the following way: the measured data are simulated with the ctools tool `ctobssim` according to the derived FoV model of the analysis and according to the statistics of the measured data set. The ctools analysis is carried out on these simulated data, exactly in the same steps as described in Sec. 4.3.3. This is done for a total set of 1000 simulations. The results from these simulations are used to generate the pull distributions for the individual model parameters.

Pull distributions for the power law model description of HESS J1826-130

The pull distributions using the FoV description with the power law model as spectral description of HESS J1826-130 are shown in Fig 4.23. The according FoV model is given in Tab. 4.6.

The distributions are for all parameters centered around the simulation input values, shown as red dashed lines in the plots. A Gaussian is fitted to each of the distributions, which is well suited to describe their basic shape. The mean and width of the distributions as determined from the fit are in agreement with the the values calculated from the statistical distribution of the data (sample mean, sample standard deviation). The relative bias is for all parameters smaller than 1%, being calculated from the sample mean value and the simulation input values. The results show that the ctools analysis as carried out on the given FoV yields correct results with good accuracy for the model parameters of the HESS J1826-130 component, assuming the validity of the found FoV description. The estimated bias is very small for all parameters and the true values are located well within the 1σ uncertainties, depicted by the gray shaded bands.

Regarding the pull distributions of the parameters of the three model components describing HESS J1825-137, the situation is more complex. The three Gaussian model components might interchange among themselves which can make a clear interpretation difficult. Furthermore, the large scale component 1825c can in some cases not be recovered and the normalization of it is set to zero, effectively replacing the triple Gaussian description by a two Gaussian description. This also influences the results for the other two components 1825 and 1825b. The situation stabilizes however when changing to a two Gaussian description of HESS J1825-137, for which the pull distributions have also been generated. Fig. 4.24 gives an exemplary view on this behavior, showing the pull distribution of the width of one Gaussian component of the HESS J1825-137 description in the two Gaussian and the triple Gaussian scenario.

The resulting pull distributions for the parameters of HESS J1826-130 for the two Gaussian model description of HESS J1825-137 have also been calculated and do not change in terms of accuracy or bias with respect to those shown above for the triple Gaussian model. This proves again the robustness of the results derived for HESS J1826-130.

Pull distributions for the cutoff power law model description of HESS J1826-130

The pull distributions for the FoV template using the power law model with exponential cutoff as spectral description of HESS J1826-130 have also been generated. This FoV model is summarized in Tab. 4.7.

The results for the model component describing HESS J1826-130 are in terms of accuracy and bias comparable to those shown above for the power law assumption concerning the spatial model parameters and the flux normalization.

For the parameters describing the spectral shape, the spectral index and the cutoff energy, the pull distributions are however distorted. A significant overflow number of entries in the bins corresponding to the respective start values of the fit parameters are observable. Closer inspection of these artifacts revealed problems connected to the numerical optimization routine, which is based on the iterative Levenberg-Marquardt method (Marquardt 1963). This is to be seen as a result of the complexity of fitting a power law model with exponential cutoff, which is quite sensitive to the provided start parameters and can

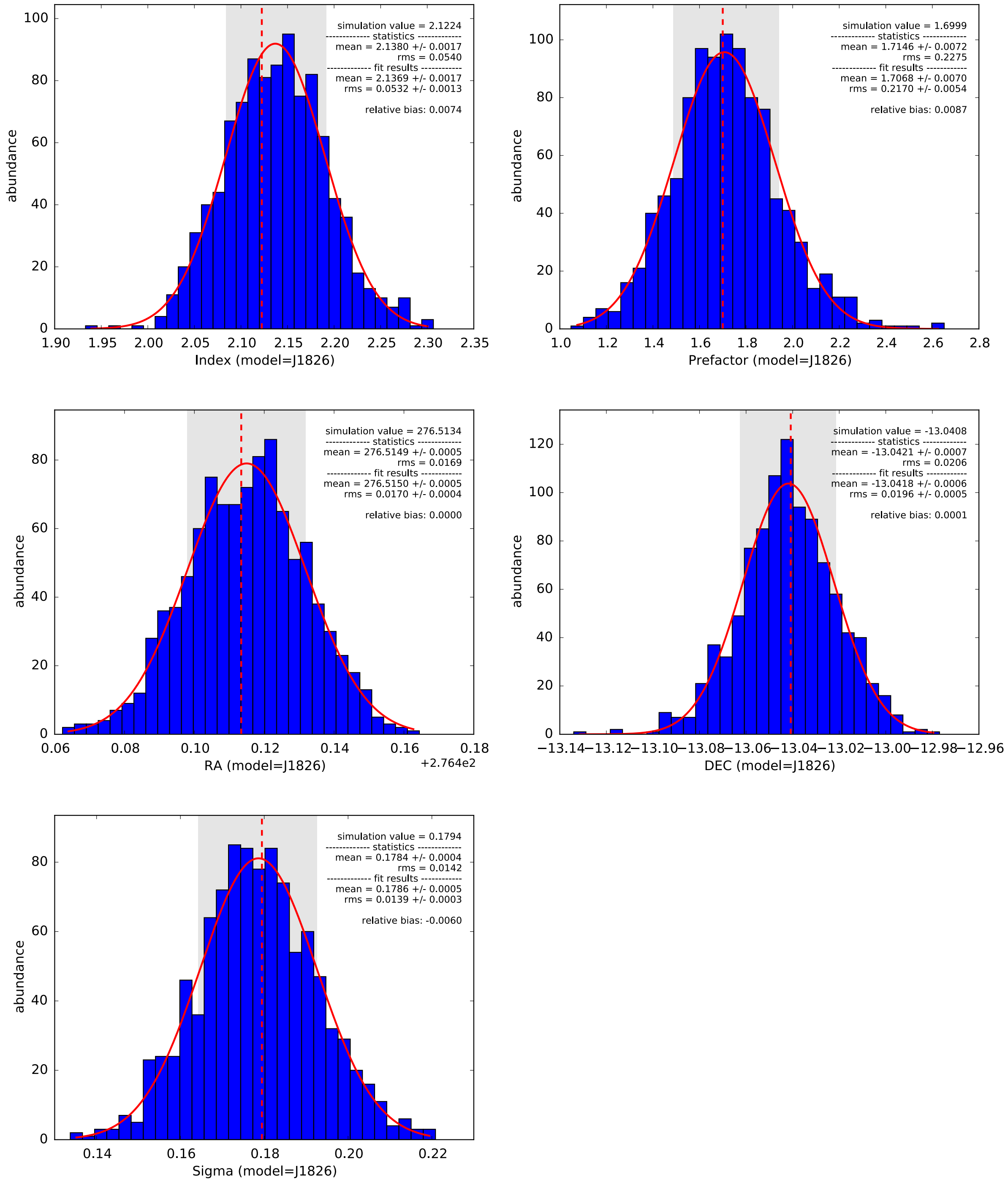

Figure 4.23: Pull distributions for all fitted parameters of the HESS J1826-130 model component. The mean and standard deviation (rms) of the shown distributions calculated from the statistical distribution (statistics) as well as derived by a Gaussian fit (fit, red line) are given in the plots. The simulation input values are also given, indicated in the plots by dashed red lines. The gray shaded bands depict the 1σ interval around the reconstructed mean values.

easily result in numerical problems. Therefore, the start values for the fit are set closer to the true input simulation values and the pull distributions are re-calculated. By this, the situation can be considerably improved, the number of entries in the bin corresponding

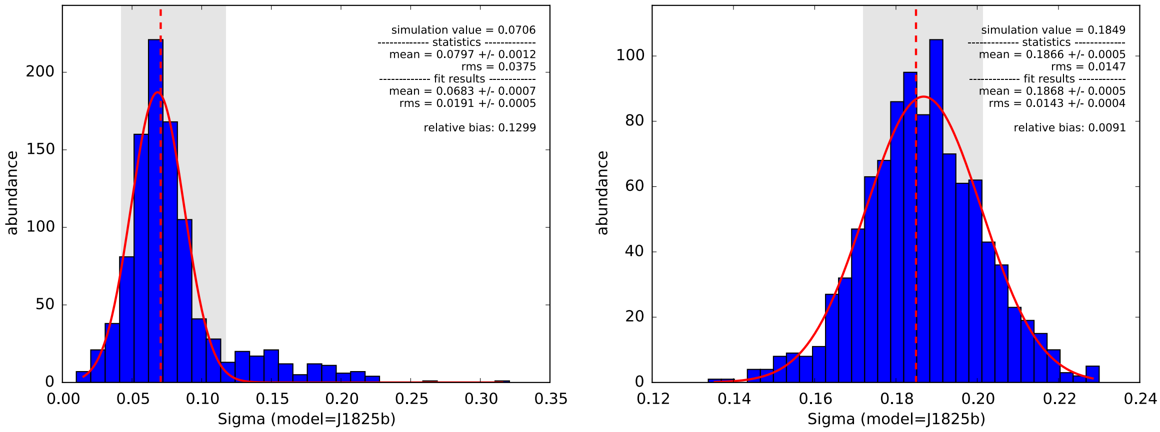

Figure 4.24: Pull distributions for the width of the component 1825b in the triple Gaussian description (left) and the two Gaussian (right) model description of HESS J1825-137. In the triple Gaussian model, the distribution shows outliers to too large sizes mainly due to problems in fitting the large scale Gaussian component 1825c. See text for further discussion.

to the start value can for the cutoff energy be reduced from about 600 to 230. However, the effect is still strongly visible. The pull distribution for the cutoff energy derived for improved fit start parameters is shown in Fig. 4.25, left.

To exclude a connection of the outlined problem to a possible divergence of the cutoff energy when fitting this parameter directly, an alternative cutoff power law model, which employs the inverse cutoff energy as fit parameter, was implemented in GammaLib and used to generate the pull distributions. However, no improvement with respect to the shown results was reached by this approach. Future investigations could encompass the usage of alternative optimization algorithms, like e.g. Nelder-Mead routines, which was however beyond the scope of this thesis.

Apart from the addressed numerical problems, it is visible in Fig. 4.25 that the distribution is not well centered on the true simulation input value, which hints to a small intrinsic bias of the estimator. To calculate this bias, a cleaned distribution is used, generated by requiring a minimum difference of 10^{-3} in terms of absolute value of the fitted parameter compared to the fit start value, taken as indication that the optimizer started to work properly. This distribution is shown in Fig. 4.25, right. As the distribution seems slightly skewed, the median m is used to calculate the bias, which is about the same as the mean of the fitted Gaussian. The calculated bias is $b_{ec} = m - E_{cut,sim} = 10.4 - 14.2 = -3.8$ in units of TeV. The best-fit result for the cutoff energy from the analysis can be corrected according to this bias from $E_{cut} = 14.2\,\text{TeV}$ to $E_{cut} = 18.0\,\text{TeV}$. Regarding the statistical error of 4.6 TeV (cf. Tab. 4.7), the systematic uncertainties related to this discussion should after this correction be negligible. In former studies, such a bias correction has been verified to yield an appropriate result in the sense that after the correction, a newly generated pull distribution centers around the uncorrected value.
Applying the same procedure to the spectral index, a bias of $b_{si} = 1.66 - 1.73 = -0.07$ is calculated. Accordingly, the bias corrected value for the spectral index is 1.80, with a remaining systematic uncertainty of 0.13.

For the model components describing HESS J1825-137, the situation for the pull distributions is comparable to the one discussed above for the FoV description using the pure power

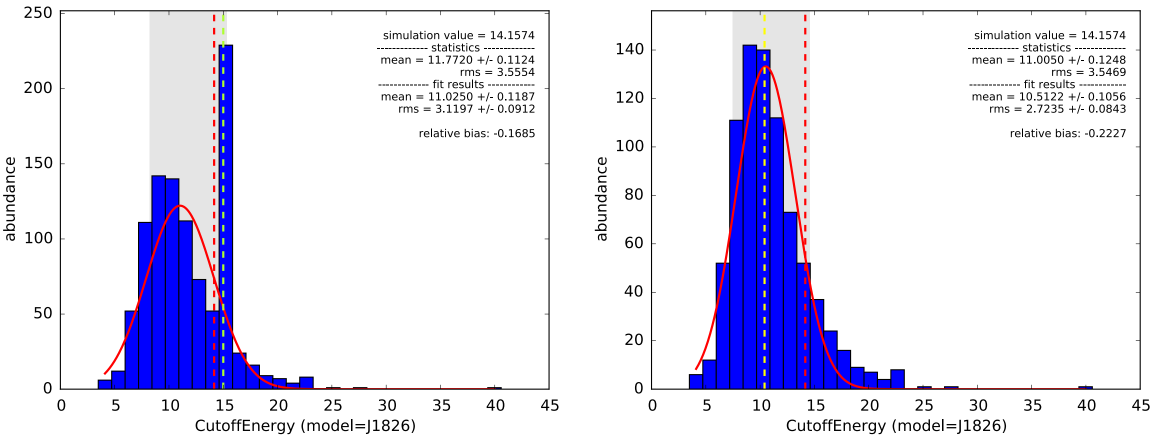

Figure 4.25: *Left:* Pull distribution for the cutoff energy of the model component for HESS J1826-130. The start value for the fit is shown as green dashed line, the true value (simluation input value) is shown as red dashed line. Due to numerical optimization problems, there is an overflow of entries in the bin corresponding to the start value. *Right:* Same pull distribution, cleaned from those analysis runs for which numerical optimization problems are observed. The total number of entries of this distribution is reduced to 808 compared to 1000 in the original one shown left. The yellow line depicts the median of the distribution.

law description for the 1826 component, which makes a further discussion redundant.

4.5.3 Residual significance map statistics

To verify the found FoV model in terms of completeness and to further test the quality of the model description, it is useful to calculate a residual significance map. An inappropriate modeling of excess regions or missing components are expected to become visible as bright spots ($> 5\sigma$) in such a map. An inspection of its entry distribution allows to verify the quality of the overall FoV description.

The residual significance map is calculated in the following way. For each pixel, the null hypothesis, given by the found FoV model, is tested against the alternative hypothesis which is given by the assumption of an additional source. The calculation of the source significance is carried out in the same way as shown in Li & Ma (1983), with the difference that the background is not a measured quantity but dictated by an expectation value provided by the FoV model. The according formula for the significance S_i per pixel is given by

$$S_i = \mathrm{sign}(d_i - m_i) \times \sqrt{2\left(d_i \ln\left(\frac{d_i}{m_i}\right) - d_i + m_i\right)} \tag{4.5}$$

with d_i the number of measured counts in pixel i and m_i the corresponding number of predicted model counts. Under the null hypothesis, the entry distribution of the residual significance map is expected to follow a standard normal distribution, which was also verified through simulations.

The residual significance map calculated for the final FoV model as given in Tab. 4.7 is shown in Fig. 4.26, left. The map is correlated with a top-hat kernel with a size equal to the H.E.S.S. PSF to reflect the sensitivity to point sources. It looks smooth without any spots brighter than 4σ, indicating a good model description. A slight negative feature

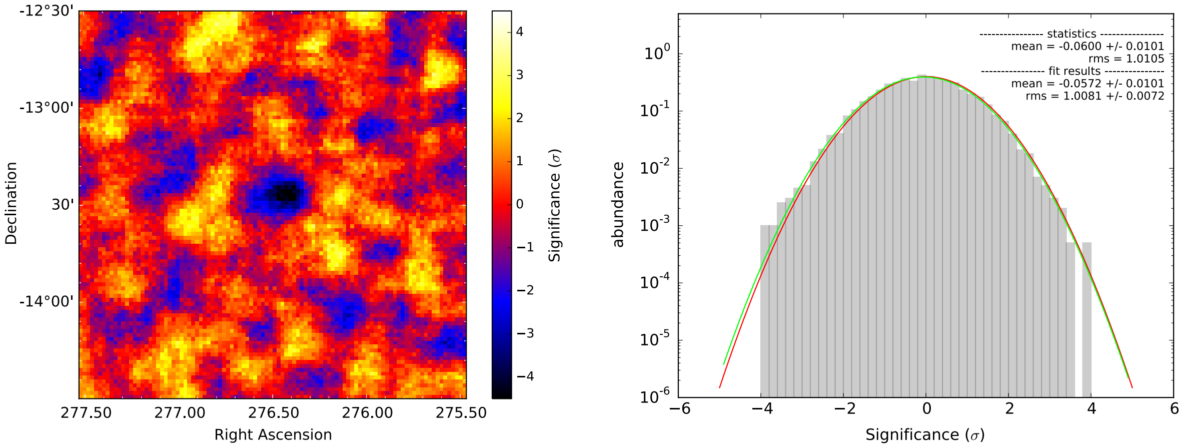

Figure 4.26: Residual significance map (left) and residual significance map entry distribution (right). The map was correlated with a top-hat kernel with a size of 0.1°, the typical width of the H.E.S.S. PSF. The entry distribution is well described by a standard normal distribution, shown as red line. The green line depicts a Gaussian fit to the data. The mean and the width (rms) of the distribution is indicated.

seems visible in the middle of the map, possibly related to the fact that the emission of HESS J1825-137 cuts off rather sharp in northern direction, whereas the model description uses Gaussian components, which might lead to a slight over-description in this area.

The entry distribution is shown on the right hand side of Fig. 4.26. Its shape is well described by a standard normal distribution, overlaid in red. A Gaussian fit to the data yields a mean value of -0.06 ± 0.01 and a width of $\sigma = 1.008 \pm 0.007$. This result shows that the derived FoV template is well suited to describe the measured data and thereby verifies all components included in this model.

4.5.4 Comparison of FoV significance maps, FoV TS map

A FoV significance map gives an illustrative overview of the overall emission morphology of the region under investigation. It evaluates the source significance of each pixel with respect to the background-only hypothesis. For the ctools analysis approach, this means Eq. 4.5 is evaluated with respect to the FoV template including only the model component describing the hadronic background. For the standard On-Off region analysis, the background is estimated from an Off-region in the FoV and Eq. 3.5 is used to calculate a pixel-wise significance.

The FoV significance map, calculated from both the standard On-Off region analysis approach and the ctools analysis approach, is shown in Fig. 4.27. The 5, 10 and 15σ contours are overlaid in color. Generally, there is a good agreement of the emission morphology of the maps, indicating again a good agreement between the two different analysis approaches. HESS J1826-130 is clearly visible as northern extension of the bright emission region of HESS 1825-137.

For the ctools analysis approach, it is however more intuitive to calculate a FoV TS map instead of a FoV significance map as discussed above. For a FoV TS map, a hypothetical, point-like test-source is moved over the considered sky region. With the position of the test-source being fixed on the pixel center, a fit evaluates the model hypothesis of back-

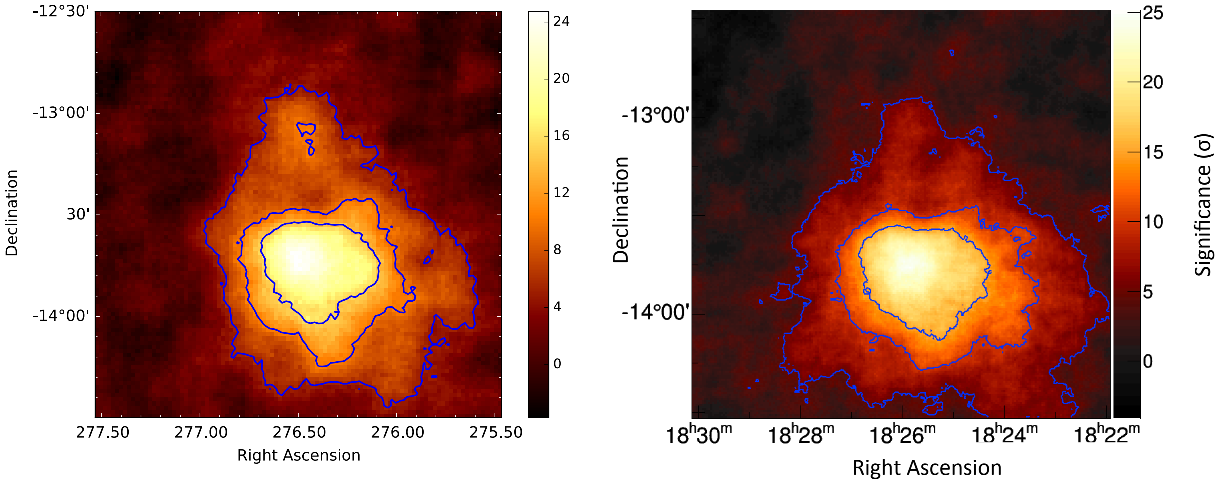

Figure 4.27: FoV significance map calculated within the ctools analysis (left) and the standard On-Off region analysis approach (right). The color scale gives the source significance above background. The blue lines depict the $5, 10$ and 15σ contours. The maps are correlated with a top-hat kernel of a width of 0.1°.

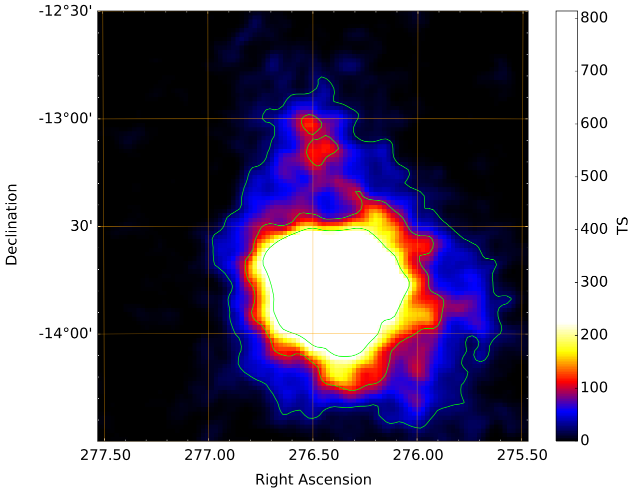

Figure 4.28: FoV TS map, calculated by using a point-like test source with fixed spectral index of 2.5. The 25, 100 and 225 TS contours, corresponding to the 5, 10, and 15σ levels are indicated in green. See text for further discussion.

ground plus test-source against the background-only hypothesis. The only free parameter of the test-source is the flux normalization. Its spectral model is given by a power law with a fixed spectral index of 2.5. By this, a TS value is calculated for each pixel. The resulting map is shown in Fig. 4.28. The overall emission morphology of the TS map is in good agreement with those of the FoV significance maps.

4.5.5 Testing for an inner source structure

To test for an inner sub-structure of the source HESS J1826-130, which is in the best-fit FoV model described by a single extended Gaussian component, slices along Right Ascension and Declination have been produced to search for obvious features not in agreement with this model. Furthermore, alternative FoV models with two-source components have been re-fit to the FoV and checked for a significant TS improvement.

Slices along R.A. and Dec.

The position for the slices along Right Ascension and Declination has been chosen to be centered on the best-fit position of HESS J1826-130, with an extension of $\pm(\sigma/2)$, where $\sigma = 0.21°$ is the best-fit width of the Gaussian model as given in Tab 4.7.

Fig. 4.29 shows the FoV count-map overlaid with the best found FoV model and the extraction region of the slices. The slices are shown in Fig. 4.30. For both slices, it is visible that the basic shape of the emission is well reproduced by the model. For the slice along Declination, the slight over-description of the model at around $-13.45°$, which was already recognized in the residual significance map discussion (cf. Sec. 4.5.3), is visible. The slices show no direct indication for an inner structure of the emission of HESS J1826-130, though somewhat larger fluctuations against the model seem to be visible in the slice along Right Ascension.

Testing extended model descriptions for HESS J1826-130

Different extensions of the single Gaussian model description of HESS J18216-130 have been tested and checked for a significant improvement of the FoV model. A brief summary is given in the following.

A first approach to add a second, independent point-source component on top of the radial Gaussian component was not successful. The fit showed an unstable behavior, not being able to place the point-source component in the central emission region of HESS J1826-130. The component runs in the spatial parameter bounds and is set to zero in terms of flux normalization.

To stabilize the fit, a composite model was used for the spatial description of HESS J1826-130. In this model description, two spatial components are bound to the same spectral component. Using a power law description and a Gaussian superimposed by a point-source component, the fit using the composite model converges. The resulting TS value is 8.7 comparing to the single Gaussian model, with the spectral indices being in agreement within the 1σ statistical error. A similar result is reached using two Gaussian components in a composite model description, with the width of one of the Gaussians fitted to a negligible value, effectively describing a point source. For the spectral assumption of a power law with exponential cutoff, the composite model of a point-source plus radial Gaussian reaches a TS of 13.4 being compared to the Gaussian-only model description.

These results can be seen as a hint to a more complex source structure which is however not clearly detectable under the given statistics in this analysis.

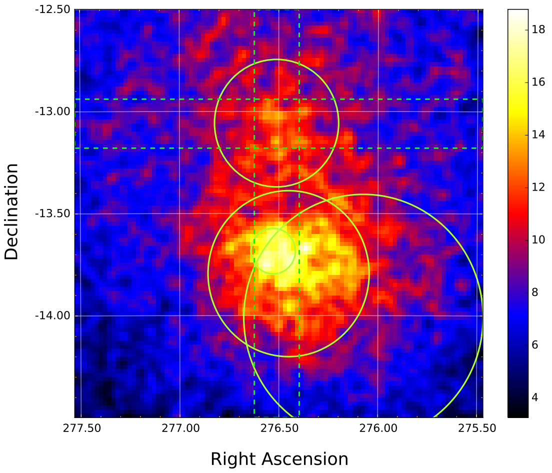

Figure 4.29: FoV countmap overlaid with the best-fit FoV model. The circles depict the 68% containment radius of the Gaussian components. The slice extraction regions are shown by green dashed lines. They are centered on the best-fit position of the HESS J1826-130 Gaussian model component.

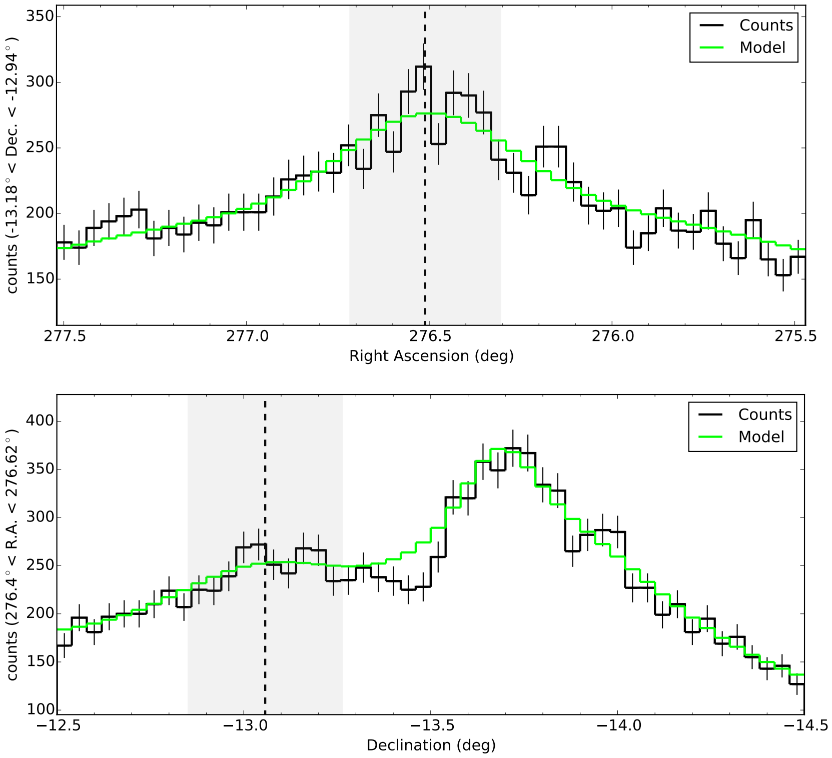

Figure 4.30: Slice plots along Right Ascension and Declination. The extraction regions of the slices are shown in Fig. 4.29. The black histogram gives the measured counts, the green one gives the model prediction. The black dashed line indicates the best-fit position of the model component of HESS J1826-130, the gray shaded band depicts its width ($\pm 1\sigma$). The basic shape of the emission is well reproduced by the model.

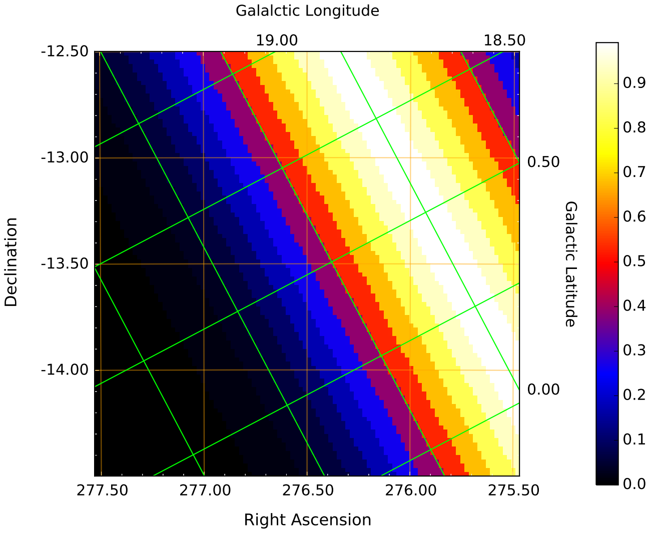

Figure 4.31: Template model component describing the VHE Galactic diffuse emission within the spatial boundaries of the FoV under investigation. The shape along Galactic latitude is assumed to follow a Gaussian with a width of 0.4°. The color scale gives the relative model intensity, normed to the maximum of the map. The Galactic coordinate system is overlaid in green. All axes are shown in units of degree.

4.5.6 Testing the influence of Galactic diffuse emission

The emission region of HESS J1826-130 is located close to the Galactic plane, its best fit position of (R.A., Dec.) $= (276.51°, -13.06°)$ corresponding to $(\lambda, \beta) = (18.44°, -0.41°)$ in Galactic coordinates λ/β = Galactic longitude/latitude. It is therefore interesting to test for a potential influence of Galactic diffuse emission, i.e. to test whether or not such a component is detectable in the given analysis. Diffuse emission along the Galactic plane was shown to be detected in the VHE range by Abramowski et al. (2014).

In a first approximation, the VHE Galactic diffuse emission can be described by a Gaussian band model

$$I(\lambda, \beta) \propto \exp\left(\frac{-\beta^2}{2\sigma_\beta^2}\right) \tag{4.6}$$

with a width of $\sigma_\beta = 0.4°$ in Galactic latitude, extending in Galactic longitude in a range of about $|\lambda| < 80°$ (cf. Mayer 2014). The spectrum of the diffuse emission is assumed to follow a power law. The spatial template map according to this model is shown in Fig. 4.31.

Including the diffuse emission component in the FoV model and carrying out a re-fit results in a poor TS improvement of 1.1, indicating that the Galactic diffuse emission cannot be detected in this analysis. Comparing the fitted model component of the diffuse emission to the background component in terms of predicted model counts per pixel, it is at a level of about 2%. The fitted peak value in terms of differential flux at 1 TeV of the component is $(1.7 \pm 1.5) \times 10^{-9}\,\mathrm{TeV^{-1}s^{-1}cm^{-2}sr^{-1}}$, which is nevertheless well comparable to the peak value of about $3 \times 10^{-9}\,\mathrm{TeV^{-1}s^{-1}cm^{-2}sr^{-1}}$ given in Abramowski et al. (2014). The spectral index of the diffuse component is found at 2.62 ± 0.86. The presented results show that the VHE Galactic diffuse emission is in a very good approximation negligible in this analysis.

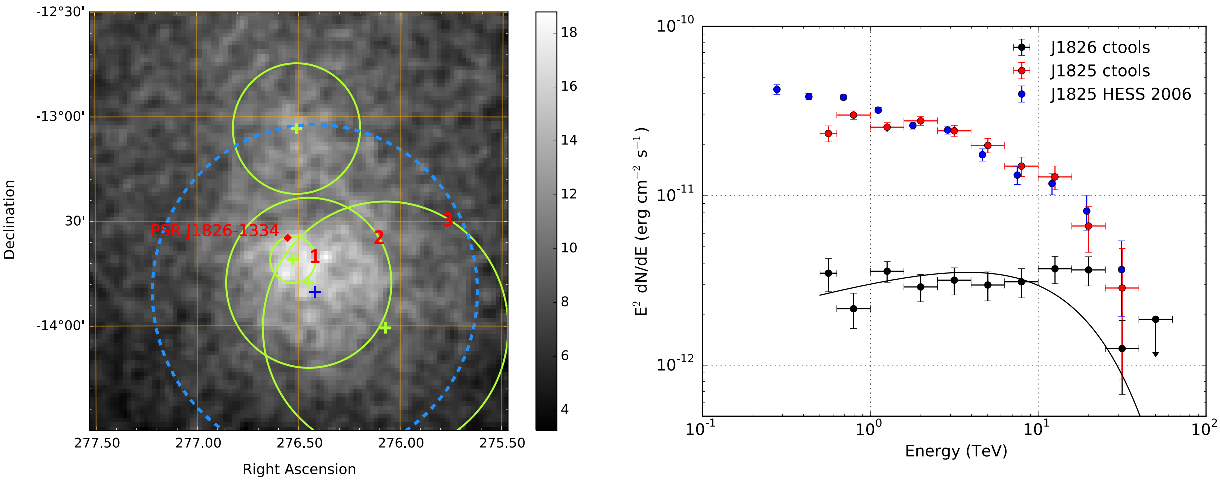

Figure 4.32: *Left:* Smoothed count-map overlaid by the ctools FoV model components, shown in green. The circles give the 68% containment radii, while the crosses depict the best fit positions of the individual components. The analysis On-region for HESS J1825-137 as used in the 2006 H.E.S.S. analysis is shown by the blue dashed line. The position of the pulsar PSR J1826-1334 is indicated. *Right:* Differential energy spectrum of HESS J1825-137 derived within the ctools analysis (red) and the H.E.S.S. analysis from 2006 (blue). The spectrum of HESS J1826-130 is shown for comparison, together with the best-fit exponential cutoff model (black line).

	Spectral index	Total flux (E > 1 TeV)
H.E.S.S. 2006	2.38 ± 0.02	14.3 ± 0.4
ctools	2.35 ± 0.05	13.1 ± 2.6

Table 4.11: Comparison of the overall emission characterization of HESS J1825-137 from the official H.E.S.S. publication from 2006 (Aharonian et al. 2006b) and the ctools analysis of this work. The total flux is given in units of $10^{-12}\,\mathrm{cm}^{-2}\mathrm{s}^{-1}$. The quoted H.E.S.S. results are given for the assumption of a power law spectrum. The ctools results are calculated as the mean value (spectral index) and the sum (total flux) of the three individual model components. See text for further discussion.

4.5.7 Verification of basic HESS J1825-137 analysis results

A comparison of the basic analysis results of the VHE emission of HESS J1825-137 from the ctools analysis to officially published H.E.S.S. results provides the opportunity to further verify the new template-fit analysis approach. Such a comparison is made in this section, referring to the H.E.S.S. analysis results as presented in Aharonian et al. 2006b. The results from the ctools analysis are given in Tab. 4.7.

The H.E.S.S. analysis from 2006 provides an overall characterization of the largely extended emission region of HESS J1825-137 by using a large integration radius of 0.8° for the analysis On-region, which in parts also covers the emission region of HESS J1826-130, see Fig. 4.32. With HESS J1825-137 being the strongly dominant source, a potential influence of HESS J1826-130 should in a frist approximation however be negligible.

The ctools analysis describes the source using three individual Gaussian components. To allow for a comparison of the overall emission characteristics, a mean spectral index is

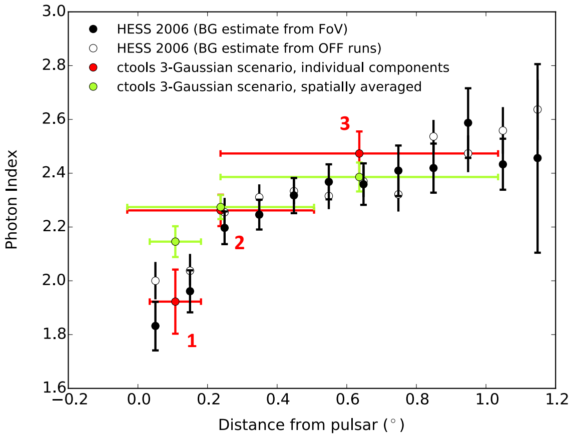

Figure 4.33: Distance from pulsar PSR J1826-1334 vs. photon index. The black/white data points are from the H.E.S.S. analysis from 2006, the red data points show the ctools result corresponding to the three individual Gaussian components as indicated in Fig. 4.32. The error bars represent the 1σ spatial width of the model components. The green data points give the mean spectral index, derived by averaging (flux-weighted) over the contributions of all three model components of the ctools analysis in the spatial regions of the individual components, respectively.

calculated by weighting with the total flux of the individual components above 1 TeV. The total source flux is calculated by taking the sum of the total flux of the three components. Tab. 4.11 summarizes the basic parameters of this characterization.

The spectral indices are in good agreement. The total flux above 1 TeV differs slightly. However, regarding the derived uncertainties, the results from the H.E.S.S. analysis and the ctools analysis are compatible.

A differential energy spectrum of HESS J1825-137 can be derived from the ctools analysis by taking the sum of the differential energy fluxes of the individual three components in the respective energy bins. The spectrum is shown in Fig. 4.32, right, together with the result from the H.E.S.S. analysis. There is a good agreement in the energy-range above 1 TeV, with increasing differences towards lower energies. This difference might be explained by the energy-dependent morphology of the source in combination with the different spatial extraction regions of the spectra. Preliminary updated analysis results on HESS J1825-137, presented by Mitchell et al. 2017, show that a restriction of the analysis region to a radius of 0.4° yields more pronounced differences in the total energy spectrum towards lower energies when being compared to the 0.8° region spectrum. Towards the highest energies, the two spectra for the different regions agree, which shows that the core region can account for the entire emission of the 0.8° region in the corresponding energy range and that potential contamination effects from HESS J1826-130 are in a very good approximation indeed negligible.

For the interpretation of the results, it is generally necessary to take into account the fact that the spatial regions from which these characterizations are derived are not exactly identical and different data sets are used for the analysis. Related systematic uncertainties are not taken into account at all. From this point of view, the agreement is at a reasonable level.

The energy-dependent morphology of the VHE emission of HESS J1825-137 was revealed by a spatially resolved spectral analysis towards the south-western direction of PSR J1826-

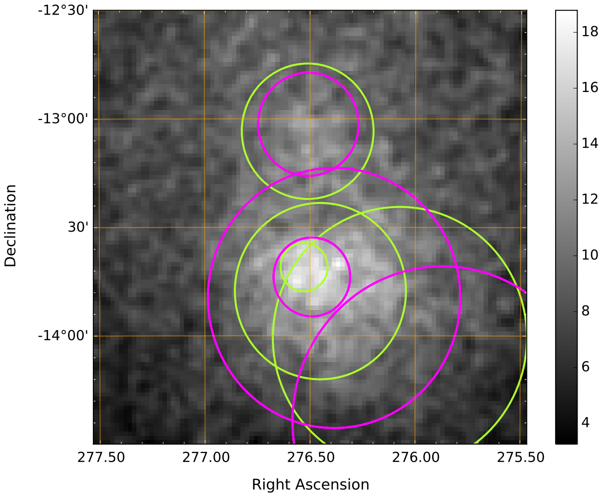

Figure 4.34: Comparison of the ctools FoV model (green) and the HGPS FoV model (magenta), overlaid on the FoV count-map of the ctools analysis. The circles depict the 68% containment radii of the individual Gaussian components.

1334. A clear increase in the spectral index for larger distances from the pulsar is observed. The three model components of the ctools analysis are also located at different distances in south-western direction to the pulsar, which allows for comparison of this effect. The dependence of the spectral index on the distance from PSR J1826-1334 is shown in Fig. 4.33. The ctools results are in good agreement with the results of the dedicated study presented in Aharonian et al. 2006b. The data points are labeled with numbers 1, 2, 3 to illustrate the corresponding model components as shown in Fig. 4.32. Referring to Tab. 4.7, these are the components 1825b, 1825 and 1825c, respectively.

4.5.8 Comparison to the HGPS FoV model

The new HGPS catalog (H.E.S.S. Collaboration et al. 2018) provides the opportunity to compare the spatial FoV model derived in this work with the FoV model derived within the HGPS analysis procedure. The HGPS also uses a multi-Gaussian approach for the spatial modeling of source regions. As at the time of writing this thesis the HGPS is still under construction without being officially published, only a qualitative comparison using preliminary results can be given. Fig. 4.34 shows the ctools FoV count-map overlaid with the two different FoV models from the ctools analysis and the HGPS analysis.

The models agree in terms of absolute number of components used to describe the sources located in the FoV: one Gaussian component to describe HESS J1826-130, three Gaussian components to describe the emission of HESS J1825-137. The width and position of the components differs slightly for HESS J1826-130, while more obvious differences are visible for the HESS J1825-137 components. These deviations should be attributable to differences in the analysis. In contrast to the ctools analysis, the spatial modeling of the HGPS is independent of any spectral assumption on the emission. Furthermore, the sky-region considered for the HGPS modeling is not restricted to the FoV of the ctools analysis but larger in total size, which might affect the modeling. Also the use of different data sets introduces systematic uncertainties. The resulting influence of such differences on a complex triple-Gaussian model as used to describe HESS J1825-137 is hard to estimate. From this point of view, the basic agreement of the FoV models is to be seen as a reasonable, satisfactory result.

4.6 Conclusion

From the analysis results of HESS J1826-130 presented in the preceding sections, the following summary and conclusions can be drawn.

The ctools template-fit analysis provides the most conclusive analysis approach to the complex FoV under investigation and is therefore expected to yield the most appropriate characterization of HESS J1826-130. The spatial as well as spectral analysis results from the standard On-Off analysis and the ctools analysis are compatible, which is to be seen as an important cross check for both analysis approaches. The reconstructed spectral flux points of the two analysis techniques agree within errors after correcting to the same solid-angle coverage. Therefore, a potential contamination effect of the analysis On-region of HESS J1826-130 by emission from the neighboring source HESS J1825-137 seems to not have as drastic effects as one might expect, cf. discussion Sec. 4.2.3.

The power law model with exponential cutoff is significantly preferred over a pure power law model (TS > 9) for the ctools analysis of data set N as well as for the On-Off analysis of data set C. The ctools analysis gives with TS $= 19.3$ (4.4σ) the strongest preference, though being based on the smaller data set. In contrast, the On-Off analysis for data set N gives a TS value of TS $= 4.3$ and thus no conclusive result. For data set C, the On-Off analysis gives a preference of TS $= 12.7$ (3.6σ). In this respect, the ctools analysis approach can also be seen as being more sensitive. As the ctools analysis confirms the preference of the cutoff power law model, the presented results are to be seen as a significant detection of a high-energy fall-off in the energy spectrum of HESS J1826-130.

The calculation of pull distributions revealed a small bias for the estimator of the cutoff energy and the spectral index for the exponential cutoff power law model, intrinsic to the fitting procedure under the given statistics. This bias can be corrected as discussed in Sec. 4.5.2. The best-fit model description found in the ctools analysis including this bias-correction is summarized in Tab. 4.12.

Spectral index	1.80 ± 0.13
E_{cut} [TeV]	18.0 ± 4.6
Flux normalization [$10^{-12}\,\mathrm{s}^{-1}\mathrm{cm}^{-2}\mathrm{TeV}^{-1}$]	2.02 ± 0.27
Flux $> 1\,\mathrm{TeV}$ [$10^{-12}\,\mathrm{s}^{-1}\mathrm{cm}^{-2}$]	1.94 ± 0.35
R.A. [deg.]	276.51 ± 0.02
Dec. [deg.]	-13.06 ± 0.02
Width (σ) [deg.]	0.21 ± 0.02

Table 4.12: Resulting best-fit model characterization of HESS J1826-130, derived within the ctools analysis. For the cutoff energy and the spectral index, bias-corrected values are given. The flux normalization is given at an energy of 1 TeV. See text for further discussion.

Taking the ctools analysis result as reference, the cutoff energy is $E_{cut} = 18.0 \pm 4.6\,\mathrm{TeV}$. Assuming that the exponential cutoff power law model gives an appropriate description of the source spectrum, this result strongly disfavors the PeVatron hypothesis, as it indicates a cutoff in the parent particle spectrum at hundreds of TeV, likely not reaching the PeV energy range without strong attenuations. This aspect will be discussed in more detail in chapter 5, presenting a basic modeling of the TeV emission of HESS J1826-130.

More complex alternative spectral models allowing for a curvature in the spectrum towards the highest energies like a broken power-law or log-parabola model have not been tested. Such advanced alternative spectral shapes might result in competitive descriptions of the differential energy spectrum of HESS J1826-130.

A detailed study of systematic reconstruction uncertainties related to the ctools analysis approach, e.g. connected to IRF export precision, was beyond the scope of this thesis. However, studies about such systematics are of importance for the future development of the template-fit analysis approach in order to further improve a comprehensive understanding of this new analysis technique and are an ongoing effort in the H.E.S.S. Collaboration. Recent results imply systematic uncertainties of about 20% to 30% concerning spectral reconstruction.

5 Modeling the VHE emission from HESS J1826-130

After having derived a morphological and spectral characterization of the non-thermal VHE emission of HESS J1826-130, this chapter focuses on the question of the origin of this emission and potential conclusions which can be drawn about the underlying parent particle distribution and related astrophysical processes. A brief overview of the MWL surrounding of the source is given at the beginning of this chapter. The derived VHE differential energy spectrum is used for a basic modeling of the observed emission. For this purpose, the `naima`[1] software package is used. Under the assumption of a homogeneous parent particle distribution, the γ-ray emission resulting from leptonic or hadronic particle interaction processes is calculated. The spectral shape of the parent particle distribution is predefined by a given spectral model, e.g. a power law spectrum. Using Markov-Chain Monte Carlo (MCMC) sampling, `naima` allows one to fit such a model to an observed source spectrum. For a detailed description of the `naima` software, see Zabalza (2015); Foreman-Mackey et al. (2013).

5.1 Motivation

A detailed discussion of the MWL surrounding of the source region of HESS J1826-130 is given in Sec. 4.1.3, together with a summary of ISM gas studies. An illustrating overview including the results from the ctools analysis is given by Figs. 5.1 and 5.2, which show the MWL picture of the region and information about the ISM matter distribution gained from gas studies overlaid on the FoV TS map.

In Fig. 5.1, it is visible that the entire ASCA X-ray emission region, including the radio-quiet pulsar PSR J1826-1256, is well located within the emission (best-fit model) region of HESS J1826-130. The location of the pulsar seems slightly shifted towards the northern direction with respect to the peak regions in the TS map. The positional coincidence gives rise to the assumption that the observed TeV emission might be of leptonic origin, i.e. a pulsar wind nebula, powered by PSR J1826-1256.

From Fig. 5.2, it is visible that none of the very dense molecular clump cores as detected by Voisin et al. (2016) is directly coincident with the TS peaks in the emission region of HESS J1826-130. However, the red circle which depicts the core region of the molecular cloud, whose average density has been estimated to be $n_{\mathrm{H}} = 6.1 \times 10^{2}\,\mathrm{cm}^{-3}$, overlaps the emission region in large parts. The overall spatial match between dense molecular clouds and the emission region of HESS J1826-130 can be seen as support of a hadronic emission scenario and made HESS J1826-130 a PeVatron candidate.

---

[1] http://naima.readthedocs.org

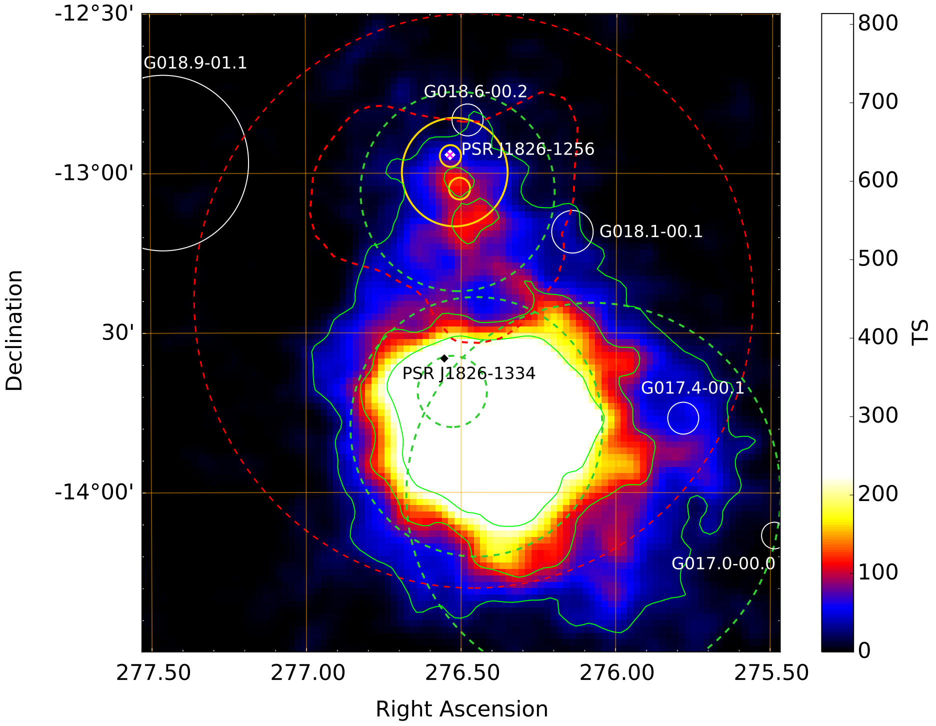

Figure 5.1: FoV TS map of the ctools analysis overlaid with the MWL source surrounding. The green lines indicate the 25, 100 and 225 TS contour levels. The green dashed lines depict the 68% containment radii of the Gaussian components from the ctools FoV model. The yellow lines show the ASCA X-ray emission regions from Roberts et al. (2001). The 95% confidence region of the position of 3EG J1825-1302 is shown by the inner red dashed contour line. The white diamond marks the location of the radio-quiet Fermi pulsar PSR J1826-1256, whose position matches the one of the Eel Nebula observed by Chandra (marked with a magenta cross). The dashed red circle depicts the spectral extraction region of 2HWC J1825-134, as given in Abeysekara et al. (2017).

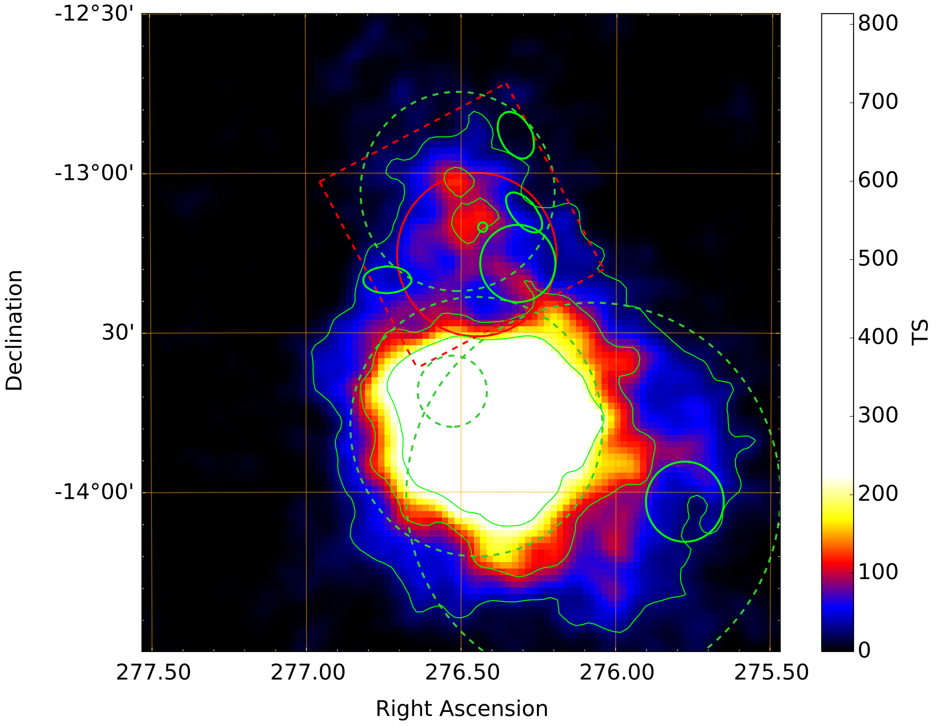

Figure 5.2: Same as Fig. 5.1, but overlaid with regions derived from ISM gas studies. The red dashed box shows the 7 mm Mopra survey region from Voisin et al. (2016), cf. Sec. 4.1.3. The thick green contours depict dense clumps of molecular matter. The red circle depicts the core region of the molecular cloud north to HESS J1825-137, whose mass and density has been estimated.

5.2 Hadronic emission scenario

For the modeling of the hadronic emission scenario, the following assumptions are made: The parent particle distribution is composed of protons, with a differential energy spectrum following a power law with exponential cutoff. This model is motivated by the observation of a cutoff in the γ-ray spectrum. For the parameters describing the ambient molecular matter, the estimates derived by Voisin et al. 2016 for the central molecular cloud region towards HESS J1826-130 (red circle, Fig. 5.2) are used: a density value of $n_\mathrm{H} = 6.1 \times 10^2\,\mathrm{cm}^{-3}$ and a line-of-sight distance of the system of $\mathrm{d} = 4\,\mathrm{kpc}$.

The MCMC sampling provides estimates for the free model parameters by recovering the respective posterior distributions. The free parameters are the spectral index, cutoff energy and normalization of the exponential cutoff power law describing the proton energy spectrum. Additionally, an estimate of the total energy requirement W_p is derived by integrating over the proton spectrum above an energy of 1 GeV.

For each of the fitted parameters, a prior distribution is required for the MCMC sampling. The following priors are used: A uniform distribution in the range $[0, \infty]$ for the normalization. For the spectral index, a uniform prior distribution in the range $[-1, 8]$. The cutoff energy is sampled in logarithmic space, i.e. the fitted parameter is $\log_{10}(E_{cut,p})$. Also for this variable, a uniform distribution in the range $[0, \infty]$ is set as prior distribution. This choice of flat prior distributions is made to prevent any artificial bias which might be introduced by the usage of constraining prior functions. The MCMC sampling specifications are: 128 walkers, running 1000 burn-in steps and 1000 sampling runs.

The resulting posterior distributions are shown in Fig. 5.3. The best-fit parameter values are defined as the median of the distribution, respectively, while the 16% and 84% quantiles are used to define the 1σ errors in lower and upper direction, respectively. The derived best-fit MCMC sampling values are

- Spectral index : $1.69^{+0.22}_{-0.27}$
- Cutoff energy : 200^{+224}_{-87} TeV
- Normalization ($E_p = 1\,\mathrm{TeV}$) : 8^{+7}_{-4} $10^{33}\,\mathrm{eV}^{-1}$
- Total Energy $W_p(E_p > 1\,\mathrm{GeV})$: $1.9^{+1.0}_{-0.4}$ $10^{47}\,\mathrm{erg}$

The fitted spectral index is $1.69^{+0.22}_{-0.27}$, which mirrors the exceptional hardness of the measured TeV emission. The value is well compatible with the one derived for the γ-ray spectrum of 1.80 ± 0.13 (cf. discussion about parent particle distributions Sec. 2.2.1).

The cutoff energy is found at 200^{+224}_{-87} TeV, which is also compatible with the expectation from the cutoff energy reconstructed in the γ-ray analysis. The best fit value of 200 TeV (median of the posterior distribution) is located clearly below the PeV range. For this value, the PeVatron hypothesis would, under the assumption of a stationary modeling scenario neglecting propagation effects, not hold. Fig. 5.4 shows the best-fit parent proton spectrum and the resulting γ-ray spectrum together with the spectral flux points from the ctools analysis to which the model was fit. The 1σ and 3σ confidence bands are indicated, respectively. The strong suppression in the PeV regime also holds regarding the 1σ confidence band, cf. Fig. 5.4 left. The 95% confidence level upper limit of the cutoff energy, derived from the posterior distribution, is found at $\mathrm{UL}_{95} = 955\,\mathrm{TeV}$. The presented results show that energies of hundreds of TeV are reached in the present-age parent proton spectrum, while with high probability, a strong attenuation has already set

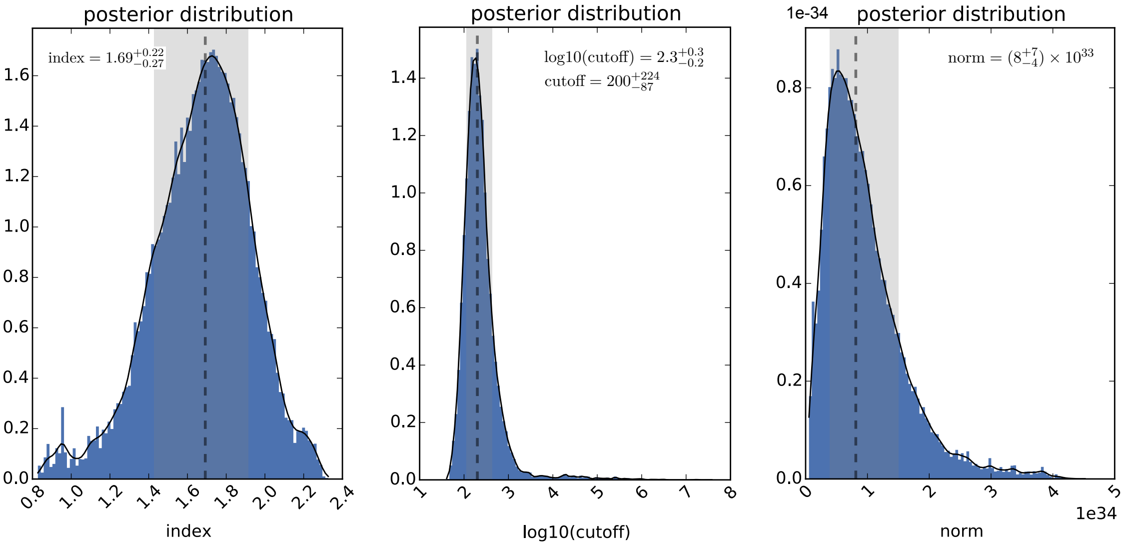

Figure 5.3: Posterior distributions of the parameters spectral index (left), cutoff energy (middle, unit = TeV) and normalization (right, unit = eV^{-1}), derived via MCMC sampling. The best-fit values are indicated by black dashed lines and refer to the median of the respective distribution. The errors refer to the 16% and 84% quantiles, used to define the 1σ confidence interval shown as gray shaded band. See text for further discussion.

in when reaching the PeV energy range. Accordingly, the PeVatron hypothesis is, in the context of a stationary modeling approach, strongly disfavored by the shown results.

The situation is further illustrated in Fig. 5.5, showing the best-fit model proton spectrum in comparison to proton spectra of same spectral index but different cutoff energies. A clear evidence of a PeVatron would be given for cutoff energies $E_{cut,p} \geq 3\,\mathrm{PeV}$. The resulting γ-ray spectra are shown on the right hand side, again together with the spectral flux points from the ctools analysis.

Regarding a typical supernova explosion energy of about $10^{51}\,\mathrm{erg}$, the requirement of $W_p(E_p > 1\,\mathrm{GeV}) = 1.9^{+1.0}_{-0.4} \times 10^{47}\,\mathrm{erg}$ is well within the energy budget that could have been delivered by a single supernova explosion, assuming a generic value of 10% efficiency for CR acceleration. A local particle accelerator is needed to produce a local CR excess, as the observed emission cannot be explained by interactions of the molecular matter with the sea of CRs (Galactic plane averaged density $w_{CR} \sim 1\,\mathrm{eV\,cm^{-3}}$), which would produce a total γ-ray flux of about $F(> 1\,\mathrm{TeV}) = 5.8 \times 10^{-14}\,\mathrm{ph\,cm^{-2}\,s^{-1}}$ for the molecular cloud of total mass $\mathrm{M_{H_2}} = 3.3 \times 10^5\,\mathrm{M_\odot}$ (cf. Sec. 4.1.3, Voisin et al. 2016). This value is about 30 times below the observed one.

Voisin et al. (2016) conclude that the progenitor SNR of HESS J1825-137, located at a line-of-sight distance of about 3.9 kpc, is a suitable candidate which might contribute to the observed TeV emission. In this scenario, the γ-ray excess would be produced in the complex interaction region of an evolved SNR shell which crashed into dense molecular matter, leading to a strongly asymmetrical evolution of the overall system. Not much is known about the progenitor SNR of HESS J1825-137. The observation of an Hα-rim at a distance of about 120 pc ($\sim 1.7°$) in eastern direction of PSR J1826-1334 might be interpreted as its outer shock region. The lack of this Hα rim in northern direction of HESS J1825-137 may arise due to shielding effects of the dense molecular material, which

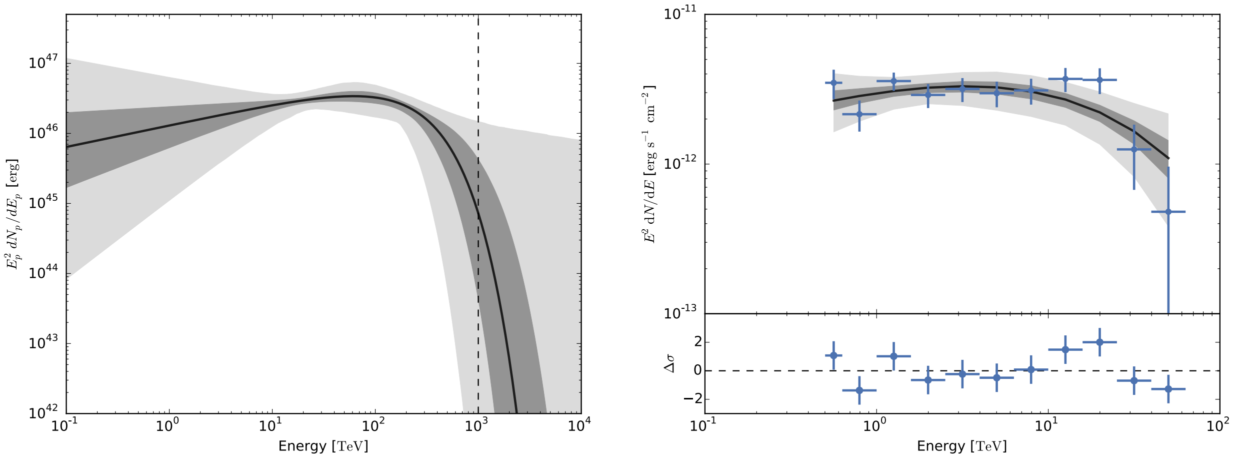

Figure 5.4: Best-fit proton spectrum (left) and resulting γ-ray spectrum (right), together with the VHE flux points derived in the ctools analysis. The dark gray (light gray) shaded region depicts the 1σ (3σ) confidence band, respectively. The beginning of the PeV range is indicated by the black dashed line.

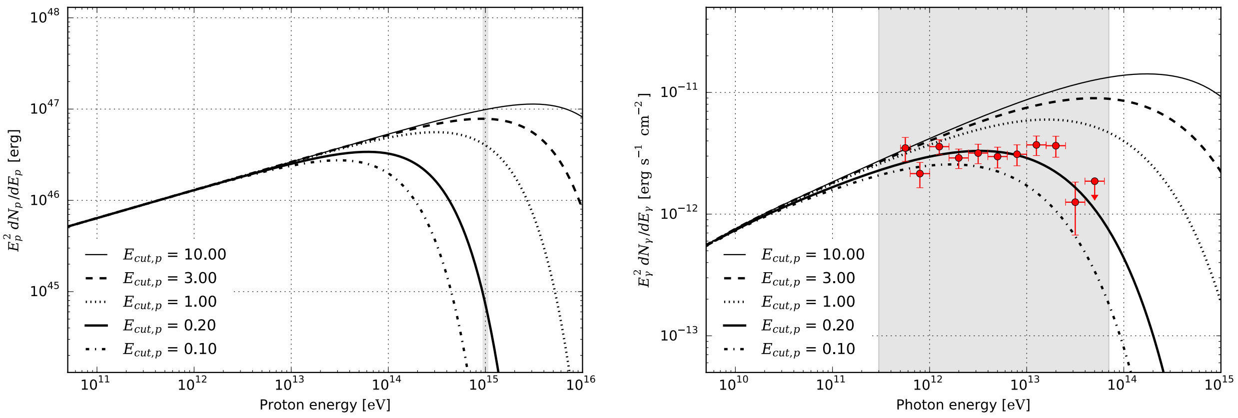

Figure 5.5: Proton spectra (left) and resulting γ-ray spectra for different cutoff energies in the parent proton distribution $E_{cut,p}$. The thick solid line corresponds to the best-fit model. The red data points are the VHE flux points derived in the ctools analysis, shown for comparison. The gray shaded band depicts the typical energy range accessible for H.E.S.S. observations in CT1-4 observation mode, targeted by this analysis.

might be connected to the observed γ-ray emission of HESS J1826-130 as well as the crashed PWN seen in TeV energies. For a more detailed discussion, see Voisin et al. (2016). In such a shell-cloud interaction scenario, the spectrum of the observed TeV emission would strongly depend on the exact environmental conditions and the resulting evolution of the system.

The SNR G018.6-00.2 is located within the 68% containment radius of the HESS J1826-130 model description, though much smaller in size. Its estimated line-of-sight distance is $4-5.2$ kpc (Johanson & Kerton 2009). SNR G018.1-00.1 is located at the edge of the 68% containment contour, with a distance estimate of $4-6.3$ kpc and an age of $4800-5800$

years[2]. Also these two SNRs might be associated with the TeV emission of HESS J1826-130.

For these objects, the scenario of runaway CRs illuminating a molecular cloud at a certain distance d away from their own position requires a more refined modeling approach than presented in this work, taking into account propagation effects and the dynamical evolution of an SNR to allow for conclusions about the maximum acceleration energy reached in these systems. The energy dependence of the CR diffusion coefficient is usually assumed to follow a power law $D(E) = D_{10} \times (E/10\,\mathrm{GeV})^{\delta}$, with a commonly proposed value of $D_{10} = 10^{28}\,\mathrm{cm}^2/\mathrm{s} = 0.03\,\mathrm{pc}^2/\mathrm{yr}$ and $\delta \sim 0.3-0.6$ (e.g. Aharonian & Atoyan 1996). Taking $\delta = 0.5$, one extrapolates to a diffusion coefficient of $D_{100} = 3\,\mathrm{pc}^2/\mathrm{yr}$ for 100 TeV protons. For a line-of-sight distance of 4 kpc, an angular distance θ between two objects corresponds to about $(\theta/1^\circ) \times 70\,\mathrm{pc}$. This relates to an estimated diffusion timescale of 100 TeV protons of $t = d^2/(2D_{100}) \approx 812\,(\theta/1^\circ)^2$ years. The angular distance of G018.6-00.2 and G018.1-00.1 to the best-fit position of HESS J1826-130 are 0.23° and 0.38°, respectively. This relates to timescales of $t_{\mathrm{G18.6}} = 43$ years and $t_{\mathrm{G18.1}} = 117$ years, which is very small compared to an age estimate of about 5000 years of G018.1-00.1. However, especially for dense environments, much smaller values of D_{10} down to $D_{10} \sim 10^{26}\,\mathrm{cm}^2/\mathrm{s}$ cannot be excluded (Aharonian & Atoyan 1996). Taking $D_{10} = 2.1 \times 10^{26}\,\mathrm{cm}^2/\mathrm{s}$ results in diffusion timescales of $t'_{\mathrm{G18.6}} = 1830$ years and $t'_{\mathrm{G18.1}} = 5000$ years, in agreement with the age estimate of G018.1-00.1. For G018.6-00.2, no age estimate was derived so far.

The search for Galactic CR PeVatrons via a delayed γ-ray signal caused by runaway CRs illuminating molecular clouds in their near vicinity was e.g. suggested by Gabici & Aharonian (2007). The VHE γ-ray spectrum of HESS J1826-130 measured with the H.E.S.S. instrument leaves room for such a hypothesis and might be used for further advanced modeling studies.

Result stability, influence of high-energy interaction models

The above quoted 95% confidence level (C.L.) upper limit of the cutoff energy of 955 TeV is derived as the 95% quantile of the posterior distribution of the cutoff energy. As this quantile is located in the upper tail of the distribution, it might be affected by statistical fluctuations intrinsic to the set MC statistics. To test for this influence, the MCMC sampling was repeated with the same settings as explained above for a set of 20 iterations. This set of 20 MCMC iterations provides a sample of 20 measures for each of the fitted parameters and the upper limit of the cutoff energy.

The resulting distributions of those 20 measures for each of the quantities are shown in Fig. 5.6. The plotted statistical errors of the spectral index, normalization and cutoff energy relate to the 16% and 84% quantiles of the posterior distribution, while the best fit value is defined by taking the median, as explained above. For all of the fit parameters, it is visible that the spread due to limited MC statistics is negligible compared to the statistical error. For example, the spread of the cutoff energy within these 20 iterations accounts to 6 TeV, calculated by taking the sample standard deviation of the 20 median estimates. In contrast, the mean statistical upper and lower error, calculated as the mean value of the upper and lower errors from this set of 20 iterations, are 217 and 86 TeV, respectively. Thus, a new estimate for the cutoff energy is given by taking these mean values: $E_{cut} = 200^{+217}_{-86}$ TeV. Analogously, new estimates for the spectral index and the normalization can be defined by taking the respective mean values. These improved

---

[2] http://www.physics.umanitoba.ca/snr/SNRcat/

estimates are given by

- Normalization ($E_p = 1\,\mathrm{TeV}$) : $8\,(^{+7}_{-4})_{\mathrm{stat}}$ $10^{33}\,\mathrm{eV}^{-1}$
- Spectral index : $1.69\,(^{+0.22}_{-0.27})_{\mathrm{stat}}$
- Cutoff energy : $200\,(^{+217}_{-86})_{\mathrm{stat}}$ TeV

and are essentially identical to the values quoted above for one single MCMC run.

As expected, the influence of limited MC statistics is however more pronounced regarding the 95% C.L. upper limit of the cutoff energy (Fig. 5.6, bottom panel). The mean value of the 20 samples is 863 TeV, the width of the distribution is $\sigma_{\mathrm{stat,MC}} = 87\,\mathrm{TeV}$. This result introduces a new estimate on the 95% C.L. upper limit for the cutoff energy of

- UL_{95} : $863 \pm 19_{\mathrm{stat,MC}}$ TeV

where the error on the mean is calculated as $\sigma_{\mathrm{stat,MC}}/\sqrt{20}$.

An additional influence which needs to be considered in the context of result stability is the fact that the parametrization of γ-ray production cross sections for inelastic proton-proton interactions are based on high-energy interaction models to extrapolate to the highest energies. The `naima` package uses the parametrization of γ-ray production rates as provided by Kafexhiu et al. (2014), which are derived for the four different interaction models Pythia8, Geant4, SIBYLL and QGSJET. The default model of `naima` is Pythia8, for which all above shown results have been derived. A systematic uncertainty for each of the estimated quantities can be derived by comparing the results from these four different interaction models.

For this purpose, a set of 20 MCMC runs with identical settings is generated for each interaction model and the final estimates are computed by calculating mean values from this set of 20 iterations, as described above for the Pythia8 sample. Exemplarily, Fig. 5.7 shows the comparison for the upper limit estimate of the cutoff energy for the different models. A clear systematic difference is observable, with a tendency to smaller upper limit estimates for the SIBYLL and QGSJET models compared to the Pythia8 result. The spread of the values, calculated via the sample standard deviation is $\hat{\sigma}_{\mathrm{UL95}} = 121\,\mathrm{TeV}$. A conservative systematic error on the Pythia8 model upper limit estimate is introduced by defining this systematic error as the difference in the Pythia8 result to that one of the alternative model for which this difference is at a maximum. For the cutoff energy upper limit estimate, this maximum difference is observed between the Pythia8 and SIBYLL model results and is $\sigma_{\mathrm{sys}} = (863 - 614)\,\mathrm{TeV} = 249\,\mathrm{TeV}$.

In the same way, systematic errors for all fit-quantities can be calculated. The following summary gives an overview of the final parameter estimates for the Pythia8 model including these systematic errors:

- Normalization ($E_p = 1\,\mathrm{TeV}$) : $8\,(^{+7}_{-4})_{\mathrm{stat}} \pm 2_{\mathrm{sys}}$ $10^{33}\,\mathrm{eV}^{-1}$
- Spectral index : $1.69\,(^{+0.22}_{-0.27})_{\mathrm{stat}} \pm 0.08_{\mathrm{sys}}$
- Cutoff energy : $200\,(^{+217}_{-86})_{\mathrm{stat}} \pm 42_{\mathrm{sys}}$ TeV
- UL_{95} : $863 \pm 19_{\mathrm{stat,MC}} \pm 249_{\mathrm{sys}}$ TeV

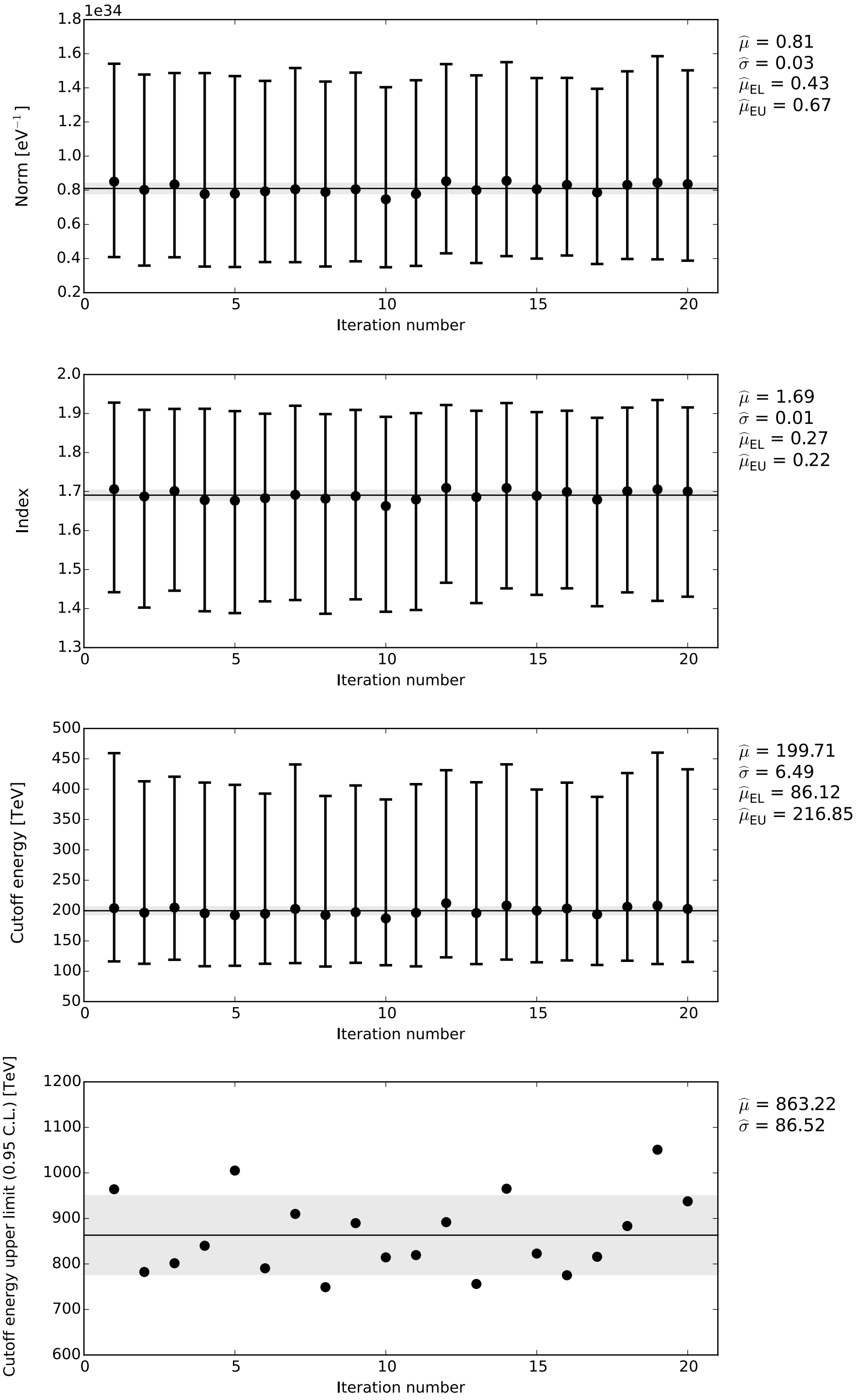

Figure 5.6: Resulting best-fit parameter estimates from a set of 20 MCMC iterations. The mean value $\hat{\mu}$ and the spread $\hat{\sigma}$ (sample standard deviation) of the values are indicated on the right hand side of the figures, together with the mean of the errors in lower and upper direction ($\hat{\mu}_{\mathrm{EL}}$, $\hat{\mu}_{\mathrm{EU}}$). The bottom panel shows the distribution of the 95% C.L. upper limit estimate on the cutoff energy. The solid line indicates the position of the mean $\hat{\mu}$, while the gray dashed band indicates the $\pm 1\hat{\sigma}$ deviation from the mean.

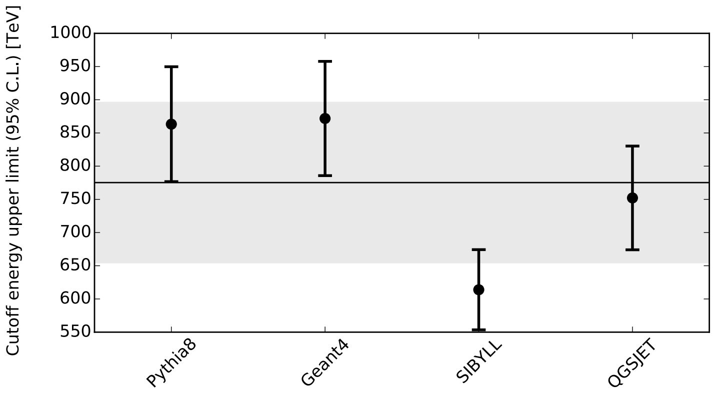

Figure 5.7: Comparison of upper limit estimates on the cutoff energy for different high-energy interaction models. The mean value $\hat{\mu}_{\mathrm{UL95}} = 775\,\mathrm{TeV}$ is indicated by the black solid line. The gray shaded band indicates the $\pm 1\sigma$ deviation from the mean, calculated via the sample standard deviation: $\hat{\sigma}_{\mathrm{UL95}} = 121\,\mathrm{TeV}$.

The strongest systematic influence is observed for the upper limit estimate on the cutoff energy, while for the other parameters, the systematic uncertainties are clearly smaller than the statistical ones.

In summary, the final parameter estimates agree well with the outcome of the first single MCMC run and do not affect the discussion or the conclusions made above concerning the hadronic emission scenario.

5.3 Leptonic emission scenario

The modeling of a leptonic emission scenario is motivated by the presence of the radio-quiet pulsar PSR J1826-1256 located at an angle of about 0.12° from the best-fit model position of HESS J1826-130. Since no reliable line-of-sight distance estimate is available for this pulsar, a generic value of 5.1 kpc is assumed, corresponding to the mean distance of the so far observed TeV emitting PWN systems (H.E.S.S. Collaboration et al. 2017). The parent particle electron spectrum is assumed to follow a power law with exponential cutoff. The existence of three primary photon fields is assumed: CMB, thermal IR (dust) and starlight. The interstellar radiation mapcube of the GALPROP CR propagation suite (Strong et al. 2009) is used to derive an estimate of the radiation fields at the Galactic radius corresponding to the position of PSR J1826-1256. A distance of 5.1 kpc in the direction of the pulsar corresponds to a Galactic radius of 3.8 kpc. The peaks in the SED of the photon fields correspond to a black body temperature of $T \sim 32\,\mathrm{K}$ with a density of $\sim 0.51\,\mathrm{eV\,cm^{-3}}$ (IR) and $T \sim 4590\,\mathrm{K}$ with a density of $\sim 2.11\,\mathrm{eV\,cm^{-3}}$ (stellar).

The fitted parameters are the normalization, spectral index and cutoff energy of the electron spectrum. The cutoff energy is again sampled in logarithmic space, i.e. the fitted parameter is $\log_{10}(E_{cut,e})$. The same sampling specifications as for the hadronic modeling are used: 128 walkers, running 1000 burn-in steps and 1000 sampling runs.

Running the MCMC sampling with the same flat, non-constraining prior distributions as used for the hadronic modeling results in the problem that some of the walkers get bound in a local maximum. For this local maximum, the cutoff energy diverges and the power

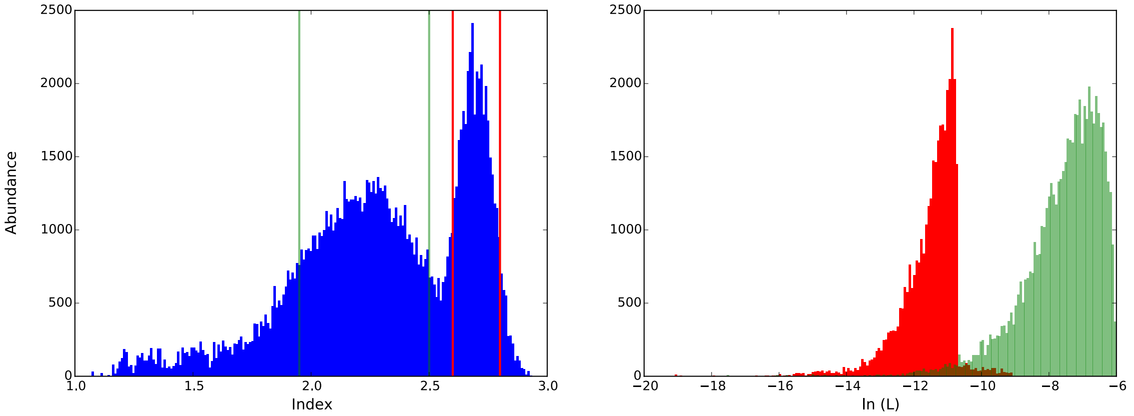

Figure 5.8: Posterior distribution of the spectral index (left) for the MCMC sampling carried out with flat, non-constraining prior distributions for all sampled parameters. The bimodal shape is caused by a secondary local maximum, which is clearly visible in the distribution of the likelihood values ln(L) shown on the right. The corresponding ranges from which the likelihood distributions were extracted are indicated by vertical lines of same color in the index distribution.

law with exponential cutoff is effectively replaced by a pure power law model. This finding is illustrated in Fig. 5.8, showing the posterior distribution of the spectral index on the left hand side. Its bimodal shape is explained by the two dominant peaks corresponding to the global maximum (left peak, smaller absolute values) and the local maximum (right peak, larger absolute values). The right hand side gives the distribution of the corresponding likelihood values, separated according to the samples belonging to the two peak regions as indicated. It confirms the right peak of the index distribution corresponding to samples of a local minimum, as their likelihood distribution peaks on a smaller value than that one of the samples from the global maximum.

To circumvent this problem, slightly constraining priors are set on the cutoff parameter $\log_{10}(E_{cut,e})$ by using a Gaussian distribution with a mean of 2.0 and a width of 2.0 and on the spectral index by using a Gaussian distribution with a mean of 2.0 and a width of 0.8. For the normalization, a flat prior distribution in the range $[0, \infty]$ is used, as before.

The resulting posterior distributions for these settings are shown in Fig. 5.9. Figure 5.10 shows the resulting best-fit electron spectrum and γ-ray spectrum together with the H.E.S.S. flux points. The derived best-fit MCMC sampling values are

- Spectral index :	$2.19^{+0.25}_{-0.31}$	
- Cutoff energy :	68^{+68}_{-27}	TeV
- Normalization ($E_e = 1\,\mathrm{TeV}$) :	4^{+3}_{-2}	$10^{34}\,\mathrm{eV}^{-1}$
- Total Energy $W_e(E_e > 1\,\mathrm{GeV})$:	$1.2^{+4.3}_{-0.9}$	$10^{48}\,\mathrm{erg}$

The fitted spectral index of the present-age particle distribution is $2.19^{+0.25}_{-0.31}$. This value yields an expected γ-ray index of $(2.19 + 1)/2 = 1.60$ (resulting IC power-law index, cf. Sec. 2.2.1), which is slightly smaller than the photon index derived in the γ-ray analysis of 1.80 ± 0.13. Yet, the values are well compatible within errors. The derived spectral index however does not allow to directly draw conclusions about the spectral shape of the initial source spectrum, as for an evolving PWN system, the initial electron source

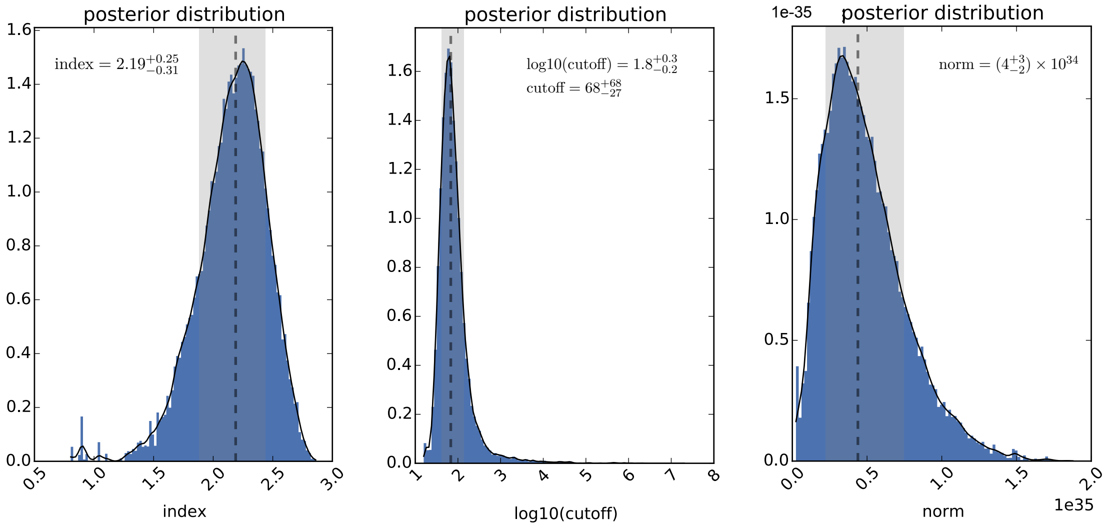

Figure 5.9: Posterior distributions of the parameters spectral index (left), cutoff energy (middle, unit = TeV) and normalization (right, unit = eV^{-1}), derived via MCMC sampling. The best-fit values are indicated by black dashed lines and refer to the median of the respective distribution. The errors refer to the 16% and 84% quantiles, used to define the 1σ confidence interval shown as gray shaded band. See text for further discussion.

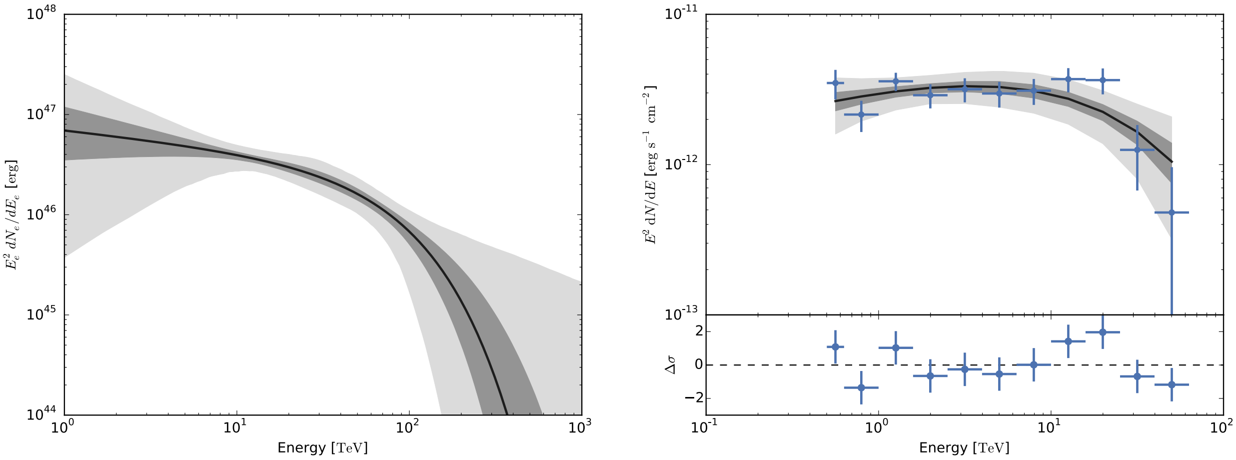

Figure 5.10: Best-fit electron spectrum (left) and resulting γ-ray spectrum (right), together with the VHE flux points derived in the ctools analysis. The dark gray (light gray) shaded region depicts the 1σ (3σ) confidence band, respectively.

spectrum will be strongly altered by related energy-loss mechanisms. A more refined, time-dependent modeling as e.g. presented in H.E.S.S. Collaboration et al. (2017), A.1.-A.6., would be required to allow such conclusions. The best-fit cutoff energy of 68^{+68}_{-27} TeV hints to a suppression of the spectrum setting in at around 100 TeV, cf. Fig. 5.10.

For the interpretation of these results, one should however take into account that the set prior distributions, though being not strongly constraining around the derived best-fit results, affect the outcome of the sampling. Decreasing the influence of the prior distributions in terms of increasing their width results in first tendency in an increase in the error estimates of the parameters, while the best-fit values (medians of the respective

$\lg(\dot{E})$	τ_c [kyr]	d [kpc]	PSR offset [pc]	Γ	$\mathrm{R_{PWN}}$ [pc]	$L_{1-10\,\mathrm{TeV}}$ [$10^{33}\,\mathrm{erg\,s^{-1}}$]	S [$10^{30}\,\mathrm{erg\,pc^{-2}\,s^{-1}}$]
36.56	14.4	5.1	10.7 ± 1.8	1.80 ± 0.13	18.7 ± 1.8	23.5 ± 4.9	5.4 ± 1.5

Table 5.1: Characteristic PWN system parameters assuming a connection of PSR J1826-1256 to HESS J1826-130. $\lg(\dot{E})$ gives the current spin-down power of the pulsar in units of $\log_{10}(\dot{E}/\mathrm{erg\,s^{-1}})$, τ_c its characteristic age, d is the assumed pulsar distance. Γ is the spectral index of the TeV source, $\mathrm{R_{PWN}}$ is the 1-sigma Gaussian extension, $L_{1-10\mathrm{TeV}}$ the TeV luminosity and S the corresponding surface brightness. All quantities are calculated according to the definitions as given in H.E.S.S. Collaboration et al. (2017). The PSR offset and the TeV source extension in units of degree are 0.12 ± 0.02 and 0.21 ± 0.02, respectively.

posterior distributions) stay constant.

The total energy requirement is $W_e(E_e > 1\,\mathrm{GeV}) = 1.2^{+4.3}_{-0.9} \times 10^{48}\,\mathrm{erg}$. To calculate the total energy released so far by the pulsar, assumptions about its initial spin-down power $\dot{E}_0$, spin-down time-scale τ_0 and the braking index n need to be made. The assumptions of $\dot{E}_0 = 2 \times 10^{39}\,\mathrm{erg\,s^{-1}}$, $\tau_0 = 0.5\,\mathrm{kyr}$ and $n = 3$, which lie within the typically considered parameter ranges, are used and refer to the parameters of a characteristic baseline model for TeV emitting PWN systems (see H.E.S.S. Collaboration et al. 2017, baseline model). This results in an energy release of $E_{rel} = 3 \times 10^{49}$ erg for PSR J1826-1256, which translates to a required conversion efficiency of about 4% against the present-age particle spectrum.

Classification parameters according to the H.E.S.S. TeV PWN population study

The H.E.S.S. Collaboration recently published a detailed study about the population of TeV pulsar wind nebulae in the H.E.S.S. Galactic plane survey (H.E.S.S. Collaboration et al. 2017). Therein, the PWN candidate systems are characterized based on observational quantities such as offset between pulsar and TeV nebula or TeV luminosity versus current pulsar spin-down power. These quantities can be calculated for HESS J1826-130 in relation to PSR J1826-1256. For this purpose, it is again assumed that the system is located at a line-of-sight distance of 5.1 kpc, which is the mean distance of TeV emitting PWN systems from the H.E.S.S. study.

The resulting quantities are summarized in Tab. 5.1 and can directly be compared to those from the H.E.S.S. population study, in which four rating criteria have been applied to PWN candidates. This rating "evaluates the plausibility of a PWN candidate by how normal the TeV properties of the PWN candidates are" (H.E.S.S. Collaboration et al. 2017), based on observations of firmly identified systems and a model describing the evolution of a PWN system. The rating criteria concern PWN containment ratio (PSR offset < 1.5 extension radii), the TeV extension versus age, TeV luminosity versus pulsar spin-down power and surface brightness versus pulsar spin-down power (for details, see H.E.S.S. Collaboration et al. 2017, Sec. 6). Applying these rating criteria to the system of HESS J1826-130 and PSR J1826-1256 (under the assumption of $d = 5.1\,\mathrm{kpc}$), it passes all of them. To further illustrate the characteristics of the potential PWN system in comparison to the entire population of TeV emitting PWN systems from the H.E.S.S. study, Fig. 5.11 shows the respective population plots with its position marked by a green diamond.

The apparent TeV efficiency is another measure to evaluate the energy requirement based

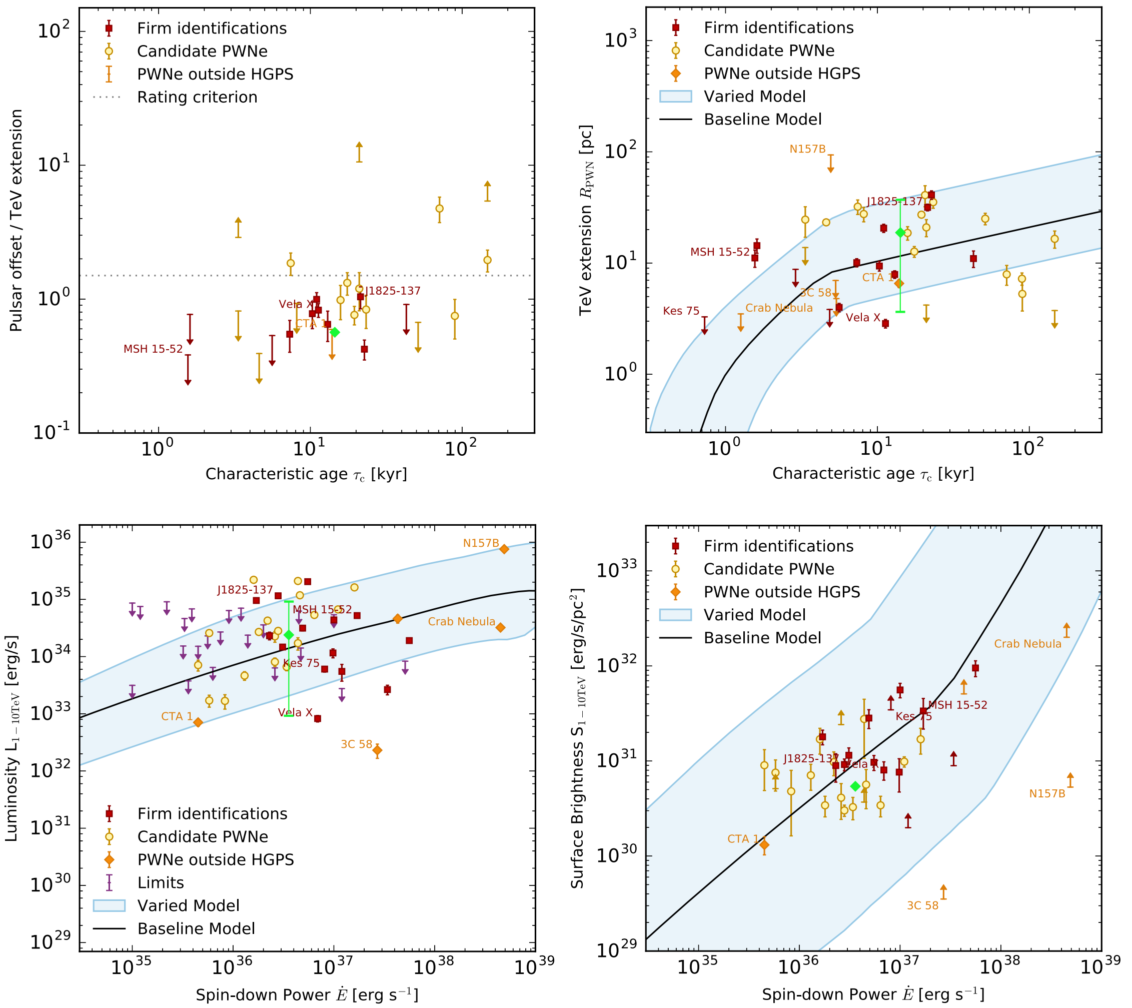

Figure 5.11: Position of the putative PWN system HESS J1826-130/PSR J1826-1256 (green marker) among the currently observed TeV PWN population for different characterization quantities. The distance of the system is assumed to be $d = 5.1$ kpc. For the quantities depending on this assumption, the shown error bars refer to a variation of the distance between $d = 1$ kpc and $d = 10$ kpc. Images adapted from H.E.S.S. Collaboration et al. 2017.

on the TeV observation than considering the total energy released so far by the pulsar in comparison to the energy required by the current electron spectrum, as made above. The apparent TeV efficiency is defined as $\varepsilon_{TeV} = L_{1-10\,\mathrm{TeV}}/\dot{E}$, the ratio of the current TeV luminosity (in the energy range 1-10 TeV) to the current spin-down power of the pulsar. For the considered system, the value accounts to $\varepsilon = 6.5 \times 10^{-3}$ for $d = 5.1$ kpc, which is a typical value for a PWN system at a characteristic age of 14.4 kyr. The corresponding value of the baseline model considered in the H.E.S.S. population study is about $\varepsilon = 4 \times 10^{-3}$. Without distance assumption, it can be parametrized as $\varepsilon = 2.5 \times 10^{-4}\,(d/1\,\mathrm{kpc})^2$.

In summary, the preceding discussion evaluates HESS J1826-130 as a plausible TeV PWN candidate in association with the energetic pulsar PSR J1826-1256. The main caveat in this discussion is the missing line-of-sight distance information of the pulsar. Also for the assumption of HESS J1826-130 being a PWN, the source stands out for its exceptionally hard energy spectrum, cf. Fig. 5.12.

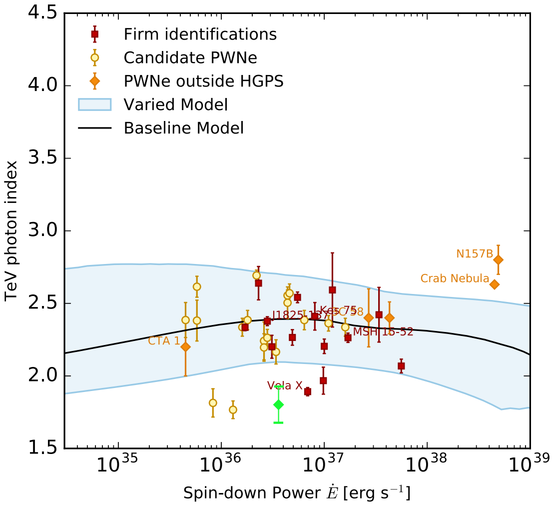

Figure 5.12: Position of the system HESS J1826-130/PSR J1826-1256 (green marker) among the currently observed TeV PWN population in a characterization comparing pulsar spin-down power vs. measured TeV photon index. Image adapted from H.E.S.S. Collaboration et al. 2017.

5.4 Conclusion

This section presented a basic modeling of the TeV emission from HESS J1826-130 in the context of a stationary modeling scenario, in which the present-age parent particle distributions are recovered. The modeling was performed in the context the MWL surrounding of the source, which allows for the following summarizing conclusions.

There are different scenarios which can explain the observed TeV emission of HESS J1826-130. The presence of dense molecular matter in the emission region gives rise to the assumption that it is of hadronic origin. In this case, the TeV emission of HESS J1826-130 may be connected to the progenitor SNR of HESS J1825-137, linking the roots of the two nearby TeV sources to the same single event of a stellar explosion. Alternatively, the two nearby SNRs G018.1-00.1 and G018.6-00.2 might be connected to the observed TeV excess via a runaway CR scenario.
The hadronic modeling yields a very hard spectral index of $1.69\,(^{+0.22}_{-0.27})_{\mathrm{stat}} \pm 0.08_{\mathrm{sys}}$ for the parent proton spectrum, with a cutoff energy estimate of $200\,(^{+217}_{-86})_{\mathrm{stat}} \pm 42_{\mathrm{sys}}$ TeV assuming a power law model with exponential cutoff. A 95% C.L. upper limit on the cutoff energy can be set at $\mathrm{UL}_{95} = 863 \pm 19_{\mathrm{stat,MC}} \pm 249_{\mathrm{sys}}$ TeV. These results show that the PeVatron hypothesis can most likely be ruled out.

In contrast to a hadronic emission scenario, the presence of the energetic pulsar PSR J1826-1256 in the immediate vicinity of the TeV emission supports the scenario of HESS J1826-130 being a new pulsar wind nebula. The leptonic modeling and an evaluation of the system according to the criteria of the H.E.S.S. TeV PWN population study (H.E.S.S. Collaboration et al. 2017) indeed reveals HESS J1826-130 as a plausible PWN candidate, matching in terms of observational characterization quantities to the so far observed TeV PWN population. Assuming a distance of 5.1 kpc, the system would pass all PWN post-selection candidate criteria of the H.E.S.S. TeV PWN population study.

In addition, the stellar cluster corresponding to the southern ASCA X-ray sub-peak is located very centrally in the emission region. This stellar cluster is also observed in the optical waveband, characterized as optical open cluster. Its total mass is estimated to be 382 $M_\odot$, located at a distance of 1.64 ± 0.19 kpc (Bica et al. 2004). Also for this object, a possible association with HESS J1826-130 cannot be firmly ruled out. However, the fact that no high-mass stars are observed in the optical regime, as well as the fact that its distance estimate differs significantly from the one of the bulk of dense molecular matter located in the region of the TeV emission (about 4 kpc), makes this association rather unlikely.

6 Summary

This thesis presents a detailed study of the unidentified TeV γ-ray source HESS J1826-130, which was considered as one of the most promising PeVatron candidates detected in the H.E.S.S. Galactic plane survey. In the first part of this work, our current understanding of CR astrophysics is reviewed, pointing out the necessity of Galactic PeV particle accelerators in the context of our current interpretation of the CR energy spectrum measured locally on Earth. The following discussion of the different production mechanisms of high-energy γ rays highlights the close connection between CR astrophysics and modern γ-ray astronomy using secondary γ-ray photons as messenger particles and motivates the search for Galactic PeVatrons in VHE γ rays.

The aim of this work was to derive a detailed morphological and spectral characterization of HESS J1826-130 based on the analysis of dedicated observations of the source with the H.E.S.S. instrument in VHE γ rays, thereby allowing for a further evaluation of its potential PeVatron character. Due to the complex analysis situation of HESS J1826-130 being located in the immediate vicinity of the bright and strongly extended pulsar wind nebula HESS J1825-137, the analysis procedure used in this work is based on a likelihood template-fit approach using the Gammalib/ctools analysis framework. Compared to the classical region-based analysis, one of the strong advantages of the chosen method is being able to take all sources in the field of view into account simultaneously. This provides a characterization of the individual components free of any contamination effects. The spectral analysis presented in this thesis yields a significant detection of a high-energy cutoff in the energy spectrum of HESS J1826-130, with a best-fit cutoff energy of $18.0 \pm 4.6\,\mathrm{TeV}$ and a very hard spectral index of 1.80 ± 0.13. For the description of the differential energy spectrum, a power law model with exponential cutoff is preferred over a pure power law by 4.4σ ($\mathrm{TS} = 19.3$) in a likelihood ratio test. The cutoff energy measured in the γ-ray spectrum is to be seen as strong indication against the PeVatron hypothesis as it points to a cutoff energy in the parent particle distribution clearly below the PeV energy range referring to a hadronic emission scenario.

The results derived with the new template-fit analysis approach were compared to those from the standard region-based On-Off analysis approach. The spectral high-energy cutoff detected in the ctools analysis is also detected in the On-Off region analysis if using an enlarged data set additionally employing archival H.E.S.S. I era data. The morphological and spectral analysis results of the different approaches are compatible if taking into account systematic analysis differences. The details of this comparison are given in Sec. 4.4. Various advanced analysis checks have been carried out to verify the new template-fit analysis procedure for the complex field of view under investigation. The calculation of pull distributions can be seen as a self-consistency check on the entire analysis procedure, which showed to work well and to yield correct results. A small bias was observed for the cutoff-energy estimate and the related spectral index when fitting a power law with exponential cutoff. This bias has been corrected and is taken into account for the final parameter estimates. Additionally, a comparison to already published H.E.S.S. analysis results on the source HESS J1825-137 showed an overall good agreement with the analysis results derived in the ctools analysis.

This thesis presents the first H.E.S.S. data analysis on a complex multi-source region using the new template-fit analysis approach based on the Gammalib/ctools framework. For the analysis of H.E.S.S. data, this can be seen as a proof-of-principle analysis, while for the future ground-based CTA observatory, the Gammalib/ctools software package is one of the candidates proposed as the standard Science Tools software (Knödlseder et al. 2016). Given the fact that for VHE γ-ray astronomy, topics like source confusion and source region contamination are becoming more and more important, the shifting of existing ground-based IACT experiments towards new analysis approaches is both reasonable and mandatory. However, due to the established robustness of the classical On-Off analysis approach for the analysis of isolated point-like sources and in order to allow for comparison between the different analysis methods, the On-Off region based analysis is currently being implemented in the Gammalib/ctools software as well. For the future, most likely both approaches will be used, depending on the exact analysis requirements and surrounding FoV conditions.

Dense molecular matter is located in the emission region of HESS J1826-130, which leads to the assumption that the TeV emission of HESS J1826-130 is of hadronic origin. A modeling of the γ-ray emission of HESS J1826-130 using the derived VHE γ-ray spectrum results in a best-fit cutoff energy estimate of the parent proton spectrum of $200\,(^{+217}_{-86})_{\mathrm{stat}} \pm 42_{\mathrm{sys}}$ TeV. A 95% C.L. upper limit on the cutoff energy can be set at $\mathrm{UL}_{95} = 863 \pm 19_{\mathrm{stat,MC}} \pm 249_{\mathrm{sys}}$ TeV. These results confirm the expectations from the spectral analysis of the γ-ray data and show that the PeVatron hypothesis can, in the context of a stationary modeling scenario, most likely be ruled out. There are different scenarios which might explain the TeV emission of HESS J1826-130. In the context of a hadronic origin, the observed emission might be connected to the progenitor SNR of HESS J1825-137. Alternatively, it might also be connected to the two nearby SNRs G018.1-00.1 and G018.6-00.2 via a runaway CR scenario. In contrast, the presence of the energetic pulsar PSR J1826-1256 in the near vicinity of HESS J1826-130 supports the assumption of HESS J1826-130 being of leptonic origin, i.e. a new pulsar wind nebula. A comparison of the system to the recent TeV pulsar wind nebula population study of the H.E.S.S. Collaboration (H.E.S.S. Collaboration et al. 2017) indeed reveals HESS J1826-130 as plausible PWN candidate, matching the so far observed population in terms of observational characterization quantities. Presumably, a firm identification will only become possible by future observations of the complex emission region with the CTA observatory, in combination with advanced multi-wavelength studies.

The search for Galactic PeVatrons remains one of the pressuring questions in the research fields of CR astrophysics and observational γ-ray astronomy. Current IACT instruments like H.E.S.S. provide a first instructive insight in the multi-TeV domain and have already allowed for first conclusions. In the near future, advanced water Cherenkov detectors such as the HAWC instrument (e.g. Abeysekara et al. 2017) will also play an interesting role in the hunt for PeV accelerators. Though being more limited in terms of spectral measurements and energy resolution, such detectors have a much larger FoV (> 1.5 sr) compared to IACT instruments and are therefore much better suited for surveying the entire sky. From this point of view, the γ-ray community awaits the first high-energy survey results from the HAWC experiment with huge interest. Moreover, the search for Galactic PeVatrons is listed as a key science project of the CTA observatory (see Cherenkov Telescope Array Consortium et al. 2017). CTA will provide energy coverage in a range from 20 GeV up to at least 300 TeV, with a larger FoV and significantly improved IRF response compared to

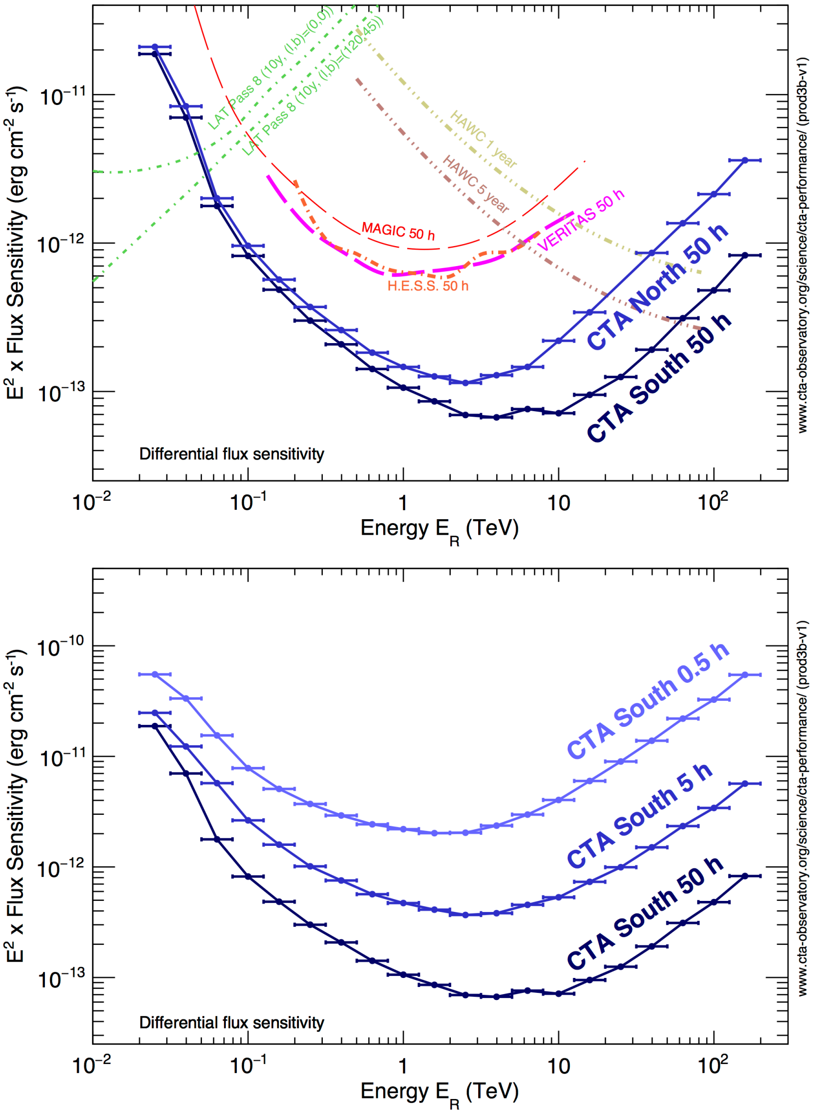

Figure 6.1: Comparison of sensitivity curves of different operating space- (Fermi-LAT) and ground-based γ-ray observatories to the expected sensitivity of the CTA observatory. CTA will improve the sensitivity of current IACT instruments by about one order of magnitude, and reach a comparable sensitivity within a much smaller observation time (bottom panel). Image credit: `https://www.cta-observatory.org/science/cta-performance/`.

current IACT experiments. It will increase the sensitivity of current instruments by about one order of magnitude over a broad energy range and reach comparable sensitivities in much smaller observation times, cf. Fig. 6.1. Future observations with such new upcoming experiments will help to further improve our understanding of the origin of Galactic CRs, their acceleration sites and the question of where and what the Galactic PeVatrons are - just one single highly energetic CR source at the center of our Galaxy, young supernova remnants or something different.

A Auxiliary analysis information

A.1 Runlist data set N

The runlist of data set N (193 observations), given in H.E.S.S.-internal run identification numbers:

104570, 104610, 104640, 104643, 104695, 104697, 104722, 104724, 105257, 105258, 105397, 105468, 105470, 105471, 105472, 105473, 105474, 105508, 105509, 105529, 105975, 105976, 106240, 106301, 106387, 106388, 106390, 106974, 107014, 107016, 107017, 107019, 107021, 107023, 107094, 107096, 107103, 107168, 107175, 107372, 107374, 107376, 107378, 107438, 107440, 107813, 107814, 107860, 107861, 107867, 107902, 107998, 108005, 108225, 108267, 108269, 108271, 108273, 108315, 108380, 108382, 108384, 108427, 108429, 108431, 108432, 108434, 108436, 108438, 108440, 108442, 108444, 108446, 108489, 108491, 108493, 108495, 108497, 108500, 108502, 108504, 108506, 108508, 108510, 108512, 108514, 108554, 108556, 108558, 108560, 108562, 108564, 108566, 108568, 108570, 108574, 108577, 108580, 108582, 108584, 108586, 108617, 108619, 108621, 108623, 108625, 108627, 108629, 108631, 108633, 108636, 108641, 108643, 108645, 108647, 108649, 108670, 108671, 108675, 108678, 108683, 108824, 108826, 108827, 108828, 108829, 108830, 108859, 108861, 108863, 108865, 108867, 108869, 108872, 108874, 108876, 108878, 108880, 108882, 108884, 108886, 108902, 108907, 108908, 108909, 108910, 108911, 108912, 108913, 108914, 108915, 108916, 108917, 108918, 108941, 108944, 108946, 108948, 108950, 108952, 108954, 108956, 108958, 108960, 108962, 108964, 108979, 108981, 108983, 108986, 108988, 108990, 108992, 108994, 108997, 109017, 109020, 109022, 109024, 109026, 109028, 109030, 109032, 109056, 109058, 109060, 109062, 109064, 109066, 109144, 109147, 109149, 109202

A.2 Testing the influence of energy dispersion

To test the impact of energy-dispersion for the analysis of data set N, a comparison of the spectral analysis results with and without taking the energy dispersion into account is given. The reconstructed differential energy spectra including detailed reconstruction information are given in Figs. A.1, A.2, A.3. The results are in very good agreement, indicating that the influence of energy dispersion is in a good approximation negligible in this analysis.

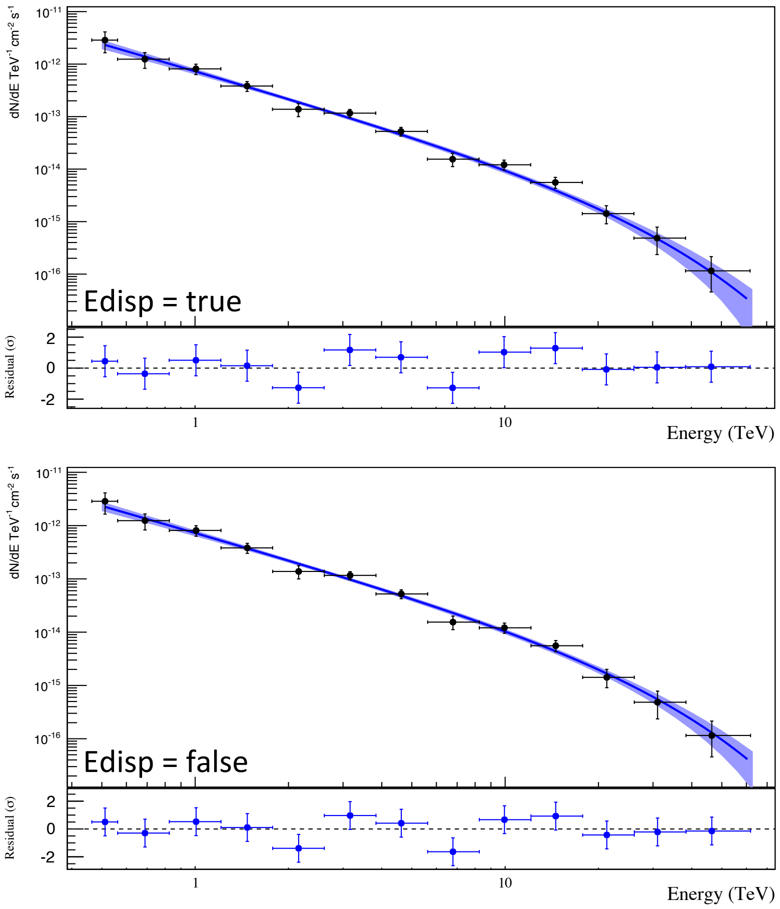

Figure A.1: Comparison of the reconstructed differential energy spectra of HESS J1826-130 for the analysis of data set N with (top) and without (bottom) taking into account energy dispersion. A detailed comparison of the differential flux points and fit results is given in Figs. A.2, A.3.

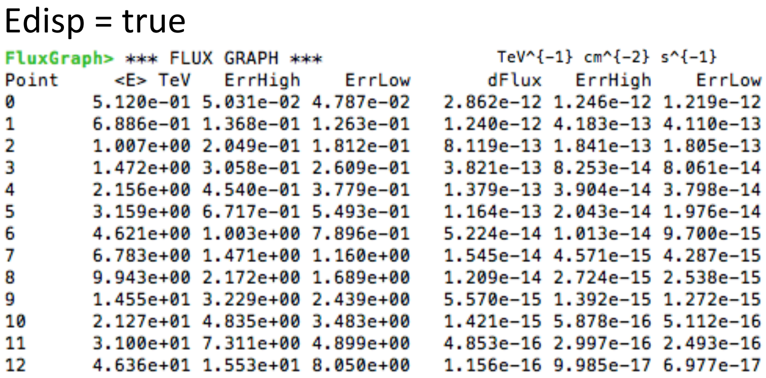

Edisp = true

```
FluxGraph> *** FLUX GRAPH ***                  TeV^{-1} cm^{-2} s^{-1}
Point      <E> TeV   ErrHigh     ErrLow        dFlux    ErrHigh     ErrLow
0       5.120e-01 5.031e-02 4.787e-02   2.862e-12 1.246e-12 1.219e-12
1       6.886e-01 1.368e-01 1.263e-01   1.240e-12 4.183e-13 4.110e-13
2       1.007e+00 2.049e-01 1.812e-01   8.119e-13 1.841e-13 1.805e-13
3       1.472e+00 3.058e-01 2.609e-01   3.821e-13 8.253e-14 8.061e-14
4       2.156e+00 4.540e-01 3.779e-01   1.379e-13 3.904e-14 3.798e-14
5       3.159e+00 6.717e-01 5.493e-01   1.164e-13 2.043e-14 1.976e-14
6       4.621e+00 1.003e+00 7.896e-01   5.224e-14 1.013e-14 9.700e-15
7       6.783e+00 1.471e+00 1.160e+00   1.545e-14 4.571e-15 4.287e-15
8       9.943e+00 2.172e+00 1.689e+00   1.209e-14 2.724e-15 2.538e-15
9       1.455e+01 3.229e+00 2.439e+00   5.570e-15 1.392e-15 1.272e-15
10      2.127e+01 4.835e+00 3.483e+00   1.421e-15 5.878e-16 5.112e-16
11      3.100e+01 7.311e+00 4.899e+00   4.853e-16 2.997e-16 2.493e-16
12      4.636e+01 1.553e+01 8.050e+00   1.156e-16 9.985e-17 6.977e-17
```

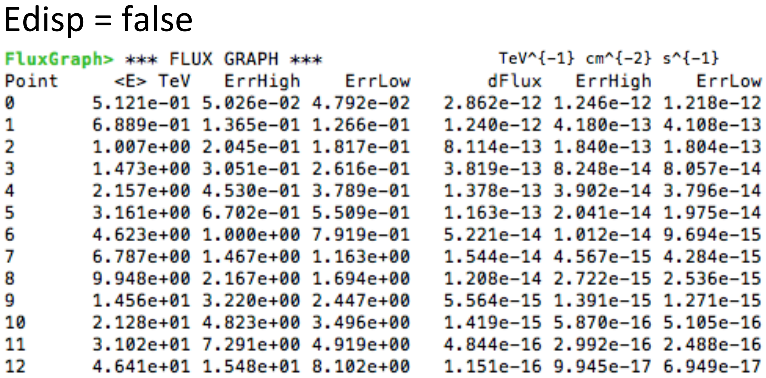

Edisp = false

```
FluxGraph> *** FLUX GRAPH ***                  TeV^{-1} cm^{-2} s^{-1}
Point      <E> TeV   ErrHigh     ErrLow        dFlux    ErrHigh     ErrLow
0       5.121e-01 5.026e-02 4.792e-02   2.862e-12 1.246e-12 1.218e-12
1       6.889e-01 1.365e-01 1.266e-01   1.240e-12 4.180e-13 4.108e-13
2       1.007e+00 2.045e-01 1.817e-01   8.114e-13 1.840e-13 1.804e-13
3       1.473e+00 3.051e-01 2.616e-01   3.819e-13 8.248e-14 8.057e-14
4       2.157e+00 4.530e-01 3.789e-01   1.378e-13 3.902e-14 3.796e-14
5       3.161e+00 6.702e-01 5.509e-01   1.163e-13 2.041e-14 1.975e-14
6       4.623e+00 1.000e+00 7.919e-01   5.221e-14 1.012e-14 9.694e-15
7       6.787e+00 1.467e+00 1.163e+00   1.544e-14 4.567e-15 4.284e-15
8       9.948e+00 2.167e+00 1.694e+00   1.208e-14 2.722e-15 2.536e-15
9       1.456e+01 3.220e+00 2.447e+00   5.564e-15 1.391e-15 1.271e-15
10      2.128e+01 4.823e+00 3.496e+00   1.419e-15 5.870e-16 5.105e-16
11      3.102e+01 7.291e+00 4.919e+00   4.844e-16 2.992e-16 2.488e-16
12      4.641e+01 1.548e+01 8.102e+00   1.151e-16 9.945e-17 6.949e-17
```

Figure A.2: Comparison of reconstructed differential flux points for the analysis of data set N with (top) and without (bottom) taking into account energy dispersion.

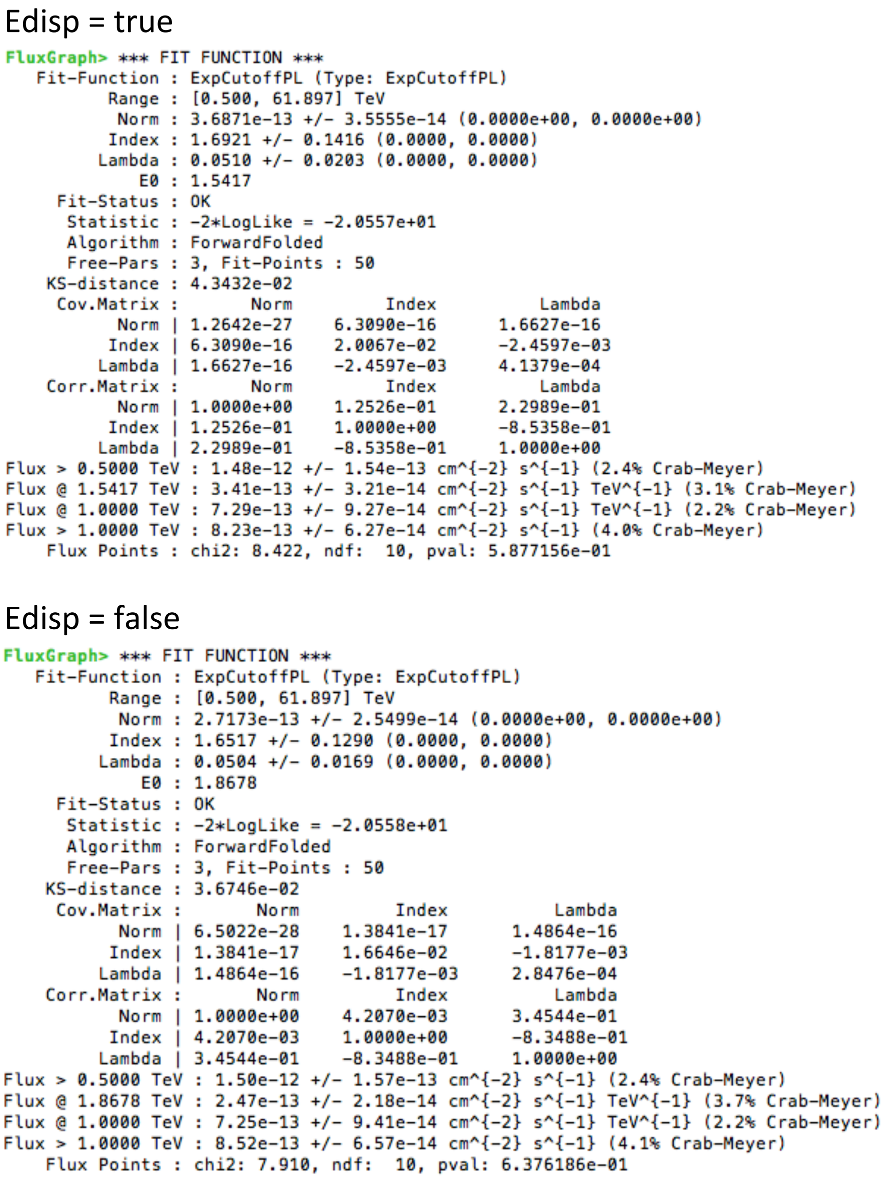

Edisp = true

```
FluxGraph> *** FIT FUNCTION ***
   Fit-Function : ExpCutoffPL (Type: ExpCutoffPL)
          Range : [0.500, 61.897] TeV
           Norm : 3.6871e-13 +/- 3.5555e-14 (0.0000e+00, 0.0000e+00)
          Index : 1.6921 +/- 0.1416 (0.0000, 0.0000)
         Lambda : 0.0510 +/- 0.0203 (0.0000, 0.0000)
             E0 : 1.5417
     Fit-Status : OK
      Statistic : -2*LogLike = -2.0557e+01
      Algorithm : ForwardFolded
      Free-Pars : 3, Fit-Points : 50
    KS-distance : 4.3432e-02
     Cov.Matrix :       Norm          Index          Lambda
           Norm | 1.2642e-27    6.3090e-16      1.6627e-16
          Index | 6.3090e-16    2.0067e-02      -2.4597e-03
         Lambda | 1.6627e-16    -2.4597e-03     4.1379e-04
    Corr.Matrix :       Norm          Index          Lambda
           Norm | 1.0000e+00    1.2526e-01      2.2989e-01
          Index | 1.2526e-01    1.0000e+00      -8.5358e-01
         Lambda | 2.2989e-01    -8.5358e-01     1.0000e+00
Flux > 0.5000 TeV : 1.48e-12 +/- 1.54e-13 cm^{-2} s^{-1} (2.4% Crab-Meyer)
Flux @ 1.5417 TeV : 3.41e-13 +/- 3.21e-14 cm^{-2} s^{-1} TeV^{-1} (3.1% Crab-Meyer)
Flux @ 1.0000 TeV : 7.29e-13 +/- 9.27e-14 cm^{-2} s^{-1} TeV^{-1} (2.2% Crab-Meyer)
Flux > 1.0000 TeV : 8.23e-13 +/- 6.27e-14 cm^{-2} s^{-1} (4.0% Crab-Meyer)
    Flux Points : chi2: 8.422, ndf:  10, pval: 5.877156e-01
```

Edisp = false

```
FluxGraph> *** FIT FUNCTION ***
   Fit-Function : ExpCutoffPL (Type: ExpCutoffPL)
          Range : [0.500, 61.897] TeV
           Norm : 2.7173e-13 +/- 2.5499e-14 (0.0000e+00, 0.0000e+00)
          Index : 1.6517 +/- 0.1290 (0.0000, 0.0000)
         Lambda : 0.0504 +/- 0.0169 (0.0000, 0.0000)
             E0 : 1.8678
     Fit-Status : OK
      Statistic : -2*LogLike = -2.0558e+01
      Algorithm : ForwardFolded
      Free-Pars : 3, Fit-Points : 50
    KS-distance : 3.6746e-02
     Cov.Matrix :       Norm          Index          Lambda
           Norm | 6.5022e-28    1.3841e-17      1.4864e-16
          Index | 1.3841e-17    1.6646e-02      -1.8177e-03
         Lambda | 1.4864e-16    -1.8177e-03     2.8476e-04
    Corr.Matrix :       Norm          Index          Lambda
           Norm | 1.0000e+00    4.2070e-03      3.4544e-01
          Index | 4.2070e-03    1.0000e+00      -8.3488e-01
         Lambda | 3.4544e-01    -8.3488e-01     1.0000e+00
Flux > 0.5000 TeV : 1.50e-12 +/- 1.57e-13 cm^{-2} s^{-1} (2.4% Crab-Meyer)
Flux @ 1.8678 TeV : 2.47e-13 +/- 2.18e-14 cm^{-2} s^{-1} TeV^{-1} (3.7% Crab-Meyer)
Flux @ 1.0000 TeV : 7.25e-13 +/- 9.41e-14 cm^{-2} s^{-1} TeV^{-1} (2.2% Crab-Meyer)
Flux > 1.0000 TeV : 8.52e-13 +/- 6.57e-14 cm^{-2} s^{-1} (4.1% Crab-Meyer)
    Flux Points : chi2: 7.910, ndf:  10, pval: 6.376186e-01
```

Figure A.3: Comparison of best-fit results for the spectral model of an exponential cutoff power law, with (top) and without (bottom) taking into account energy dispersion.

Bibliography

Aab, A., Abreu, P., Aglietta, M., et al. 2017, JCAP, 4, 038

Abdo, A. A., Ackermann, M., Ajello, M., et al. 2009a, Science, 325, 840

Abdo, A. A., Ackermann, M., Ajello, M., et al. 2009b, ApJS, 183, 46

Abeysekara, A. U., Albert, A., Alfaro, R., et al. 2017, ArXiv e-prints, 1702.02992

Abraham, J., Abreu, P., Aglietta, M., et al. 2009, ArXiv e-prints, 0906.2189

Abraham, J., Abreu, P., Aglietta, M., et al. 2010, Physical Review Letters, 104, 091101

Abramowski, A., Aharonian, F., Benkhali, F. A., et al. 2014, Phys. Rev. D, 90, 122007

Acharya, B. S., Actis, M., Aghajani, T., et al. 2013, Astroparticle Physics, 43, 3

Ackermann, M., Ajello, M., Allafort, A., et al. 2013, Science, 339, 807

Ackermann, M., Ajello, M., Baldini, L., et al. 2011, ApJ, 726, 35

Aharonian, F., Akhperjanian, A., Barrio, J., et al. 2001, A&A, 370, 112

Aharonian, F., Akhperjanian, A. G., Aye, K.-M., et al. 2005a, Science, 307, 1938

Aharonian, F., Akhperjanian, A. G., Aye, K.-M., et al. 2005b, Science, 309, 746

Aharonian, F., Akhperjanian, A. G., Bazer-Bachi, A. R., et al. 2006a, A&A, 457, 899

Aharonian, F., Akhperjanian, A. G., Bazer-Bachi, A. R., et al. 2006b, A&A, 460, 365

Aharonian, F., Akhperjanian, A. G., Bazer-Bachi, A. R., et al. 2006c, A&A, 460, 743

Aharonian, F., Angüner, E. O., Bordas, P., et al. 2014, HESS Legacy on Galactic PeVatrons, H.E.S.S. Proposal for 2015 Season, H.E.S.S. internal

Aharonian, F. & Neronov, A. 2005, ApJ, 619, 306

Aharonian, F. A. 2004, Very high energy cosmic gamma radiation : A crucial window on the extreme Universe, World Scientific Publishing Co. Pte. Ltd.

Aharonian, F. A. 2013, Astroparticle Physics, 43, 71

Aharonian, F. A., Akhperjanian, A. G., Bazer-Bachi, A. R., et al. 2005c, A&A, 442, L25

Aharonian, F. A. & Atoyan, A. M. 1996, A&A, 309, 917

Aleksić, J., Alvarez, E. A., Antonelli, L. A., et al. 2012, Astroparticle Physics, 35, 435

Aloisio, R., Berezinsky, V., & Gazizov, A. 2012, Astroparticle Physics, 39, 129

Angüner, E. O., Aharonian, F., Bordas, P., et al. 2017a, in American Institute of Physics Conference Series, Vol. 1792, 6th International Symposium on High Energy Gamma-Ray Astronomy, 040024

Angüner, E. O., Casanova, S., Oya, I., et al. 2017b, ArXiv e-prints, 1708.04844

Asaoka, Y., Shikaze, Y., Abe, K., et al. 2002, Physical Review Letters, 88, 051101

Atoyan, A. & Dermer, C. D. 2004, ApJ, 617, L123

Atoyan, A. M., Aharonian, F. A., & Völk, H. J. 1995, Phys. Rev. D, 52, 3265

Atwood, W. B., Abdo, A. A., Ackermann, M., et al. 2009, ApJ, 697, 1071

Axford, W. I., Leer, E., & Skadron, G. 1977, International Cosmic Ray Conference, 11, 132

Baade, W. & Zwicky, F. 1934, Proceedings of the National Academy of Science, 20, 259

Bell, A. R. 1978, MNRAS, 182, 147

Bell, A. R. & Lucek, S. G. 2001, MNRAS, 321, 433

Benbow, W. 2005, in American Institute of Physics Conference Series, Vol. 745, High Energy Gamma-Ray Astronomy, ed. F. A. Aharonian, H. J. Völk, & D. Horns, 611–616

Berezinskii, V. S. & Grigor'eva, S. I. 1988, A&A, 199, 1

Berge, D. 2006, A detailed study of The gamma-ray supernova remnant RX J1713.7-3946 with H.E.S.S., PhD Thesis, Universität Potsdam

Berge, D., Funk, S., & Hinton, J. 2007, A&A, 466, 1219

Bernlöhr, K. 2008, Astroparticle Physics, 30, 149

Bernlöhr, K., Carrol, O., Cornils, R., et al. 2003, Astroparticle Physics, 20, 111

Bethe, H. & Heitler, W. 1934, Proceedings of the Royal Society of London Series A, 146, 83

Bica, E., Bonatto, C., & Dutra, C. M. 2004, A&A, 422, 555

Blandford, R. D. & Ostriker, J. P. 1978, ApJ, 221, L29

Blasi, P. & Amato, E. 2012, JCAP, 1, 010

Blumenthal, G. R. & Gould, R. J. 1970, Reviews of Modern Physics, 42, 237

Brogan, C. L., Gelfand, J. D., Gaensler, B. M., Kassim, N. E., & Lazio, T. J. W. 2006, ApJ, 639, L25

Bykov, A., Gehrels, N., Krawczynski, H., et al. 2012, Space Sci. Rev., 173, 309

Cash, W. 1979, ApJ, 228, 939

Cerenkov, P. A. 1937, Physical Review, 52, 378

Cherenkov Telescope Array Consortium, Acharya, B. S., Agudo, I., et al. 2017, ArXiv e-prints, 1709.07997

Clifton, T. R., Lyne, A. G., Jones, A. W., McKenna, J., & Ashworth, M. 1992, MNRAS, 254, 177

Cornils, R., Gillessen, S., Jung, I., et al. 2003, Astroparticle Physics, 20, 129

Dame, T. M., Hartmann, D., & Thaddeus, P. 2001, ApJ, 547, 792

Davies, J. M. & Cotton, E. S. 1957, Solar Energy, 1, 16

de Naurois, M. 2012, L'astronomie gamma de très haute énergie. Ouverture d'une nouvelle fenêtre astronomique sur l'Univers non thermique, Habilitation, Université Pierre et Marie Curie - Paris VI

Degrange, B. & Fontaine, G. 2015, Comptes Rendus Physique, 16, 587

Deil, C., Boisson, C., Kosack, K., et al. 2017, in American Institute of Physics Conference Series, Vol. 1792, 6th International Symposium on High Energy Gamma-Ray Astronomy, 070006

Deil, C., Brun, F., Carrigan, S., et al. 2015, in International Cosmic Ray Conference, Vol. 34, 34th International Cosmic Ray Conference (ICRC2015), 773

Di Mauro, M., Donato, F., Fornengo, N., & Vittino, A. 2016, JCAP, 5, 031

Doering, M., Bernloehr, K., Hermann, G., Hofmann, W., & Lampeitl, H. 2001, ArXiv Astrophysics e-prints, astro-ph/0107149

Donath, A., Deil, C., Arribas, M. P., et al. 2015, in International Cosmic Ray Conference, Vol. 34, 34th International Cosmic Ray Conference (ICRC2015), 789

Fermi, E. 1949, Physical Review, 75, 1169

Fichtel, C. E., Bertsch, D. L., Chiang, J., et al. 1994, ApJS, 94, 551

Finley, J. P., Srinivasan, R., & Park, S. 1996, ApJ, 466, 938

Foreman-Mackey, D., Hogg, D. W., Lang, D., & Goodman, J. 2013, PASP, 125, 306

Frank, I. & Tamm, I. 1937, C. R. Acad. Sci. USSR, 14, 109

Funk, S. 2015, Annual Review of Nuclear and Particle Science, 65, 245

Funk, S., Hermann, G., Hinton, J., et al. 2004, Astroparticle Physics, 22, 285

Gabici, S. & Aharonian, F. A. 2007, ApJ, 665, L131

Gaensler, B. M., Schulz, N. S., Kaspi, V. M., Pivovaroff, M. J., & Becker, W. E. 2003, ApJ, 588, 441

Gaggero, D., Maccione, L., Di Bernardo, G., Evoli, C., & Grasso, D. 2013, Physical Review Letters, 111, 021102

Gaisser, T. K., Stanev, T., & Tilav, S. 2013, Frontiers of Physics, 8, 748

Ginzburg, V. L. & Syrovatskiy, S. I. 1961, Geomagnetism and Aeronomy, 1, 427

Giuliani, A., Cardillo, M., Tavani, M., et al. 2011, ApJ, 742, L30

Greisen, K. 1966, Physical Review Letters, 16, 748

Grondin, M.-H., Funk, S., Lemoine-Goumard, M., et al. 2011, ApJ, 738, 42

Grupen, C. 2000, Astroteilchenphysik - Das Universum im Licht der kosmischen Strahlung, Vieweg Verlag

Hahn, J., Gast, H., de los Reyes, R., et al. 2013, Heidelberg Data Quality Selection, H.E.S.S. internal note

Hartman, R. C., Bertsch, D. L., Bloom, S. D., et al. 1999, ApJS, 123, 79

Heck, D., Knapp, J., Capdevielle, J. N., Schatz, G., & Thouw, T. 1998, CORSIKA: a Monte Carlo code to simulate extensive air showers, TIB Hannover

H.E.S.S. Collaboration, Abdalla, H., Abramowski, A., et al. 2017, ArXiv e-prints, 1702.08280

H.E.S.S. Collaboration, Abdalla, H., Abramowski, A., et al. 2018, A&A forthcoming

H.E.S.S. Collaboration, Abramowski, A., Aharonian, F., et al. 2016, Nature, 531, 476

Hillas, A. M. 1985, International Cosmic Ray Conference, 3, 445

Hillas, A. M. 2005, Journal of Physics G Nuclear Physics, 31, R95

Hillas, A. M. 2006, ArXiv Astrophysics e-prints, astro-ph/0607109

Hinton, J. A. & Hofmann, W. 2009, ARA&A, 47, 523

Hinton, J. A. & the HESS Collaboration. 2004, New Astronomy Review, 48, 331

Holder, J., Acciari, V. A., Aliu, E., et al. 2008, in American Institute of Physics Conference Series, Vol. 1085, American Institute of Physics Conference Series, ed. F. A. Aharonian, W. Hofmann, & F. Rieger, 657–660

Hörandel, J. R. 2004, Astroparticle Physics, 21, 241

Ibarra, A., Tran, D., & Weniger, C. 2013, International Journal of Modern Physics A, 28, 1330040

Istomin, Y. N. 2014, New Astronomy, 27, 13

Jogler, T. & Funk, S. 2016, ApJ, 816, 100

Johanson, A. K. & Kerton, C. R. 2009, AJ, 138, 1615

Kafexhiu, E., Aharonian, F., Taylor, A. M., & Vila, G. S. 2014, Phys. Rev. D, 90, 123014

Kelner, S. R., Aharonian, F. A., & Bugayov, V. V. 2006, Phys. Rev. D, 74, 034018

Knödlseder, J. 2012, in Astronomical Society of the Pacific Conference Series, Vol. 461, Astronomical Data Analysis Software and Systems XXI, ed. P. Ballester, D. Egret, & N. P. F. Lorente, 65

Knödlseder, J. 2017, Learning ctools and GammaLib development in an hour, 7th ctools coding sprint, ECAP Erlangen

Knödlseder, J., Mayer, M., Deil, C., et al. 2016, A&A, 593, A1

Krymskii, G. F. 1977, Akademiia Nauk SSSR Doklady, 234, 1306

Lamanna, G., Antonelli, L. A., Contreras, J. L., et al. 2015, in International Cosmic Ray Conference, Vol. 34, 34th International Cosmic Ray Conference (ICRC2015), 947

Lemiere, A., Terrier, R., & Djannati-Ataï, A. 2006, ArXiv Astrophysics e-prints, astro-ph/0602436

Li, T.-P. & Ma, Y.-Q. 1983, ApJ, 272, 317

Longair, M. S. 2011, High Energy Astrophysics, Cambridge University Press

Lu, F. J., Wang, Q. D., Ge, M. Y., et al. 2011, ApJ, 732, 11

Marquardt, D. W. 1963, Journal of the society for Industrial and Applied Mathematics, 11, 431

Mattox, J. R., Bertsch, D. L., Chiang, J., et al. 1996, ApJ, 461, 396

Mayer, M. 2014, Pulsar Wind Nebulae At High Energies: A Diverse Population and Exceptional Twins, PhD Thesis, Universität Potsdam

Mitchell, A. M. W., Caroff, S., Parsons, R. D., et al. 2017, ArXiv e-prints, 1708.03126

Neyman, J. & Pearson, E. S. 1928, Biometrika, 20A, 175

Nolan, P. L., Tompkins, W. F., Grenier, I. A., & Michelson, P. F. 2003, ApJ, 597, 615

Ohm, S., van Eldik, C., & Egberts, K. 2009, Astroparticle Physics, 31, 383

Patrignani, C. & Particle Data Group. 2016, Chinese Physics C, 40, 100001

Pence, W., Blackburn, J. K., & Greene, E. 1993, in Astronomical Society of the Pacific Conference Series, Vol. 52, Astronomical Data Analysis Software and Systems II, ed. R. J. Hanisch, R. J. V. Brissenden, & J. Barnes, 541

Pence, W. D., Chiappetti, L., Page, C. G., Shaw, R. A., & Stobie, E. 2010, A&A, 524, A42

Piron, F., Djannati-Atai, A., Punch, M., et al. 2001, A&A, 374, 895

Ptuskin, V. S., Rogovaya, S. I., Zirakashvili, V. N., et al. 1993, A&A, 268, 726

Ray, P. S., Kerr, M., Parent, D., et al. 2011, ApJS, 194, 17

Roberts, M. S. E. 2009, The Pulsar Wind Nebulae of Three Radio Quiet Gamma-Ray Pulsars, Conference Presentation, Supernova Remnants and Pulsar Wind Nebulae in the Chandra Era, Boston

Roberts, M. S. E., Gotthelf, E. V., Halpern, J. P., Brogan, C. L., & Ransom, S. M. 2007, in WE-Heraeus Seminar on Neutron Stars and Pulsars 40 years after the Discovery, ed. W. Becker & H. H. Huang, 24

Roberts, M. S. E., Romani, R. W., & Kawai, N. 2001, ApJS, 133, 451

Roulet, E. 2004, International Journal of Modern Physics A, 19, 1133

Sakurai, I., Kawai, N., Torii, K., & Shibata, S. 2001, in Astronomical Society of the Pacific Conference Series, Vol. 251, New Century of X-ray Astronomy, ed. H. Inoue & H. Kunieda, 408

Schure, K. M. & Bell, A. R. 2013, MNRAS, 435, 1174

Sokolsky, P. & HiRes Collaboration. 2011, Nuclear Physics B Proceedings Supplements, 212, 74

Stecker, F. W. 1970, Ap&SS, 6, 377

Stecker, F. W. & Salamon, M. H. 1999, ApJ, 512, 521

Strong, A. W., Moskalenko, I. V., Porter, T. A., et al. 2009, ArXiv e-prints, 0907.0559

Strong, A. W., Moskalenko, I. V., & Ptuskin, V. S. 2007, Annual Review of Nuclear and Particle Science, 57, 285

The Fermi-LAT Collaboration, Ajello, M., Atwood, W. B., et al. 2017, ArXiv e-prints, 1702.00664

Thoudam, S., Rachen, J. P., van Vliet, A., et al. 2016, A&A, 595, A33

Tinyakov, P. 2014, Nuclear Instruments and Methods in Physics Research A, 742, 29

Vink, J. & Laming, J. M. 2003, ApJ, 584, 758

Voisin, F., Rowell, G., Burton, M. G., et al. 2016, MNRAS, 458, 2813

Völk, H. J., Berezhko, E. G., & Ksenofontov, L. T. 2005, A&A, 433, 229

Völk, H. J. & Bernlöhr, K. 2009, Experimental Astronomy, 25, 173

Wakely, S. & Horan, D. 2017, TeVCat, online Gamma-Ray catalog, `http://tevcat.uchicago.edu/`

Weekes, T. C., Cawley, M. F., Fegan, D. J., et al. 1989, ApJ, 342, 379

Wilks, S. S. 1938, The Annals of Mathematical Statistics, 9, 60

Winkler, M. W. 2017, JCAP, 2, 048

Yuan, J. P., Wang, N., Manchester, R. N., & Liu, Z. Y. 2010, MNRAS, 404, 289

Zabalza, V. 2015, in International Cosmic Ray Conference, Vol. 34, 34th International Cosmic Ray Conference (ICRC2015), 922

Zatsepin, G. T. & Kuz'min, V. A. 1966, ZhETF Pisma Redaktsiiu, 4, 114

Zhang, L. & Cheng, K. S. 1998, A&A, 335, 234

Acknowledgements/Danksagung

Zum erfolgreichen Abschluss dieser Arbeit haben viele Personen auf unterschiedliche Art und Weise beigetragen. Ich möchte mich an dieser Stelle bei allen bedanken, die mich während meiner Zeit am ECAP begleitet und unterstützt haben und ohne deren Beitrag diese Arbeit in dieser Form nicht möglich gewesen wäre. Insbesondere gilt mein Dank

- Herrn Prof. Dr. Christopher van Eldik. Vielen Dank, Christopher, dass du es mir ermöglicht hast, meine Arbeit hier am ECAP anzufertigen. Vielen Dank für die gute Betreuung, insbesondere für zahllose '5 Minuten' – diese vielen, wichtigen Diskussionen mit dir haben diese Arbeit immer wieder maßgeblich in die richtige Richtung gelenkt.
- Herrn Prof. Dr. Stefan Funk für das Beantworten zahlreicher Fragen und interessante Diskussionen.
- Der gesamten Erlanger Gamma-Gruppe. Vielen Dank für die gute Zusammenarbeit, eure Unterstützung und die gemeinsame Zeit, ihr seid ein super Team. Vor allem werde ich auch unsere gemeinsamen Ausflüge, ob fachliche Konferenzen oder Erlanger Pub-Abende, vermissen. Also thanks to Giacomo for a nice visit in the Dolomites – that was fun beyond all of the work. Vielen Dank insbesondere auch an unser Post-Doc Team: I asked so many questions to all of you and I always enjoyed our discussions! Idan, Dima, special thanks for proofreading my thesis! Tobias für zahlreiche Diskussionen vor allem zu Beginn der ctools Analyse. Lars für die gute Zusammenarbeit innerhalb des FITS und open-source tool Projekts. Marc für viele gute Ratschläge und Gespräche auch neben der Physik.
- Meinen Bürokollegen Stefan, Manuel und David aus Zimmer 309. Danke für eine angenehme Arbeitsatmosphäre und eine super Zeit! In diesem Büro schreckt niemand davor zurück, offene Fragen in den Raum zu werfen, und muntere Diskussion gehört hier zum Arbeitsalltag.
- Der H.E.S.S. FITS data Task Group, insbesondere den Erlanger Mitgliedern der Gruppe, Lars, Domenico und Andreas. Domenico vor allem für die gute Zusammenarbeit in Richtung ctools Analyse.
- Dem ctools/GammaLib Software-Team um Jürgen Knödlseder. Ohne dieses Framework wäre diese Arbeit so nicht möglich gewesen. Vor allem auch vielen Dank an Michael Mayer für das Heranführen an ctools/GammaLib von H.E.S.S. Seite kommend und für die Unterstützing in allen damit in Verbindung stehenden Aspekten.
- The HESS J1826 Task Group, Ozi, Sabrina and Igor, for the joint collaborative work and valuable discussions.
- Sebastian für die gemeinsamen montäglichen Mensabesuche, wo wir so vieles besprochen haben.
- Meiner Familie für die langjährige Unterstützung während meines gesamten Studiums bis hin zur Promotion.
- Dir, Julia! Dir gilt mein größter Dank, einfach für alles! Für dein Verständnis und deine Unterstützung, dafür dass du dir all die Geschichten über diese Arbeit angehört hast und dass du für mich da bist!